WMO/CAS/WWW

EIGHTH INTERNATIONAL WORKSHOP ON TROPICAL CYCLONES

Topic 4.4 Oceanic Influences and the Air-Sea Interface

Rapporteur: L. K. (Nick) Shay
Upper Ocean Dynamics Laboratory
Division of Meteorology and Physical Oceanography
Rosenstiel School of Marine and Atmospheric Science
University of Miami
4600 Rickenbacker Causeway
Miami, FL 33149, USA
e-mail: nshay@rsmas.miami.edu
fax: 305-421-4696

Working Group: M. M. Ali, S. Chen, I. Ginis, G. Halliwell, H-S Kim, Marie-Dominque Leroux, I-I Lin, A. Wada

4.4.1: Introduction

The objective of this report is to document progress since IWTC-VII in this thematic area from experimental, observational, empirical, theoretical, and numerical perspectives. The report benefits from the recently published Book Chapter entitled *Air-Sea Interactions In Tropical Cyclones* (Shay 2010) in the second edition of the Global Perspectives of Tropical Cyclones edited by Chan and Kepert (2010). The report begins by briefly describing progress in upper-ocean processes that include the oceanic mixed layer (OML) and the thermocline. This section is followed by a discussion of the air-sea interface that includes surface winds and waves, and the communication to the atmospheric boundary layer through the momentum and enthalpy fluxes across the interface. These findings are summarized within a global context with specific recommendations to the WMO's Commission on Atmospheric Science (CAS).

4.4.2: SST and Upper-Ocean Processes

Coupled oceanic and atmospheric models to predict hurricane intensity and structure change are increasingly being used to issue forecasts to the public who increasingly rely on the most advanced weather forecasting systems to prepare for landfall (Marks and Shay 1998; Rogers *et al.* 2006). For such models, it has become clear over the past decade that ocean models will have to include realistic initial conditions to simulate the oceanic response to hurricane forcing (Price *et al.* 1994; Sanford *et al.* 1987, 2007, 2011; Shay 2009; D'Asaro 2003, Jacob and Shay 2003; D'Asaro *et al.* 2007; Lin *et al.* 2008, 2009; Lin et al. 2013; Halliwell *et al.* 2008; Fan *et al.* 2009a, Wada *et al.* 2009, 2011; Jaimes and Shay 2009, 2010, 2011; Mrvaljevic *et al.* 2013; D'Asaro *et al.* 2011, 2013), but also to simulate the atmospheric response to oceanic forcing (Bender and Ginis 2000; Bao *et al.* 2000; Shay et al. 2000, Hong *et al.* 2000; Walker *et al.* 2005; Lin *et al.* 2009, 2013; Wada

and Usui 2007; Wada *et al.* 2013, 2014; Wu *et al*. 2007; Sandery et al. 2010; Chen *et al*. 2010; Jaimes *et al.* 2014).

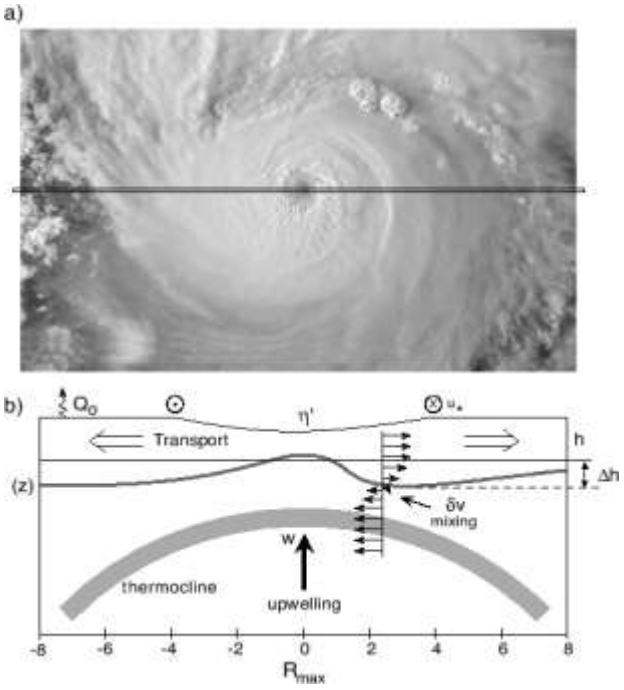

Figure 1: a) Tropical cyclone image and b) cartoon of the physical processes forced by hurricane winds such as shear-induced mixing and deepening of the ocean mixed layer, upwelling due to transport away from the center, and surface heat fluxes from the ocean to the atmosphere, all of which may contribute to ocean cooling during TC passage (from Shay 2009).

As shown in Fig. 1, upper-ocean mixing and cooling are a strong function of forced near-inertial current shears that reduce the Richardson numbers below criticality, which induces entrainment mixing (Price 1981; Schade and Emanuel 1999; Shay 2009; D'Asaro 2003, D'Asaro *et al.* 2007; Jacob and Shay 2003). The contributions to the heat and mass budgets by shear-driven entrainment heat fluxes across the OML base (h) are 60 to 85%, surface heat fluxes are between 5 to 15%, and horizontal advection by ocean currents are 5 to 15 % (Price *et al.* 1994; Jacob *et al.* 2000). All of these processes impact the SST and Oceanic Heat Content (OHC) variability. In addition, wind-driven upwelling of the isotherms due to net upper ocean transport away from the storm modulate the shear-induced (S) ocean mixing events by an upward transport of cooler water from the thermocline. This transport increases the buoyancy frequency (N), which tends to keep the Richardson number above criticality. In the Loop Current (LC) and warm core ring (WCR) regimes with deep, warm thermal layers, cooling induced by these physical processes (Fig. 1) is considerably less as much greater turbulent-induced mixing by the current shear is required to cool and deepen the OML (Uhlhorn and Shay 2012, 2013). Quantifying the effects of forced current (and shear) on the OHC and SST distributions is central to accurately forecasting hurricane intensity and structure change.

To place these concepts into context, important example of this later effect was observed during the passages of hurricanes Katrina, Rita, and Wilma during the 2005 Atlantic Ocean hurricane season and more recently during the ONR-sponsored Impact of Typhoon on Pacific (ITOP) experiment in 2010 as shown in Fig. 2 (D'Asaro *et al*. 2013). During the ITOP field campaign, concurrent atmospheric and ocean observations of three typhoons

(Megi, Fanapi, and Malakas) over the western North Pacific were acquired from multiple platforms. In-situ aircraft observations from WC-130 aircraft observed the pre-TC, during-TC, and post-TC atmospheric and oceanic fields of these three typhoons. These cases are supertyphoon (ST) Megi (cat 5), typhoon Fanapi (cat 3) and typhoon Malakas (cat 2). The pre-TC SST conditions for these cases were approximately 29^{o}C. However, the distinction is in the observed sub-surface pre-TC conditions (Lin *et al.* 2013). ST Megi intensified over regions of highest OHC exceeding 120 kJ cm^{-2}, followed by Fanapi (pre-TC OHC ~70 kJ cm^{-2}, and Malakas (pre-TC OHC ~60 kJ cm^{-2}). Detailed air-sea flux analyses support this strong control by subsurface thermal condition on the intensification of these three cases that will be discussed below (Lin *et al.* 2013).

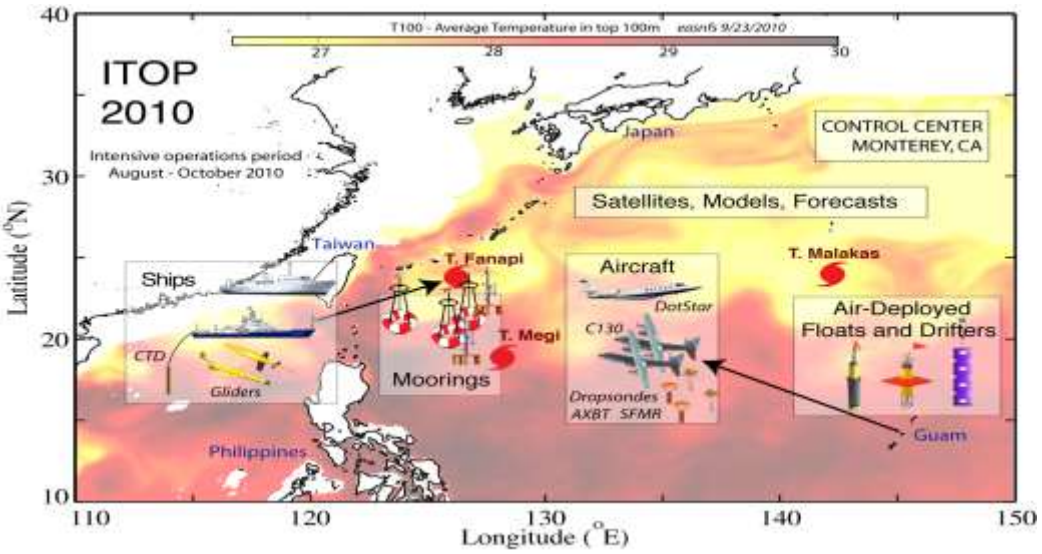

Figure 2: Cartoon of ITOP operations area, experimental tools and strategy. Locations of the three major ITOP storms at the time of maximum sampling are shown by storm symbols (After D'Asaro *et al*. 2013).

During Katrina, Rita and Wilma, a trifecta of cat-5 TCs, favorable atmospheric conditions prevailed over the Northwest Caribbean Sea and Gulf of Mexico (GOM) as the LC extended several hundred kilometers north of the Yucatan Strait. As these storms moved over deep warm pools (OHC > 120 kJ cm^{-2}) ,all three hurricanes explosively deepened and were more closely correlated with the OHC variations (and deep isotherms) than with the sea-surface temperatures (SST) distributions, which were essentially flat and exceeded 30^{o}C over most of the region. By contrast, the OHC and 26^{o}C isotherm depths indicated the LC and its deep warm layers as it was in the process of shedding a mesoscale WCR in August and September 2005. A cold core ring (CCR) that advected cyclonically around the shed WCR may have helped weaken Rita before landfall. Walker *et al.* (2005) also found that Ivan may have encountered a CCR prior to landfall. These studies point to the

importance of initializing coupled models with realistic warm and cold ocean features in the global oceans (Ali *et al.* 2007; Ito *et al.* 2014; Lin *et al*. 2008; 2009a; Halliwell *et al.* 2008; 2011 ;Wada *et al*. 2010a; 2010b; 2013a; 2013b; 2014; Chen *et al*. 2010; Sandery *et al.* 2010; Zheng et al. 2008).

4.4.2.1 Oceanic Thermal and Biological Responses

Walker *et al.* (2005) showed that the SST response was modulated by both WCR and CCR in the Gulf of Mexico during Ivan's passage (Fig. 3). Up to 7^{o}C cooling was observed in the CCR due in part to upwelling associated with TC Ivan's wind stress curl. Upward isotherm displacements of up to 65 m were documented from altimeter-derived surface height anomaly (SHA) and wind stress curl. This result was corroborated using a reduced-gravity model where for each 10 cm surface height change, the isotherm displacement is approximately 33 m. The observed 20 cm decrease in the SHA field may have been associated with the barotropic (sea-surface) trough in the cooling wake (Shay and Chang 1997). While this depressed sea surface and the SST cooling provided *negative feedback* to Ivan, the associated phytoplankton blooms in the wake had peak concentrations of chlorophyll A (Chl-a) exceeding 1 mg m^{-3} distributed over 13,000 km^{2} area detected from SeaWiFS imagery compared to background concentrations of less than 0.5 mg m^{-3}. This relative maximum occurred about 3 to 4 days following passage in the vicinity of the CCR. By contrast, the SSTs in the WCR only decreased by 1 to 2^{o}C during Ivan, consistent with previous studies.

In the wake of TC Ketsana (Oct. 2003) in the western Pacific ocean basin, SST imagery by the Advanced Microwave Sounding Radiometer (AMSR) and chlorophyll concentrations from the Moderate Resolution Imaging Spectro-radiometer (MODIS) were combined to assess the oceanic response (Yin *et al.* 2007). Based on post-storm measurements, Chl-a concentrations increased to 1.2 mg m^{-3} about 7 days after passage. This equates to more than an order of magnitude change induced by upwelling of nutrients from the cooler thermocline water. The maximum Chl-a level found was more than 3 mg m^{-3} in Ketsana's cold wake as this response persisted for more than two weeks following TC passage. Simulations using a Regional Ocean Modeling System with a Nitrogen-Phytoplanton-Zooplankton-Detritus (NPZD) biochemical model revealed levels of Chl-a of 0.4 to 1.7 mg m^{-3}, consistent with satellite estimates. The typhoon's wind stress curl induced significant upwelling into the OML and forced this large phytoplankton bloom. These results are in agreement with Walker *et al.* (2005) and Hanshaw *et al.* (2008). More recently, Lin *et al*. (2003) showed that the SST cooling response by a very slow moving TC can be as much as 9^{o}C cooling and accompanied by intense biological response of 10-30 times increase in satellite observed Chl-a in the South China Sea.

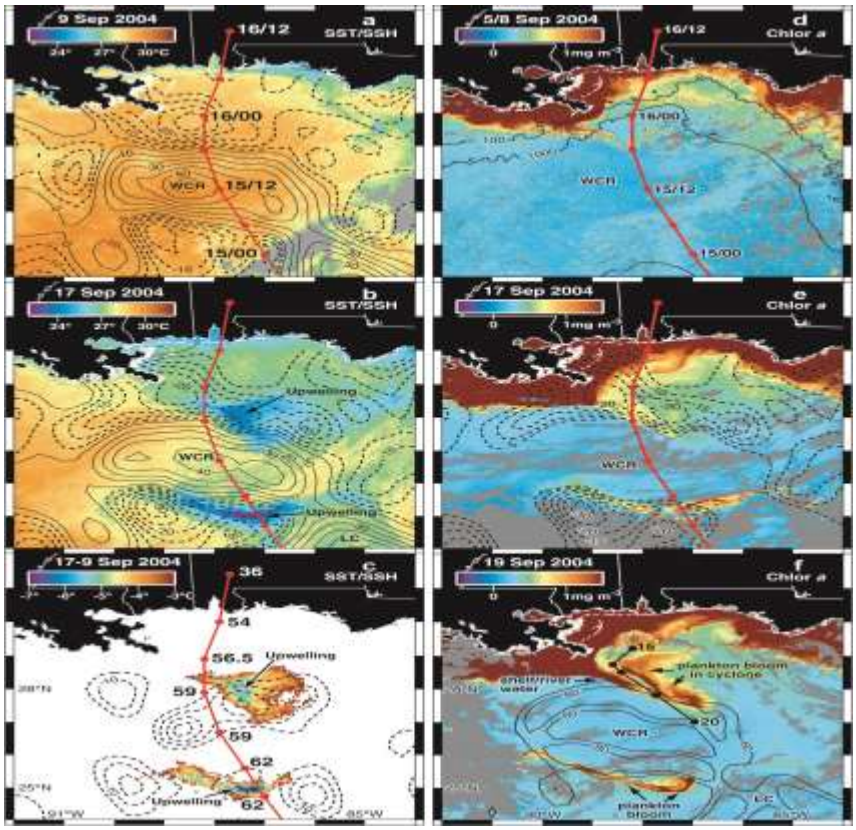

Figure 3: SSTs (color: ^{o}C) and SHA's (contours: cm) a) pre (9 Sept) and b) post Ivan (17 Sept) and c) SST and SHA differences where wind speeds from Ivan are shown in m s^{-1} and Chlorophyll a (mg m^{-3}: right panels) corresponding to similar days for d) pre, e) post and f) 19 Sept for corresponding isotachs derived from the SHA gradients (Combined from Figs 2 and 3 in Walker *et al.* 2005).

Lin (2012) systematically explored all typhoons passing over the western North Pacific main development region in a year. This approach is needed since most existing studies were based on case studies, emphasizing those with evident blooms. That study found only 2 out of 11 typhoons in a year can induce sizeable phytoplankton blooms as the TC-induced response is strongly affected by pre-existing nutricline depth, TC wind speed, translation speed and size (a much neglected parameter). Although individual cases may induce strong biological responses, actually 80% of typhoons over the western Pacific main development region do not induce strong bloom.

Park *et al.* (2005) combined ARGO float temperature and salinity profiles with satellite-derived SSTs to document the thermal response to TCs in the western Pacific Ocean (WPAC) over ten-day periods (Fig. 4). They found a high correlation of OML temperature changes and SSTs, and a strong dependence on both latitude and the initial OML depth. A key result was a negative correlation between OML depth change and when its initial depth exceeded 50 m (often a proxy for the Kuroshio's location and its WCR field). In the Kuroshio Current, the OML depth changes are less where the SST cooled by 1 to 2^{o}C. This result has consequences for both the genesis and the development of a mature TC underscoring the inherent oceanic variability in the vicinity of western boundary currents and their background eddy fields. Strong gradients in the OML depths and temperatures play a pivotal role in TC intensity changes discussed below.

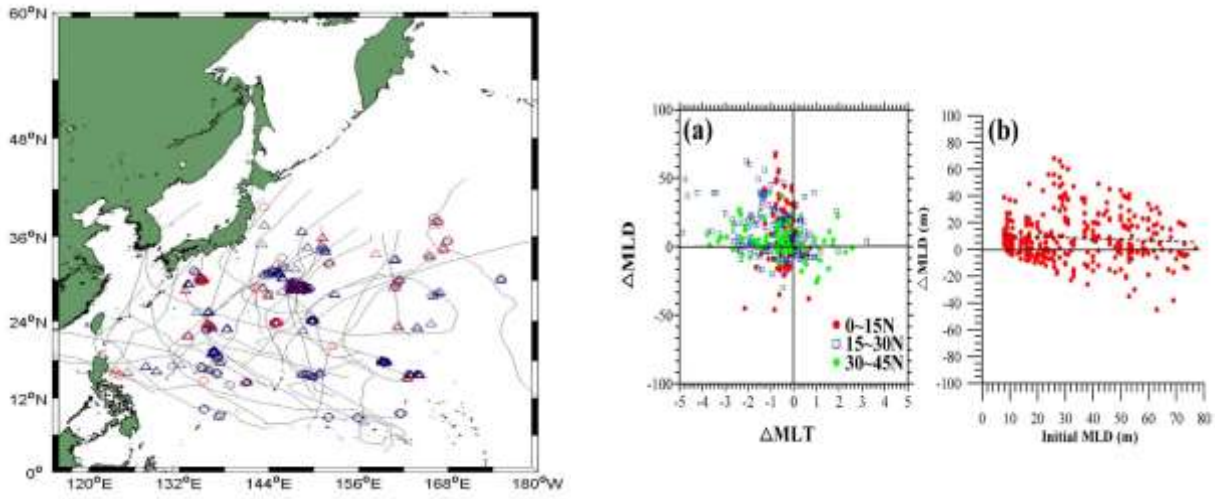

Figure. 4: Distribution of typhoon tracks (left panel) relative to the ARGO float pairs in the Western Pacific Ocean from 1999-2003 and scatter (right panels) for a) OML temperature change (ΔMLT: ^{o}C) and depth change (ΔMLD : m) binned by bands (red: 0-15^{o}N; blue 15-30^{o}N; green: 30-45^{o}N) and b) initial depth (MLD : m) and depth change (ΔMLD : m) (From Park *et al.* 2005).

During the ONR-CBLAST (2004), technology for measuring the ocean response to tropical cyclones using air-deployed instrumentation was advanced. Several varieties of floats and surface drifters were deployed into Hurricane Frances (2004) that measured the temperature, salinity and velocity ocean response (Black *et al.* 2007; Chen *et al*. 2007; D'Asaro *et al.* 2007; Sanford *et al.* 2007, 2011). The profiler data are sufficient to resolve the SST response where the cold wake with maximum cooling of 2.2^{o}C is clearly offset from both the center of the storm and from the strongest winds. Less cooling occurred on the left-hand side of the storm (0.8^{o}C) and under the central core (0.4^{o}C). The reduction in air-sea heat flux in the core due to this cooling is modest, only about 16%.

During the ITOP (2010) experiment, large amount (several hundred temperature profiles) of in situ observations was observed in the cold wake (oceanic thermal response) from multiple platforms during Fanapi (Mrvaljevic *et al.* 2013; D'Asaro *et al.* 2013). As shown in Fig. 5, more than 2.5^{o}C cooling was observed. Perhaps more interesting, though the SST cold wake (surface cold wake) recovered within few days after the passage of Fanapi, the capped, subsurface cold wake was able to last for another 3 weeks or so. These Lagrangian technologies when complemented with aircraft based measurements from synoptic grids (Eulerian) increase our ability to measure the oceanic parts of the TC system with the same resolution and accuracy as the atmospheric part.

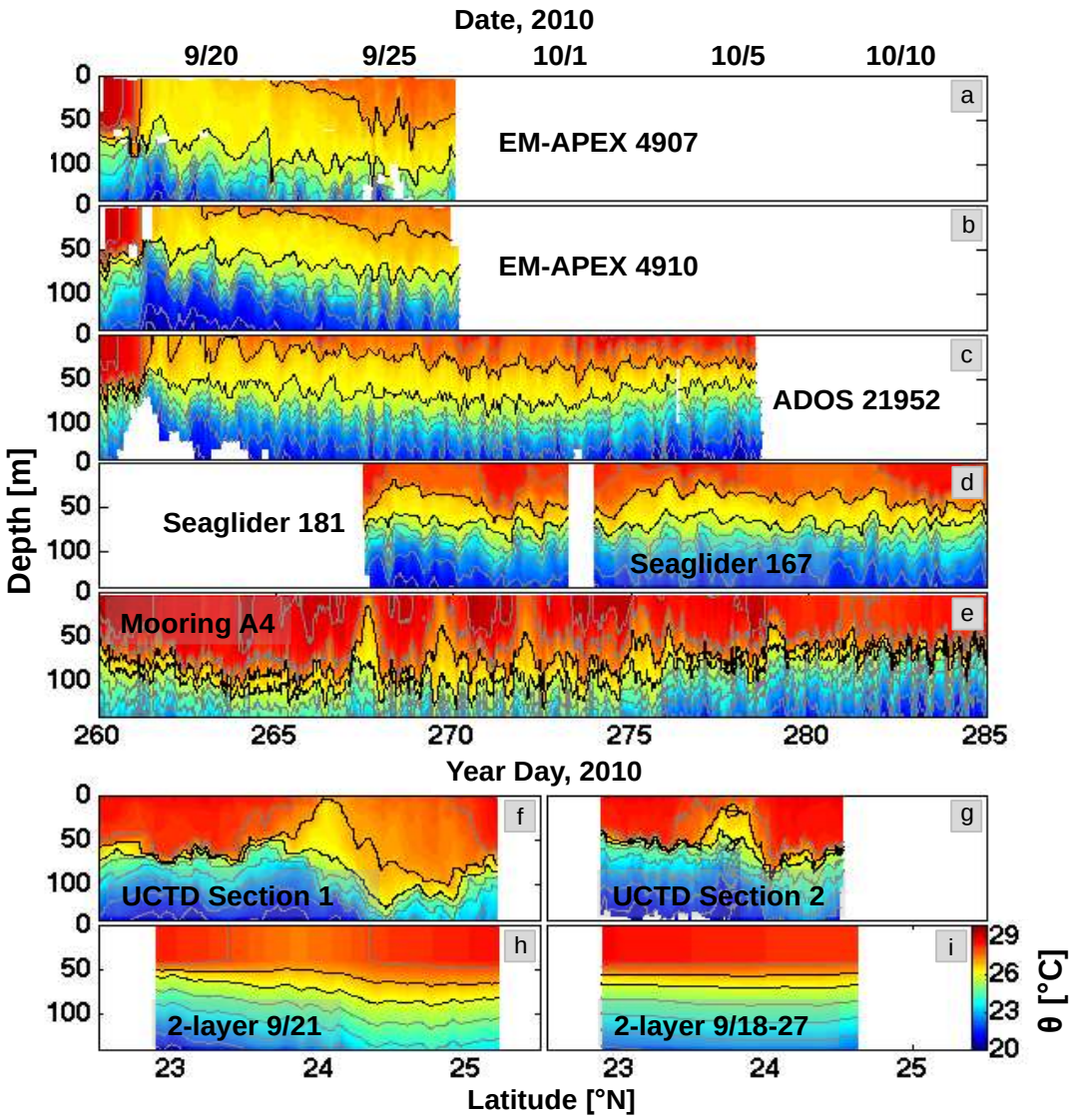

Figure 5: Potential temperature between 17 Sept and 12 Oct (contour interval 1°C) from selected floats and drifters (a-c), Seagliders (d) and a mooring (e). Wake cross sections from the ship-board CTD on 22 Sept (year day 265) (f) and 23 Sept (year day 266) (g) and from a 2-layer reduced gravity model estimate of the cross section using a single altimeter pass (track 203 of NASA's Jason-2 altimeter) on 09/21 (h), and using a 10-d map of surface height anomalies (SSHA) from 09/18 to 09/27 (i). The 26°C and 27°C isotherms (highlighted contours) show the thickness of the cold wake. Vertical displacements of the isotherms reflect storm-induced inertial motions (period ~30 hours) and internal tides, which are strong in this region. (After Mrvaljevic *et al*. 2013).

During the passage of Katrina and Rita in the Gulf of Mexico, Jaimes and Shay (2009, 2010) assessed the ocean thermal response using observations and the Miami Isopycnic

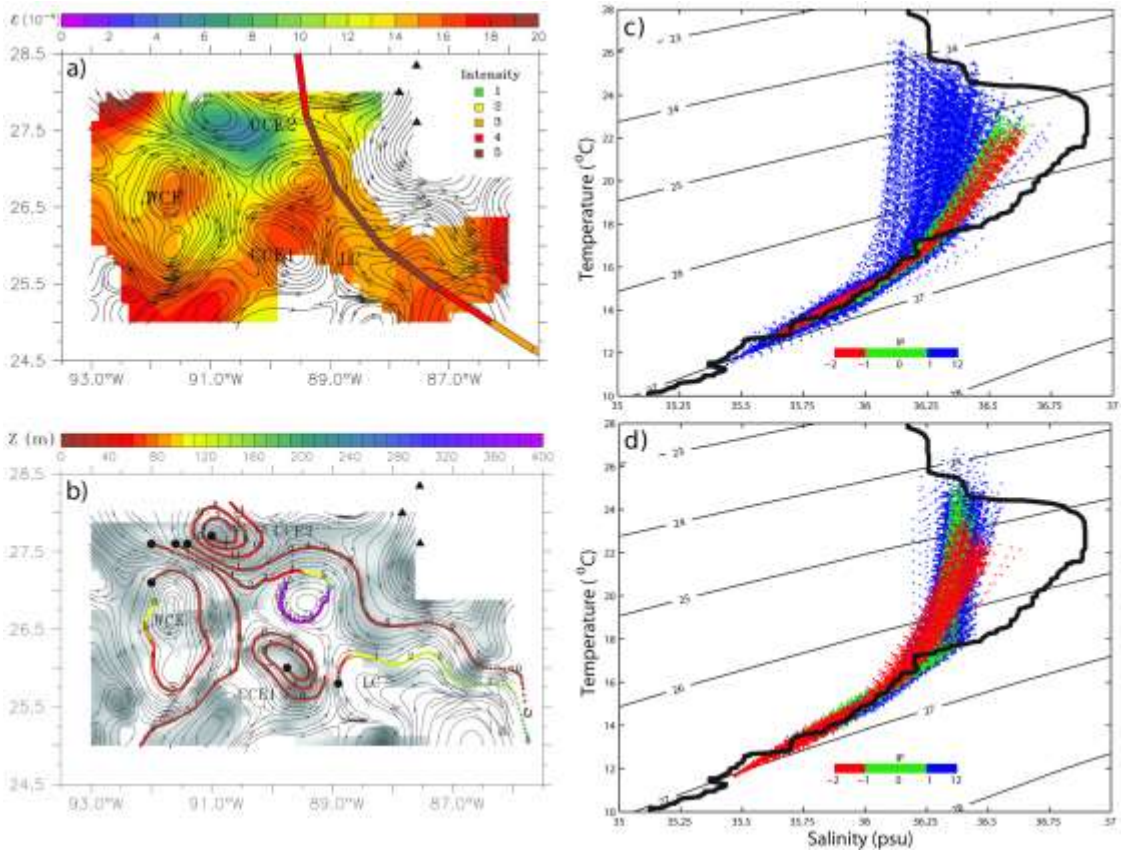

Figure 6: . Upper-ocean response to major hurricanes Katrina and Rita (Jaimes and Shay 2009, 2010). (a) Mixing parameter (ε) accounting for temperature differences between OML and thermocline waters (smaller values are associated with more mixing); cyclonic and anticyclonic eddies are labeled CCE and WCE, respectively; the storm's track is for Katrina. (b) 3-dimensional dispersion of NIOs (Near Inertial Oscillation) during the relaxation stage; Z is the depth at which NIOs are propagating; numbers on the wave rays are for inertial periods (approximately one day). (c) Water mass response to Katrina over a cyclonic geostrophic vortex. (d) Water mass response to Rita over an anticyclonic geostrophic vortex. Red, green, and blue color in (c, d) is for responses before, during, and after the passage of the storm; the black solid line is a typical profile over the LCt (warm anticyclonic geostrophic feature) during non-wind forcing conditions.

Coordinate Ocean Model (Jaimes *et al.* 2011). The assessment involved the levels of contrasting OML cooling responses in cyclonic and anticyclonic geostrophic oceanic eddies (Fig. 6), during both the forced stage (relatively short time scale when the TC is overhead), and relaxation stage in the wake of the storm where storm-generated near-inertial oscillations (NIO) propagate away from the storm's track. Based on these observational and model data in combination with a theoretical model (Stern 1965), it was found that contrasting OML cooling levels can develop over geostrophically balanced eddies because the upwelling response is a function of the underlying geostrophic relative vorticity (ζ_g). Upwelling (downwelling) regimes were found to predominantly develop in

regions where the wind stress vector is with (against) geostrophic OML currents; the upwelling response was a function of the curl of wind-driven acceleration of OML currents rather than just a function of the wind stress curl (Jaimes and Shay 2009; Jaimes *et al.* 2011). The impact of ζ_g extended to the relaxation stage: NIO dispersion was found to be a function of ζ_g that affected the distribution of momentum, vertical shear, and mixing in the upper ocean. The OML cooling response was reduced over regions of anticyclonic ζ_g, as near-inertial shear instability vanished because NIOs rapidly propagated into the thermocline (Fig. 6b). By contrast, cooling induced by vertical mixing was intense over regions of cyclonic ζ_g because NIOs were trapped in OMLs that increased vertical shear instability at the layer base. This anticyclonic circulation may impact the location and magnitude of the hurricane-induced sea surface cooling. Yablonsky et al. (2013) showed when a WCR is located to the right of the storm track (in the Northern Hemisphere), the interaction of the WCR's circulation with the hurricane-induced cold wake can cause increased SST cooling under the storm core and decreased storm intensity relative to the scenario where no WCR is present at all. They concluded that the presence of a WCR may create a less favorable condition for hurricane intensification.

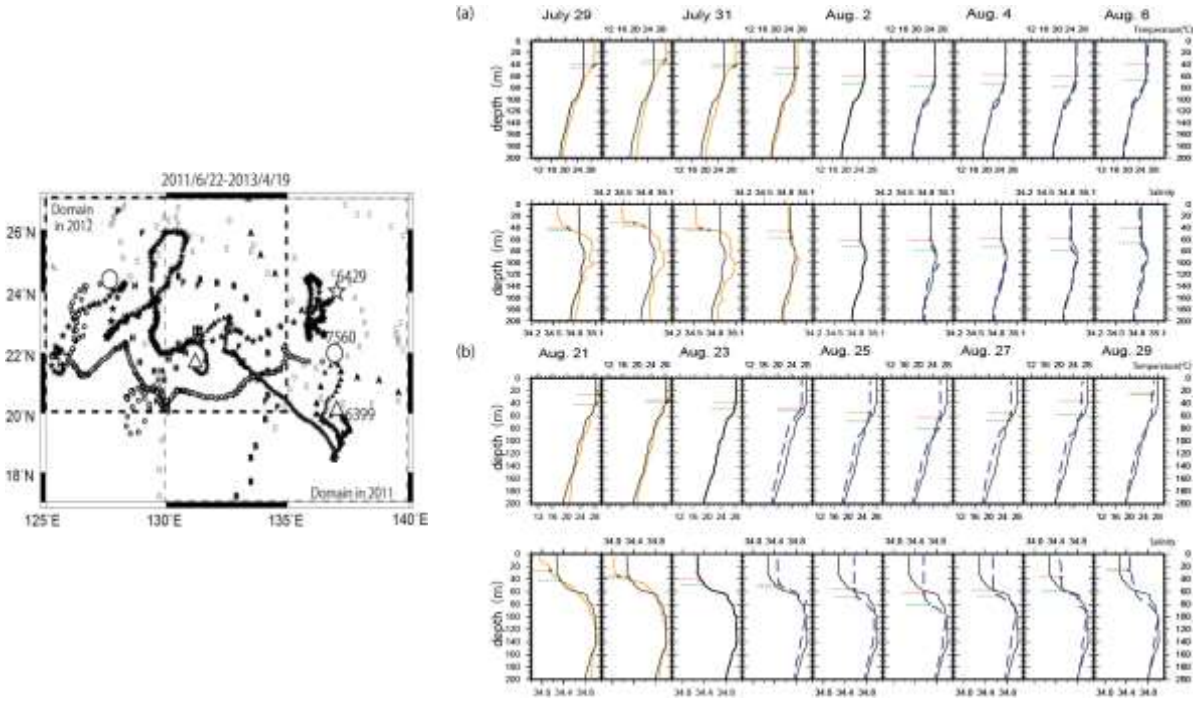

Figure 7: Left panel shows trajectories of the three profiling floats from 22 June 2011 to 19 April 2013. Right panel shows vertical profiles of the water temperature and salinity in the vicinity of the typhoon track (from Wada *et al*., 2014).

Wada *et al.* (2014) investigated the thermal response to typhoons during the 2011 and 2012 typhoon seasons using daily observations from three profiling floats deployed in the western North Pacific. Daily observations showed that the SST cooled by more than 2°C in

typhoons Ma-on and Muifa in 2011, and typhoons Bolaven and Parapiroon in 2012. The response varied between differing float locations relative to the TC center, that is, the response within 100 km of the typhoon center was different to the response more than 100 km from the center on the right- or left-hand sides of the typhoon track, even though the response was affected by pre-existing oceanic conditions, precipitation, and the typhoon intensity.

In Yablonsky et al. (2014) modeling study, the 2013 operational version of HWRF is used to analyze the Princeton Ocean Model (POM)-TC thermal response in retrospective HWRF/POM-TC forecasts of Atlantic Hurricanes Earl (2010), Igor (2010), Irene (2011), Isaac (2012), and Leslie (2012) against remotely sensed and in situ SST and subsurface ocean temperature observations. The model generally underestimates the hurricane-induced upper-ocean cooling, particularly far from the storm track, as well as the upwelling and downwelling oscillation in the cold wake, compared with observations. Nonetheless, the timing of the model SST cooling is generally accurate (after accounting for along-track timing errors), and the ocean model's vertical temperature structure is generally in good agreement with observed temperature profiles from AXBTs.

4.4.2.2 Oceanic Current Response

Observations of the ocean current response to TC passage have been generally sparse over the global oceans as the community has had to rely on fortuitous encounters with buoys and moorings deployed in support of other experiments or ships crossing TC wakes (Shay and Elsberry 1987; Church *et al.* 1989; Teague *et al.* 2007; Zedler *et al.* 2001). Using a network of high frequency radar stations (Yoshikawa *et al.* 2006), a strong wind-driven current response was observed during typhoon Mari's passage in the Tsushima Strait. Surface currents have also been shown to impact the direction of the surface wind stress (Drennan and Shay 2006). The divergent surface velocity response exceeded 50 cm s^{-1}, which is indicative of a 3-D response and upwelling processes (Yablonsky and Ginis 2009; Halliwell *et al*. 2011). Wind-forced currents directly affect the thermal, haline and mass field response to TC passage. Recent airborne field experiments to measure the momentum and thermal response during TC passage are listed in Table 1.

A fortuitous encounter occurred during TC Ivan (2004) over an array of moored Acoustic Doppler Current Profilers (ADCP). Fourteen moorings were deployed about 180 km south of Mobile, Alabama as part of the Slope to Shelf Energetics and Exchange Dynamics (SEED) project from early May through early Nov 2004. During the period of deployment TC Ivan passed directly over these ADCP moorings (Teague *et al.* 2006, 2007), which provided the temporal evolution of the 3-D current (and shear). The current response at Ivan moorings is shown in Fig. 8 for the near-inertial wave band where the local inertial period (IP) is ~24 h at 30^{o}N. Profiler data started at a depth of 50 m and extended to 500 m at 4-m intervals. Profiles at 1.5 Rmax to the right of Ivan's track indicate a clear downward propagation of the baroclinic energy ($\mathbf{V_g}$) from the wind-forced OML current into the thermocline, consistent with an upward propagating phase velocity ($\mathbf{V_p}$). Baroclinic

motions, which are the most energetic part of the ocean's momentum response to a moving TC, have a characteristic time scale for the phase of each mode to separate from the OML current structure when the wind stress scale ($2R_{max}$) exceeds the deformation radius of the first baroclinic mode (~ 30 to 40 km) (Gill 1984). This time scale increases with mode number due to decreasing phase speeds. This vertical propagation is primarily associated with the predominance of the anticyclonic-rotating (clockwise in northern hemisphere) energy of the NIOs (Shay and Jacob 2006). The ratio of the anticyclonic to cyclonic energies range from values of 3 to 4 is indicative of a preference for downward energy propagation from the OML. The corresponding vertical energy flux indicated an average value of ~2 ergs cm^{-2} s^{-1}, which was similar to that estimated from NIO in a frontal regime by Kunze and Sanford (1984).

TC	Basin	Year	Instrument(s)	References
Norbert	EPAC	1984	AXCP	Sanford *et al.* (1987)
Josephine	WATL	1984	AXCP	Sanford *et al.* (1987)
Gloria	WATL	1985	AXCP Drifters	Black *et al.* (1988); Price *et al.* (1994)
Gilbert	GOM	1988	AXCP	Shay *et al.* (1992)
Dennis	WATL	1998	OML Floats	D'Asaro (2003)
Isidore /Lili	GOM	2002	AXCP AXCTD	Shay and Uhlhorn (2008)
Frances	WATL	2004	EMAPEX OML floats	Sanford *et al.* (2007); D'Asaro et al. (2007)
Katrina/Rita	GOM	2005	AXCTD AXCP	Jaimes and Shay (2009)
Gustav	GOM	2008	EMAPEX OML floats	
ITOP	WPAC	2010	EMAPEX OML floats	D'Asaro et al. (2013)
Isaac	GOM	2012	AXCTD AXCP	Jaimes and Shay (2014)

Table 1: Summary of aircraft field programs where currents and shears were observed during TC passage where EPAC-Eastern Pacific Ocean, WATL-Western Atlantic Ocean, GOM-Gulf of Mexico, AXCP-airborne expendable current profiler, AXCTD- airborne expendable conductivity temperature and depth profiler, EMAPEX-Electro-Magnetic Autonomous Profiling Experimental Floats, Ocean Mixed Layer Floats.

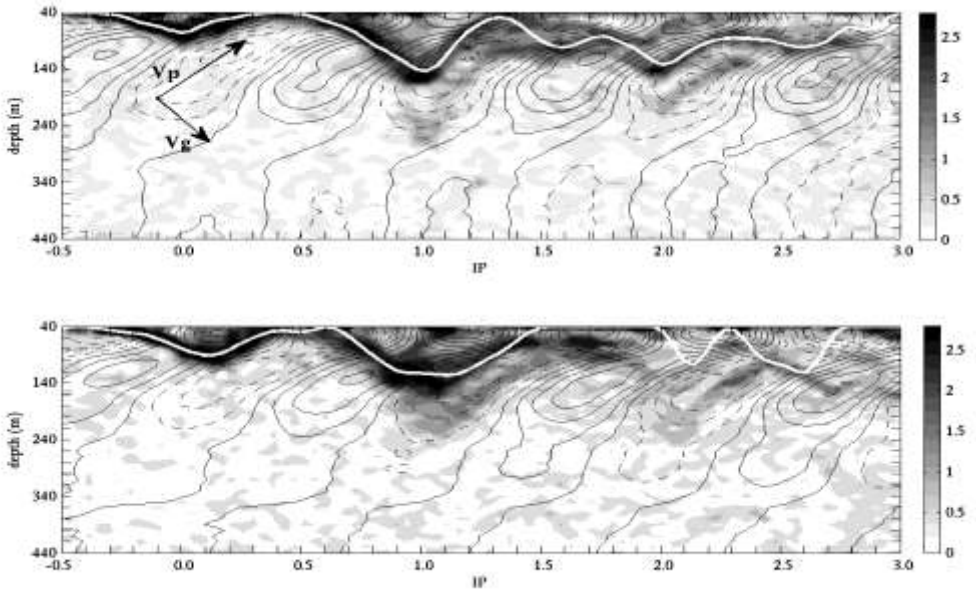

Figure 8: Band-pass filtered cross-track current structure along the track (upper panel) and at $1.5R_{max}$ (lower panel) contoured at 5 cm s^{-1} with t = 0 the time of TC Ivan's passage and the time axis normalized by the inertial period (~1 day). Heavy solid line represents the depth of the magnitude of the maximum shear (gray shade x 10^2 s^{-1}). Arrows represent upward phase (**Vp**) with downward group velocity (**Vg**) indicative of downward propagating waves into the thermocline. Time interval spans 15-19 Sept (Data courtesy Naval Research Laboratory).

Near-inertial current shears are central to the oceanic cooling by lowering the bulk (gradient) Richardson numbers to < 1 (0.25) and forcing the OML to deepen through instabilities. Uhlhorn and Shay (2012, 2013) documented the magnitude of the observed current shears from several experiments listed in Table 1. A value of 1.4 x 10^{-2} s^{-1} was found from TC Lili measurements in the LC to as high as 3.5 x 10^{-2} s^{-1} in the GCW during TC Gilbert. In the regime influenced by TC Ivan with relatively shallow OML, the shear is nearly three times larger than that observed in the LC system. Higher vertical shear levels were observed from the EM/APEX floats deployed in TC Frances (Sanford *et al.* 2005; 2007). As shown in Fig. 9, higher current shear levels forced mixing events during Frances passage by essentially lowering the gradient Richardson number to below 0.25 ($S^2 - 4N^2 > 0$) across the base of the OML at 1 to 2Rmax to the right of the track. During this period of intense forcing, strong near-inertial currents were excited by the TC of up to 1.6 m s^{-1} which created the vigorous shears (Sanford *et al.* 2007). Cooling level in TC Frances was ≈ 2.2 ^{o}C (D'Asaro *et al.* 2007).

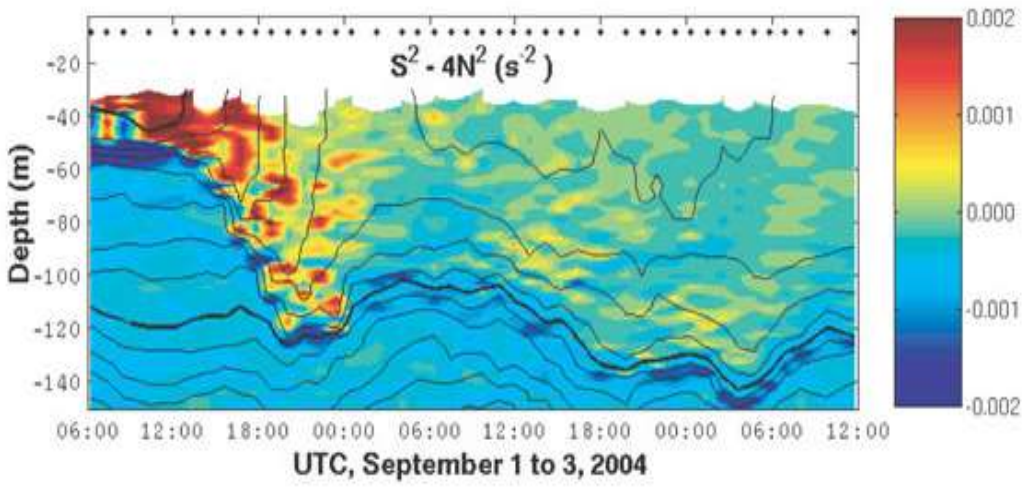

Figure. 9: Reduced shear (color: s^{-2}) based on the gradient Richardson ($Ri = N^2 S^{-2}$ where N is the buoyancy frequency and S is the shear) and the temperature (contours: ^oC) contoured at 0.5^oC intervals number where the heavy black contours represent 29 and 25^oC during and subsequent to Frances. The shear instability criterion is simply rewritten as $S^2 - 4N^2 > 0$ to represent mixing events (values greater than 0) in yellow and red. Blue colors represent stable conditions. Analysis is based on data from one EM/APEX float described in Sanford *et al.* (2005; 2007). The time of the closest approach of TC Frances was at 1700 UTC 1 Sept 2004.

4.4.3: Oceanic Background States and Parameterizations

4.4.3.1 Background Ocean States

Background oceanic flows that are set up by horizontal pressure gradients due to T(z) and S(z) may play a significant role in altering the development of strong wind-driven current shears within the LC/WCR complex as suggested (Shay and Uhlhorn 2008). Pre- and post-Isidore measurements across the Yucatan Strait indicate strong density and pressure gradients that are associated with the northward-flowing LC at speeds of up to 1 m s^{-1}. In the post-Isidore case, the horizontal gradients were sharpened since the storm cooled the Yucatan shelf waters by more than 4^oC compared to less than 1^oC across the Yucatan Strait. Here, strong horizontal advection of the thermal and salinity gradients through this regime impacted the oceanic response within the LC. Falkovich et al. (2005) and Yablonsky and Ginis (2008) introduced an approach for feature-based ocean model initialization in coupled forecast models that involves cross-frontal "sharpening" of the background temperature and salinity fields according to data obtained in field experiments, which allows specifying the LC position in the GOM using observations.

Briefly, the LC is a highly variable ocean feature in time as it can penetrate ~500 km northward of the Yucatan Strait. Recurring WCR shedding events with peak periods from 6 to 11 months (Sturges and Leben 2000) occur when CCRs are located on the LC

periphery prior to separation. These WCRs, with diameters of ~200 km, propagate west to southwest at phase speeds of 3 to 5 km d^{-1} (Elliot 1982), and can remain in the Gulf of Mexico for several months. In this LC regime, OHC values relative to the 26°C isotherm exceed 100 kJ cm^{-2} (Leipper and Volgenau 1972). Such OHC levels are resistive to storm-induced cooling by wind-driven current shears across the OML base.

The OML response to Hurricane Lili within and immediately adjacent to the Gulf of Mexico LC was examined in Uhlhorn and Shay (2012; 2013). A set of temperature, salinity, and current profiles acquired from aircraft-deployed expendable probes is utilized to analyze the 3-D oceanic energy evolution in response to TC Lili's (2002) passage. The OML thermal analyses showed that the LC cooled by ~1°C in response to the storm, in contrast to typically observed larger decreases of 3°–5°C. Correspondingly, vertical current shear associated with mixed layer currents, which is responsible for entrainment mixing of cooler water, was found to be up to 50% weaker, on average, than observed in previous studies within the directly forced region. The LC, which separates the warmer, lighter Caribbean Subtropical Water from the cooler, heavier Gulf Common Water, was found to decrease in intensity by -0.18 +/- 0.25 m s^{-1} over an approximately 10-day period within the mixed layer. Contrary to previous ocean response studies, which have assumed approximately horizontally homogeneous ocean structure prior to storm passage, a kinetic energy loss of 5.8 +/- 6.4 kJ m^{-2}, or approximately ~1 wind stress-scaled energy unit, was observed. By examining near-surface currents derived from satellite altimetry data, the LC is found to vary similarly in magnitude over such time scales, suggesting storm-generated energy is rapidly removed by the preexisting LC.

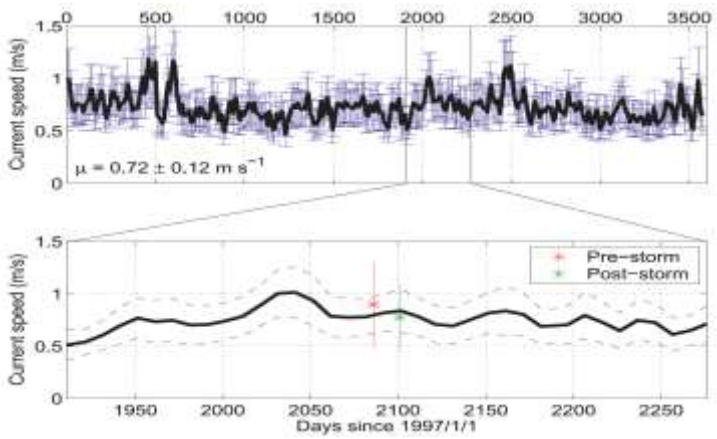

Figure 10: (a) 10-yr time series of LC current (mean and standard deviation) through the Lili observation region derived from satellite radar altimetry, and (b) 1-yr record centered at time of Lili's passage. Pre-storm and post-storm |**V**| within the LC estimated from the objectively analyzed fields are plotted for comparison (from Uhlhorn and Shay 2012).

The details of the upper-ocean response within an idealized baroclinic current to a translating TC were examined in a series of nonlinear, reduced-gravity numerical simulations (Uhlhorn and Shay 2013). The preexisting ocean mass and momentum fields are initialized with a Gulf of Mexico LC–like jet, which is subsequently forced by a vortex whose wind stress field approximates that observed in the Lili experiments. Because of 1) favorable coupling between the wind stress and preexisting current vectors, and 2) wind-

driven currents flowing across the large horizontal pressure gradient, wind energy transfer to the mixed layer can be more efficient in such a regime as compared to the case of an initially horizontally homogeneous ocean. However, nearly all energy is removed by advection and wave flux by two local inertial periods after storm passage, consistent with these observational results.

Data assimilative ocean nowcasts are an effective method for providing initial and boundary conditions to the ocean component of nested, coupled TC prediction models. The thermal energy available to intensify and maintain a TC depends on both the temperature and thickness of the upper ocean warm layer. The ocean model must be initialized so that ocean features associated with relatively large or small OHC values are in the correct locations and T-S (and density) profiles, along with the OHC, are realistic. Ocean nowcast-forecast systems based on HYCOM (Chassignet *et al.* 2003; Halliwell 2004) were evaluated in the northwest Caribbean and eastern Gulf of Mexico for September 2002 prior to Hurricanes Isidore and Lili and for Sept. 2004 prior to Hurricane Ivan (Halliwell et al. 2008). In this region, the OHC distribution associated with the LC/WCR complex as well as coastal upwelling was initialized for the ocean model. In this context, measurements are critically important not only for assimilation, but to evaluate initial and boundary ocean fields. Assimilation of the storm stage *in-situ* AXBT observations was found to have modest improvement on the coupled model track and intensity forecasts and the SHIPS intensity forecasts (Sanabia *et al*. 2013).

A new ocean OSSE (Observing System Simulation Experiment) system initially developed and evaluated in the Gulf of Mexico (Halliwell *et al*. 2014a) has been used to test the impact of rapid-response airborne profile surveys for improving ocean analysis products used for model initialization (Halliwell *et al*. 2014b). The OSSE system permits different sampling strategies to be tested using ocean models alone. Positive impacts were demonstrated for conducting surveys on two back-to-back days instead of a single day, for using deep AXCTDs instead of shallow AXBTs, and for increasing horizontal profile resolution to < 1º latitude and longitude. The latter result is illustrated in Fig. 11 where synthetic 1000m AXCTD profiles were simulated from a Nature Run (NR) stipulated to represent the true ocean over the open Gulf, and then assimilated into another ocean model. Three experiments, one that assimilates all observations including profiles on the 0.5º grid (Fig. 11a), one that assimilates all observations including profiles on a 1.0º, and one that denies all airborne profiles, demonstrate this impact (Fig. 11b,c). Denial of all airborne profiles increases RMS errors in OHC (or Tropical Cyclone Heat Potential : TCHP) and sea surface height anomalies (SSHA) with respect to the NR by ~50%. Substantial error increases result when horizontal profile resolution is reduced to 1.0º, more for TCHP than for SSH. Altimetry assimilation can constrain the broad structure of mesoscale ocean features (eddies and boundary currents), but the assimilation of airborne profiles has high value in constraining smaller-scale structure (e.g. the frontal boundaries separating these ocean features) with scales <1.0º.

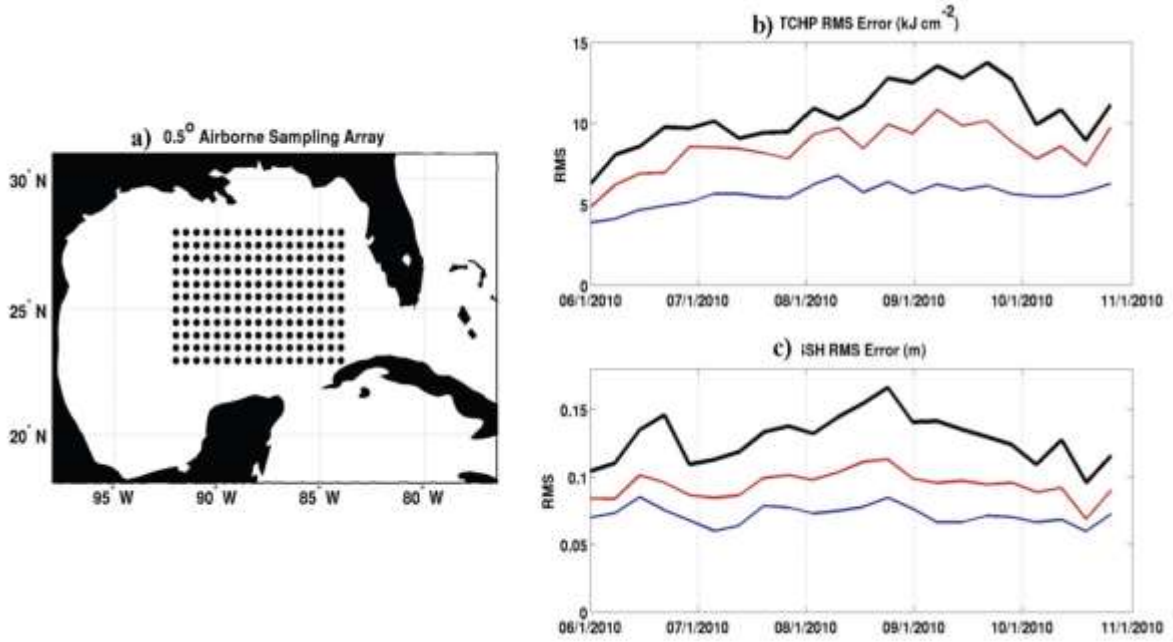

Figure 11. (a) Synthetic airborne profile locations with 0.5º resolution in both latitude and longitude. Time series of RMS error with respect to the Nature Run at all model grid points within the region containing the synthetic profile locations from analyses separated by 7 days for (b) TCHP and (c) SSHA. RMS errors are presented for an experiment that assimilated all observations except airborne profiles (black), one that also assimilated all airborne profiles on the 0.5º grid (blue), and one that also assimilated profiles on a 1.0º grid consisting of alternate points of the 0.5º grid (red).

4.4.3.2 Vertical Mixing Parameterization

One of the significant effects on the upper-ocean heat budget and the fluxes to the atmosphere is the choice of entrainment mixing parameterizations (Jacob *et al.* 2000; Wada *et al.* 2009; Halliwell *et al.* 2011). Halliwell *et al.* (2011) conducted sensitivity tests using five schemes: K-Profile Parameterization (KPP: Large *et al*. 1994); Goddard Institute for Space Studies Level-2 closure (GISS: Canuto *et al.* 2001, 2002); Level-2.5 turbulence closure scheme (MY: Mellor and Yamada, 1982); quasi-slab dynamical instability model (PWP: Price *et al*. 1986); and the turbulent balance model of Gaspar (KT: 1988) that is a modified version of Kraus and Turner (1967). For quiescent ocean initial conditions, the range of fluxes in the directly forced region of Hurricane Ivan exceeds 500 Wm^{-2} for these five schemes.

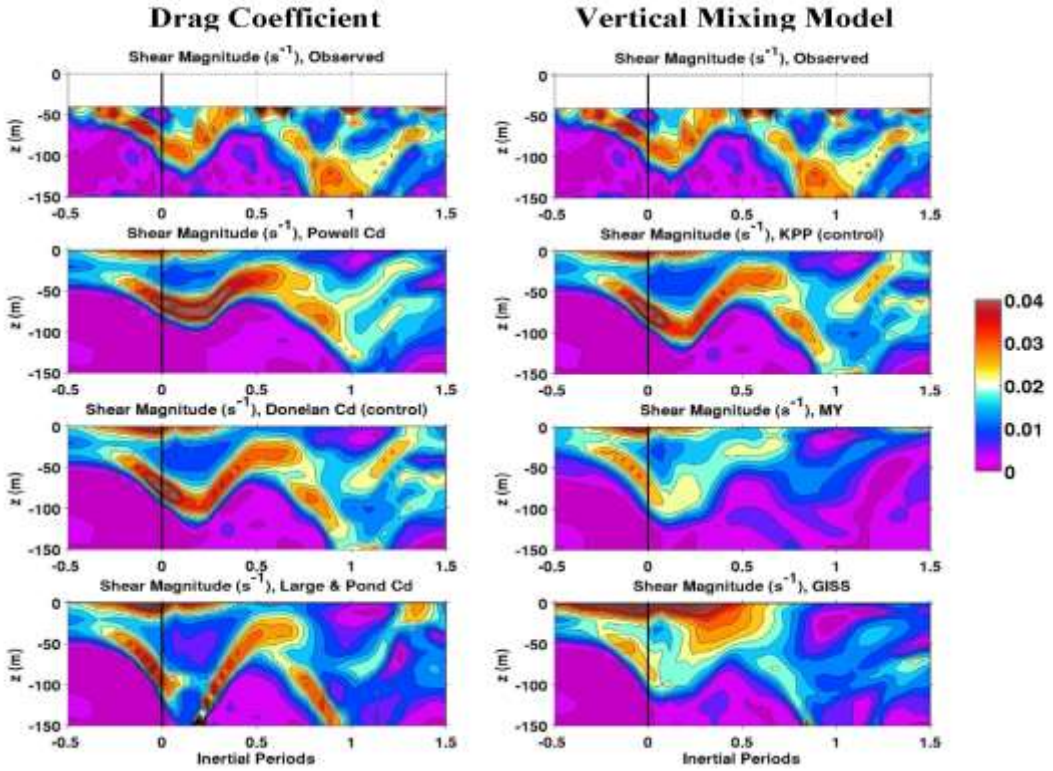

Figure 12: Time series of the magnitude of vertical current shear (s^{-1}) comparing observations from SEED mooring 9 (upper panels) to three wind stress drag coefficient choices (left) and vertical mixing choices (right) over two inertial periods. The black line represents the time of Ivan's closest approach to the mooring (t=0). The combination of KPP mixing scheme and Donelan *et al.* (2004) drag coefficient parameterization produce the most realistic shear structure and maximum OML depth relative to the data. Note that the quality ADCP data started at about 40 m which avoids surface interference effects.

Halliwell *et al.* (2011) conducted a series of sensitivity tests using the Hurricane Ivan data as a guide to understand the impact of both surface drag coefficients and vertical mixing parameterizations in HYCOM. They directly compared both the current and current shears measured at one of the moorings located about 1.5 Rmax to the right of the track. Of particular interest, the shear magnitudes revealed very high correlations with the HYCOM model using the KPP mixing scheme with the Donelan *et al.* (2004) drag coefficient over the first two inertial periods (Fig. 12). Shear comparisons reveal differences among the three vertical mixing schemes evaluated in KPP, MY and GISS as well as the surface drag coefficient parameterizations of Donelan *et al*. (2004), Powell *et al*. (2003) and Large and Pond (1981). Based on these comparisons, KPP mixing scheme with the Donelan drag coefficient are the schemes of choice for the Ivan data set. We are in the process of making such comparisons for all the ADCP records during storm forcing period. The import of this surface drag coefficient parameterization and surface stress drives the current and its shear

that will lead to enhanced shear instabilities and entrainment mixing. Thus, these schemes are clearly linked in obvious and subtle ways to fluxes and TC intensity change.

The OML salinity evolution with and without precipitation forcing highlights the effect of precipitation on the upper ocean salt budget (Jacob and Koblinsky 2007). For the no precipitation case, OML salinity variability simulated by all the above mixing schemes was similar ahead of the storm center. In the PWP scheme, however, salinity increases significantly in the right-rear quadrant over the first half of an inertial period due to enhanced mixing. In other mixing cases, the simulated salinity evolution is similar with minimal changes in the KT model due to less intense mixing (no vertical shear). By including precipitation forcing, the salinity in the OML began to decrease about 0.5 IP before the storm with maximum freshening of the OML observed in the KT case. This freshening process due to enhanced precipitation increases static stability in the mixed layer, leading to a simulated salinity balance for PWP case that is more consistent with the other schemes. OML temperature and salinity evolution in cases with and without precipitation for PWP scheme indicates a mean temperature and salinity differences of 0.5^{o}C and 0.2 psu in the OML. An average freshening of 0.2 psu is seen in the wake of the storm in all the five cases when precipitation forcing was used. Precipitation temperatures have minimal effect on the salinity evolution in the OML. Simulated results from the higher order schemes did not differ significantly from each other. Freshening of the subsurface salinity or advection of low salinity from other nearby regions may induce the formation of barrier layer between the base of the mixed layer and the base of the isothermal layer. The barrier layer has a similar effect as a deep mixed layer in that it can inhibit the vertical mixing of cooler water below the mixed layer. The TC induced ocean cooling is thus less with barrier layer. Simulations show the TC intensity is stronger for TC tracks over pre-existing ocean barrier layers (Balaguru *et al.* 2012) or sequential TC tracks through the same area (Baranowski *et al*. 2014).

Other recent modeling studies have shown that enhanced vertical mixing, which has usually been identified as the dominant driver of the cold wake for strong TCs is actually found further than two radii of maximum wind speed (~100 km) away from the TC center (Jullien *et al*., 2012; Vincent *et al.*, 2012a,b). In contrast, right under the eye, the upwelling of deep cold water induced by Ekman pumping overwhelms the mixing-induced warming signal. Rabe *et al*. (2014) utilized a large eddy simulation (LES) to model the turbulence under Hurricane Gustav in an effort to better understand the importance of Langmuir turbulence (LT) during tropical cyclones. Comparison of LES results with Lagrangian float field observations indicate that LT plays an important role in upper ocean mixing. Cross sections of normalized vertical velocities in the LES simulations at two specific time points (Fig. 13) indicate that these velocities are much more organized and stronger with LT than without. Results suggest that without LT effects, simulated vertical velocity variance (VVV) underestimates the observed VVV from mixed layer floats. Consistent with observations, the LES predicts a suppression of VVV near the eye due to wind-wave misalignment. Investigation of temperature profile evolution reveals that LT enhances deepening, resulting in larger SST cooling compared with shear turbulence (ST). The

difference between the simulated SST cooling for LT versus ST is as much as a 1°C and cooling occurs earlier and more rapidly with LT than ST, which will have implications for accurately predicting tropical cyclone strength. This work suggests that LT critically influences upper ocean response during TCs that must be considered for accurate TC predictions.

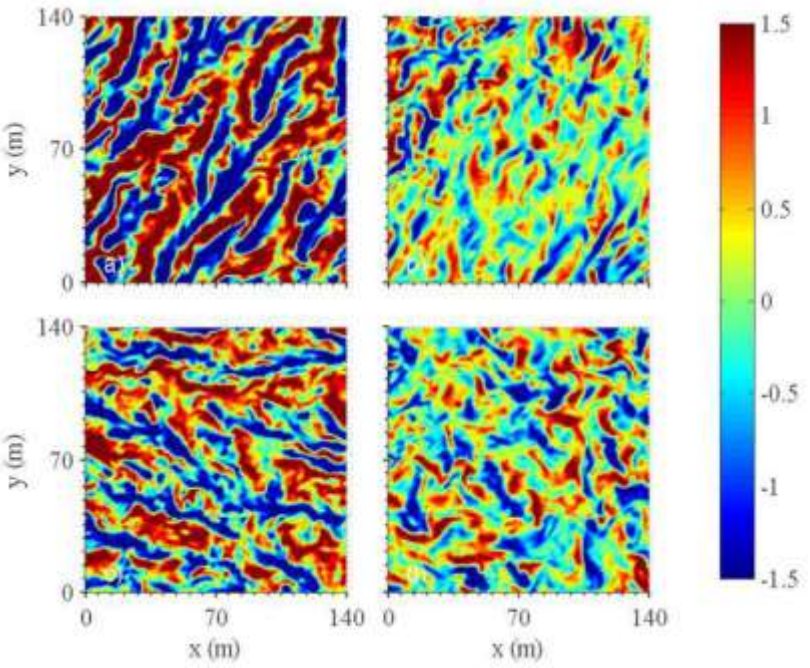

Figure 13: Cross sections of vertical velocity normalized by u^* in the LES simulations of Hurricane Gustav at two specific time points, day 245.115 (top) and 245.285 (bottom) for the LT (left) and shear turbulence (right). Cross sections are taken at the depth above z/h = −0.5 (From Rabe *et al.* 2014).

Under high wind speed conditions in the TC, the net effect of the Langmuir-induced mixing depends on the alignment of the wind and Stokes drift current and its vertical penetration. Langmuir mixing is strong when the alignment angle of wind and wave is small. When the alignment angle is large and the wind direction opposes the wave direction, the waves become steeper and break, which is a larger effect than the Langmuir mixing. Idealized large eddy simulations (LES) by Sullivan *et al.* (2012) suggested a 25% increase in turbulent mixing and a 0.25°C more cooling on the right side of the TC due to Langmuir mixing. By contrast, cooling is reduced on the left side of TC due to reduction of Langmuir mixing. The anticyclonic rotation of Langmuir cells and their associated Stokes currents have been found on the right side of TC. Rapid growth of Langmuir cells and a broad region of weak upwelling on the flank of cells occurred at the time of maximum wind. Shear-induced vertical mixing by the current and surface wave interaction has been parameterized as an additional TKE production terms from the vertical shear of the Stokes Drift Current (SDC) through the Langmuir turbulence (Kantha and Clayson 2004; Smith *et al.* 2013). The air-ocean-wave Coupled Ocean/Atmosphere Mesoscale Prediction System for Tropical Cyclone (COAMPS-TC) simulations showed the maximum magnitude of surface SDC is ~ 0.5 m s^{-1}, which accounts for 10-25% of the near-surface Eulerian current during Ivan.

4.4.3.3 SST versus OHC Estimates

If the upper-ocean warm layer is thick and has a large total OHC, the SST will decrease slowly during TC passage, the negative feedback mechanism (or "brake") will be weak, and the ocean will promote TC intensification. Several studies over the globe have now shown that OHC relative to the depth of the 26°C isotherm takes this into account and is a better indicator than a thin layer of high SST on TC intensification. Leipper and Volgenau (1972) estimated OHC (or TCHP) as:

$$\mathrm{OHC} = c_p \int_0^{D26} \rho\left[T(z) - 26\right]\, dz,$$

where c_p is specific heat at constant pressure (1 cal $gm^{-1}\ {}^{o}C^{-1}$), D26 is the 26°C isotherm depth, and OHC is zero wherever water above 26°C is not present. It is difficult to monitor the global oceans for isotherm depths, thermal structure and OHC given the relative paucity of *in situ* profiler measurements with perhaps the exception of the global ARGO float network. Thus, satellite remote sensing offers the optimal approach to infer isotherm depths and OHC variations. Measurements from radar altimeter missions (Fig. 14) of the SHA field from NASA TOPEX, Jason-1 and Jason-2, U.S. Navy Geosat Follow-On-Mission (GFO), Envisat, ERS-2, and SARAL (Cheney *et al.* 1994; Scharroo *et al.* 2005) and SSTs are used in a reduced gravity model (e.g., Goni *et al.* 1996) with hurricane season climatology (Mainelli *et al.* 2008). Since mesoscale ocean features only move a few km d^{-1}, altimeter-derived SHA locates warm (cold) features that are usually identified as positive (negative) values as observed during TC's Opal (Shay *et al.* 2000), Ivan (Walker *et al.* 2005; Halliwell *et al.* 2008), Katrina and Rita in the Gulf of Mexico (Mainelli *et al.* 2008 ; Jaimes and Shay 2009), Maemi (Lin *et al.* 2008, 2009a,b; Wu *et al.* 2007), Chaba and Songda (Wada and Usui 2007) in the western Pacific Ocean basin, and cyclones in the Bay of Bengal (Ali *et al.* 2007).

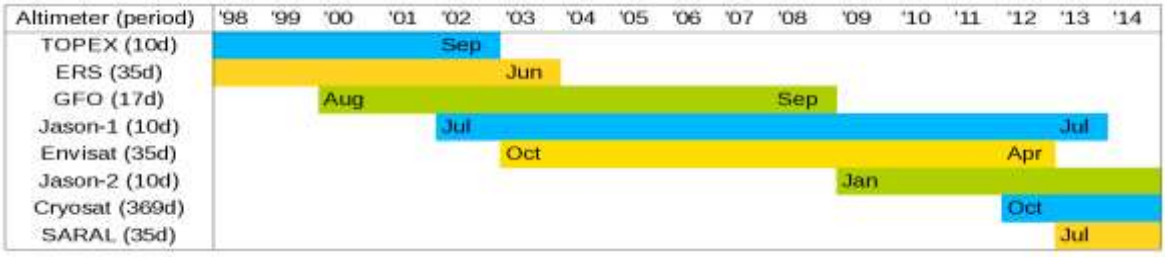

Figure 14: Bar chart showing time line of available SHA field from various altimetry platforms.

Ali *et al.* (2013a,b) studied the statistical relationship between cyclone intensity (CI) and SST in the tropical Indian Ocean (TIO; 30°S–30°N, 30°E–120°E) and concluded that satellite-derived SST (a skin temperature) is not a good indicator of CI. They suggested a more accurate parameterization of SST throughout the lifetime of a cyclone, for example, a parameter that also depends on OHC needs to be considered.

Several studies have related the maximum potential intensity (MPI) of a cyclone to SST. However, it is unclear why SST should influence only the peak wind speed and not instantaneous TC intensity (TCI), as a function of time, throughout a cyclone's life period. Ali *et al.* (2013a) studied 75 cyclones of TIO during 1998–2011 to explore the statistical relationship between SST (from the Tropical Rainfall Measuring Mission Microwave Imager) and CI (as estimates of maximum sustained winds from the best track data from the JTWC). Initially, they considered SST leading TCI by 1 day (0–24 hours). Only 34 TC's had a significant Pearson's correlation coefficient (r) at 95% level between TCI and SST (Fig. 15), impling that SST is not an adequate measure of TCI. Out of the 34 cyclones with significant r, 24 (71%) TC's had stronger negative r, varying between –1.0 and –0.5, 7 (20%) cyclones had weak negative r, varying between –0.5 and 0.0, and only 3 (9%) TC's had positive r. To study the impact of slow moving TC's, which may induce cooling due to upwelling, Ali *et al.* (2013a) also considered lead times of 2 days (24–48 hours) and 3 days (48–72 hours). Regardless of the lead-time, more than 50% of the TCs have negative r between TCI and SST.

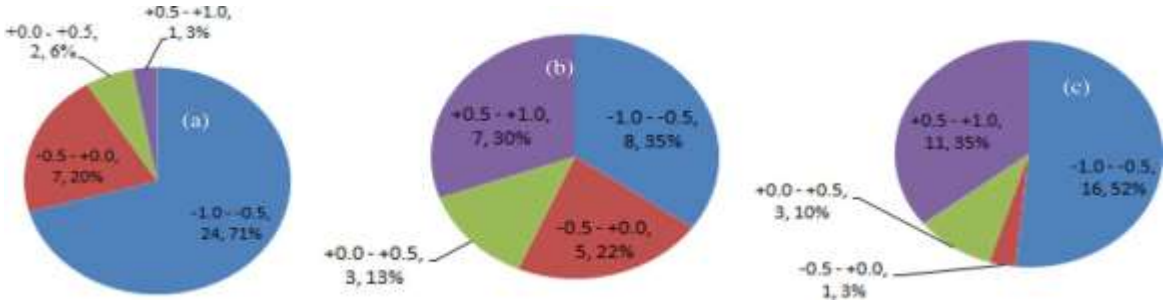

Figure 15: Pie chart of Pearson correlations (*r*) between CI and SST (with 95% confidence) from 34 cyclones for (a) one-day, (b) two-day, and (c) three-day lead times (SST leading CI). The first line in the chart represents the correlation range. The second line gives the number of cyclones and the percentage of the total number of cyclones (Ali *et al*. 2013a).

This leads to further development to revise the maximum Potential Intensity (PI) index, originally proposed by Emanuel (1988). As the existing PI (SST_based, called SST_PI) does not include ocean subsurface contribution, there was no distinction in the SST_PI of the 3 ITOP cases. However, when subsurface conditions are included in the revised PI estimation it is known as Ocean Coupling Potential Intensity (OC_PI; Lin *et al*. 2013). Clear distinction on the intensification potential among the 3 cases can be found. This newly-proposed revision of PI was further tested on nearly 150 TC cases over the western North Pacific over 1998-2011 (14 years). Evident improvement on TC intensity upper bound (PI) as compared to the observed peak intensity was obtained (Lin *et al.* 2013) (Fig. 16).

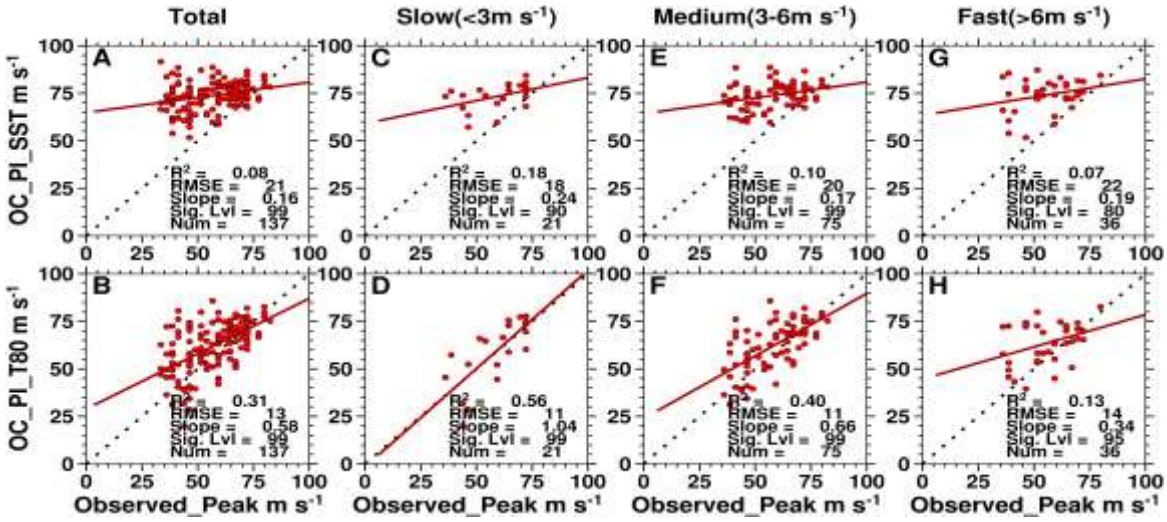

Figure 16: Scatter plots of observed maximum TC intensity from SST_PI (top row A,C,E,G) and OC_PI (bottom row B,D,F,H) as a function of translation speed. (After Lin *et al.* 2013).

Wada *et al.* (2012) investigated whether the maximum intensity of TC in the North Pacific Ocean depends on sea surface temperature (SST) and tropical cyclone heat potential (TCHP) or OHC. The study used reanalysis data sets for both the oceans and atmosphere: daily, 10-day, and monthly oceanic data sets; six-hour and monthly atmospheric data sets; and a daily satellite SST data set, for the July-to-October season from 2002 to 2005. For each TC, TCHP was summed from the time of genesis to the time of first reaching a minimum central pressure (MCP), to obtain an accumulated TCHP. In a linear regression analysis, the relationship between maximum TC intensity and accumulated TCHP differed between the eastern and western Pacific: high values of accumulated TCHP were needed before a TC attained a certain MCP in the western Pacific. In addition, the background convective available potential energy (CAPE) value was nearly four times larger in the western Pacific than in the eastern Pacific. The static stability was also 6.5% lower, the inertial stability 29.7% higher, and the size of tropical cyclones 38.2% larger in the western Pacific than in the eastern Pacific. The result indicated a deeper penetration depth and stronger TC in the western Pacific. Wada *et al.* (2012) evaluated TCHP values derived from three oceanic reanalysis data sets by using Argo profiling float observations. Only daily data can reproduce the TC-induced cooling effect, which caused a decrease in the TCHP values.

4.4.3.4 OHC Variability

Lin *et al.* (2005) point out the importance of the eddy-rich regime associated with the western boundary current or Kuroshio during the passage of typhoons over these oceanic features. In the western Pacific Ocean, the Kuroshio plays the same role as the LC and Gulf Stream in the western Atlantic Ocean basin (i.e., poleward advection of warm tropical

water). Using 13 years of satellite altimetry data, *in situ* Argo float subsurface ocean profiles, and a series of OML numerical experiments, Lin *et al.* (2008) found that the warm ocean eddies in the southern eddy-rich-zone of the western North Pacific Ocean represent 'boosters' for ST. As in all the other basins, warm mesoscale ocean eddies can provide much deeper subsurface warm layer and higher OHC. Thus, a TC's self-induced ocean cooling negative feedback to intensification can be effectively restrained and there can be sufficient air-sea enthalpy fluxes available for intensification even to ST status. Lin *et al.* (2009a) subsequently found that faster-moving typhoons can afford to intensify to the ST intensity at category-5 over relatively shallower layer of subsurface warm water (lower OHC) while slower-moving typhoons require much deeper subsurface warm layer (higher OHC) for intensification to cat-5. In Lin *et al.* (2009a), a new method was proposed to quantitatively estimate the required minimum upper OHC and the 26^{o}C isotherm depth for intensification to category-5 intensity according to the translation speeds. This is not surprising since *the time available for vertical mixing* increases (Greatbatch 1983) with slower moving storms. It is also a function of latitude and the strength of the underlying stratification.

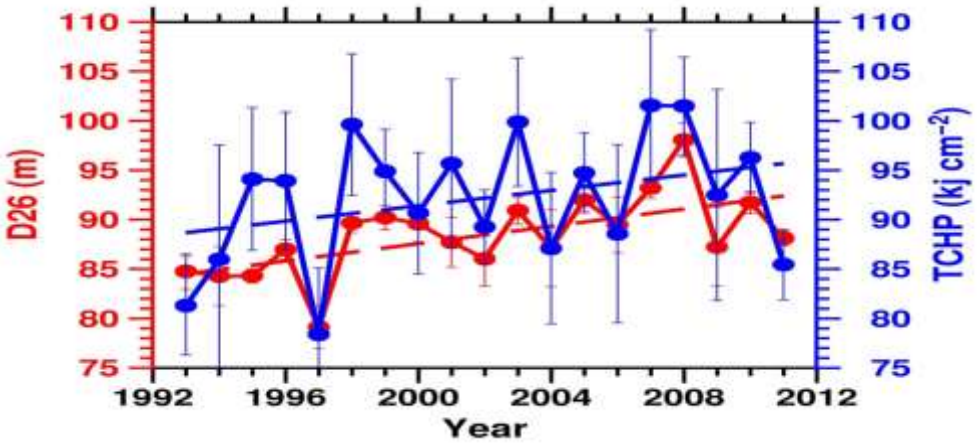

Figure 17: Western Pacific MDR domain-averaged D26 (in red, left axis) and TCHP (in blue, right axis) has increased by 12% in the past 2 decades. The error bars are standard deviations. The D26 (TCHP) curve passes 99% (80%) statistical significance test (After Pun *et al.* 2013).

Pun *et al*. (2013) reported that background ocean subsurface condition over the western North Pacific Main Development Region (MDR) is evidently warming in the past 2 decades, with current (2013) OHC increased by ~ 12% as compared to the early 90's (Fig. 17). This warming has been found to link to the intensification of ST Haiyan (2013). In addition, there has been a rapid enlargement in regions of high OHC > 100 kJ cm^{-2} (a condition favorable for ST). It has been observed that the high OHC/TCHP region has increased from covering 20% of the MDR region in the early 90's to the current (2013) 35%.

Wada and Chan (2008) found that the OHC (or TCHP) relative to 26^{o}C isotherm depth was high (Fig. 18) over the region where TCs underwent rapid intensification (Wang and Zhou 2008). The Empirical Orthogonal Function (EOF) analysis showed three significant TCHP variations.

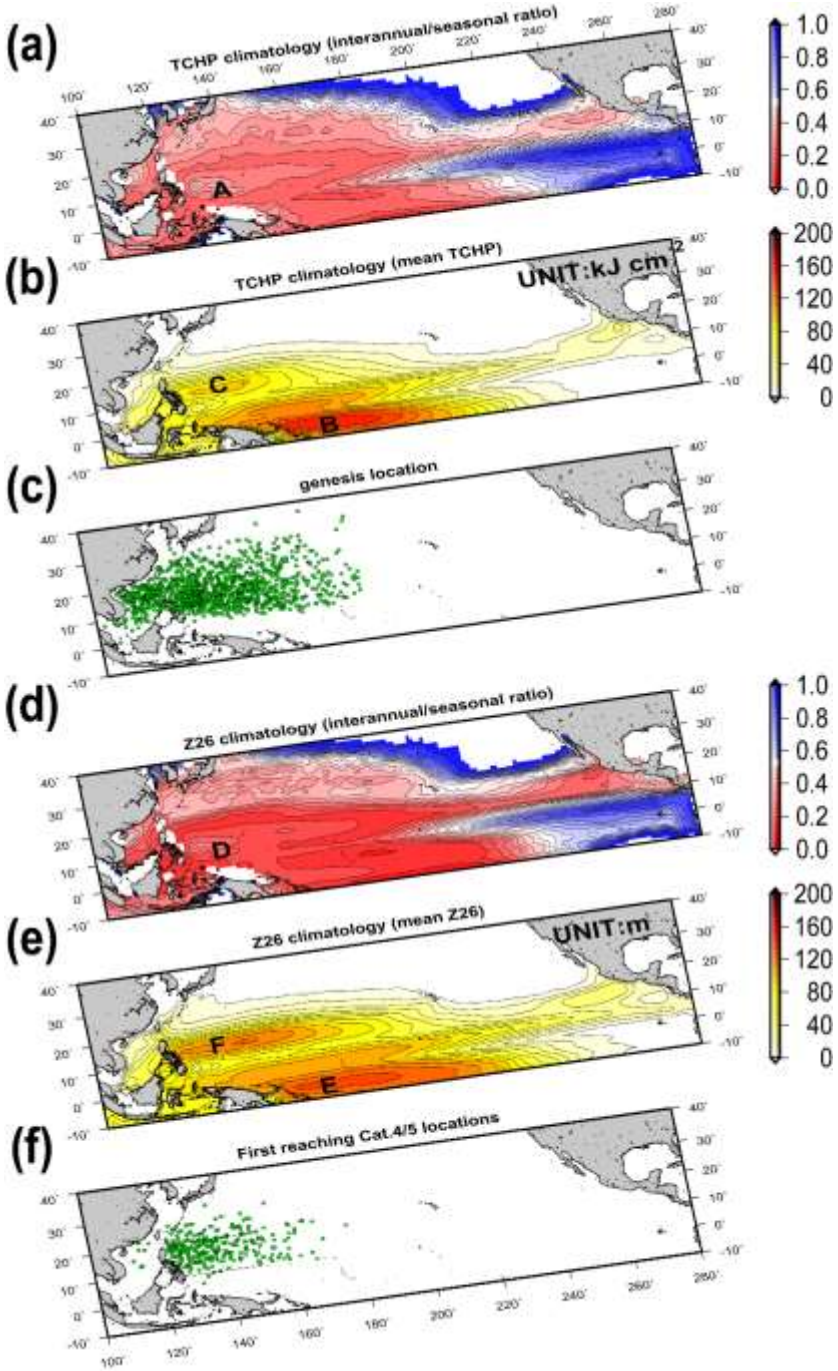

Figure 18: Spatial distributions of (a) the ratio of root mean square of TCHP anomaly deviated from mean TCHP for 44 years to that of the anomaly deviated from annual mean TCHP for 44 years, (b) TCHP averaged from 1961 to 2004, (c) genesis locations from JTWC best-track data, (d) as in panel a except for Z26 and (e) as in panel b except for Z26, (f) as in panel c except for the locations of TCs first reaching an intensity corresponding to cat-4.Subscripts A-F shows high ratio of TCHP (A), high TCHPs (B, C), high ratio of Z26 (D) and high Z26s (E,F). (From Wada *et al.*, 2012).

In the Arabian Sea, beginning in May, a cyclonically rotating atmospheric vortex forms with similar characteristics to the TC in the Atlantic Ocean and the Gulf of Mexico basins (Rao 1984). This low-pressure center with cyclonically-rotating winds moves towards the northwest due to the migration of the InterTropical Convergence Zone (ITCZ) (Findlater 1969). The timing of this northward movement of the ITCZ is modulated by the Madden Julian Oscillation causing a few week lag in Southwest Monsoon onset. A low-level forms (e.g., Findlater Jet) due to the convergence of the ITCZ and the northerlies over the northern portion of the Arabian Sea. In May 2003, Ali *et al.* (2007) found that this onset atmospheric vortex had characteristics similar to a TC (Fig. 19). The maximum intensity (Cat-4) of the TC occurred over an oceanic regime where the SHA exceeded 20 cm (deeper OML) where the corresponding SST exceeded 30.5^{o}C. The SHA field associated with this WCR is less compared to those in the GOM where SHA are 40 to 50 cm in surface deflection relative to mean sea surface level (Leben 2005).

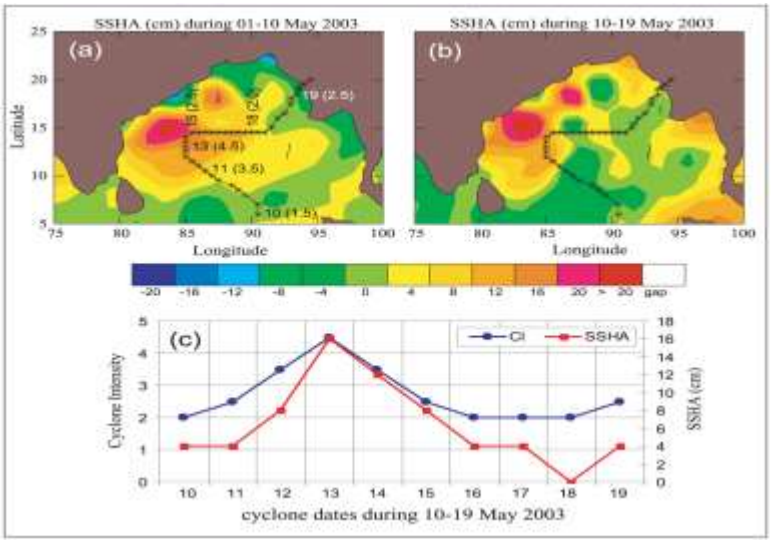

Figure 19: Composite topography of altimetry-derived SSHA (cm) from a) 1 - 10 May and b) 10-19 May 2003 relative to the track and c) along-track time series of the SSHA and TC index (CI) for the Bay of Bengal TC (from Ali *et al.* 2007).

Cyclone Nargis (2008) was a rare eastward moving TC that suddenly intensified from a relatively weak storm (cat-1) to an intense category-4 storm within 24 hrs that caused more than an hundred thousand deaths in Burma (Lin *et al.* 2009b). Based on a combination of satellite altimetry data, recently-available *in situ* Argo floats data, and numerical modelling, the abnormally thick sub-surface ocean warm layer (large OHC) precluded active entrainment of cooler, deeper thermocline water as found elsewhere. The ocean's negative feedback to intensification was reduced (more enthalpy flux).

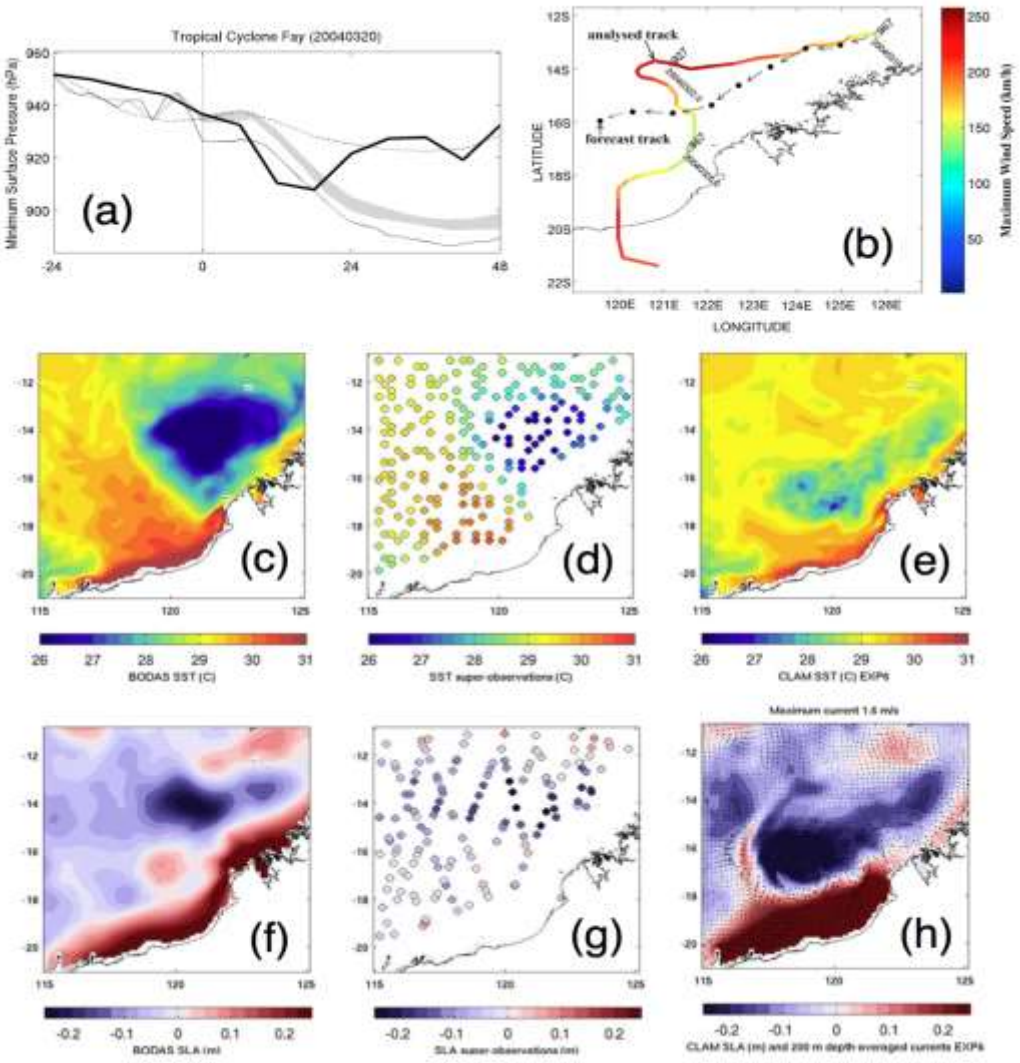

Figure 20: Observation, analysis and prediction of the ocean response to tropical cyclone Fay at 24 March 2004 off the northwest shelf of Australia illustrating sensitivity of track forecast in coupled model. (a) Comparison of analysis (heavy solid-line), operational forecast (dashed-line), uncoupled forecast (thin solid-line) and ensemble of coupled forecasts (gray envelope) for minimum surface pressure. (b) Forecasted and analyzed track. Post storm (c) BLUElink Ocean Data Assimilation system (BODAS) SST. (d) SST super-observations from the AMSR-E microwave sensor and (e) simulated SST from CLAM. Figures f-h as per c-e and illustrate corresponding sea-level anomalies and depth-averaged currents up to maximum 200-m depth. (Adapted from Sandery *et al*. 2010).

In the south Pacific Ocean, the Australian region experiences an average of 13 TCs per year and storms exhibit highly individual behaviours with erratic tracks (Dare and Davidson 2004). The ocean in this region is characterized by large environmental differences where oceanic data assimilation techniques for ocean modelling are clearly needed (Oke *et al*. 2005; Brassington *et al*. 2007). Large mesoscale variability in upper

OHC exists in various deep ocean areas, such as in the Timor Sea where activity is influenced by the Indonesian Throughflow and the Coral Sea where variability is linked to the South Equatorial Current. Broad areas of shallow continental shelf seas also exist, such as the Gulf of Carpentaria and the North West Shelf where relatively isothermal conditions prevail. The coexistence of different oceanographic environments and the broad extent of the shelf break often leads to the presence of fronts with sharply varying OHC.

A relatively higher degree of stratification is found in the equatorial southwest Pacific compared to the Atlantic, which means that a larger amount of work may be required to break down the potential energy and mix cooler water to the surface. Most TCs encounter the mixture of oceanographic regimes at various stages of their lifetime, meaning that the oceans role is complex, varied and specific for each case. There are a significant number of cases where observations show large degrees of induced SST cooling that have led to a significant change in storm intensity. One such case is TC Fay that occurred off the north-west shelf region in March 2004. This case is an example that illustrates the sensitivity of the ocean response and TC intensity to forecasted track (Sandery *et al*. 2010). Here, the forecasted track led to the storm centre following the shelf break where no cooler subsurface water was available on the left side of the storm. The actual track veered ~50 km off the shelf break over significantly deeper waters and the storm produced a pronounced ocean cooling response that significantly modified the storm's intensity (Fig. 20). This illustrates that a skilful coupled model will be required to correctly estimate intensity change for TCs in the Australian region.

Katrina and Rita both deepened to a Cat-5 TC over a lobe-like structure along the LC's western flank (Shay 2009; Jaimes and Shay 2009). There was a one-to-one correlation between TC intensity (surface pressure decreases) and OHC values exceeding 100 kJ cm^{-2} in the LC. By contrast, SSTs of more than 30^{o}C were nearly uniformly distributed in this regime, and did not reveal the complex LC and WCR structure in the central Gulf of Mexico (Sun *et al*. 2006; Shay 2009). This OHC level is more than five times the threshold of 17 kJ cm^{-2} d^{-1} integrated over the TC scale (Leipper and Volgenau 1972). Normalized OHC values vary inversely to pressure changes (surface pressure decreases, OHC increases). Mainelli *et al.* (2008) input OHC into the SHIPS (DeMaria *et al*. 2005) and found that OHC is a better indicator of TC strength than just SST alone which is similar to when TC Opal (1995) encountered a WCR and deepened to a category-4 TC during favorable atmospheric conditions. Clearly, in the western Pacific Ocean, Indian Ocean and GOM basins, these cases are all examples of *less negative feedback* since the upper ocean cooled by less than 2^{o}C to ~28^{o}C in regimes of deep warm layers (e.g., not much of a cold wake). Thus, the depth of the 26^{o}C isotherm, usually located close to the depth of the OML, and the resultant OHC is relevant to TC intensity changes.

4.4.3.5 Evaluation of OHC

Given the availability of the satellite-derived values of SSHA (and hence OHC) from radar altimetry over the globe, it is imperative to assess these inferred values relative to *in situ* data profiles (Pun *et al*. 2007; Jaimes and Shay 2009; Shay and Brewster 2010; Meyers *et al*. 2014). To illustrate the validity of this OHC approach from altimetry under non-forcing conditions, satellite-derived values were compared to *in situ* measurements from XBT

transects in the eastern Pacific Ocean basin (Shay and Brewster 2010). Five years of data along a repeated transect is used to determine OHC and compare it to the five-year average from satellite-inferred values along the same transect as well as the closest moorings (Fig. 21). There is marked agreement between the XBT, mooring and satellite-derived OHC values. Notice there are no significant differences between the two *in situ* and the remotely sensed values at 95% confidence. Over a broader spatial scale from 2000 to 2008 during

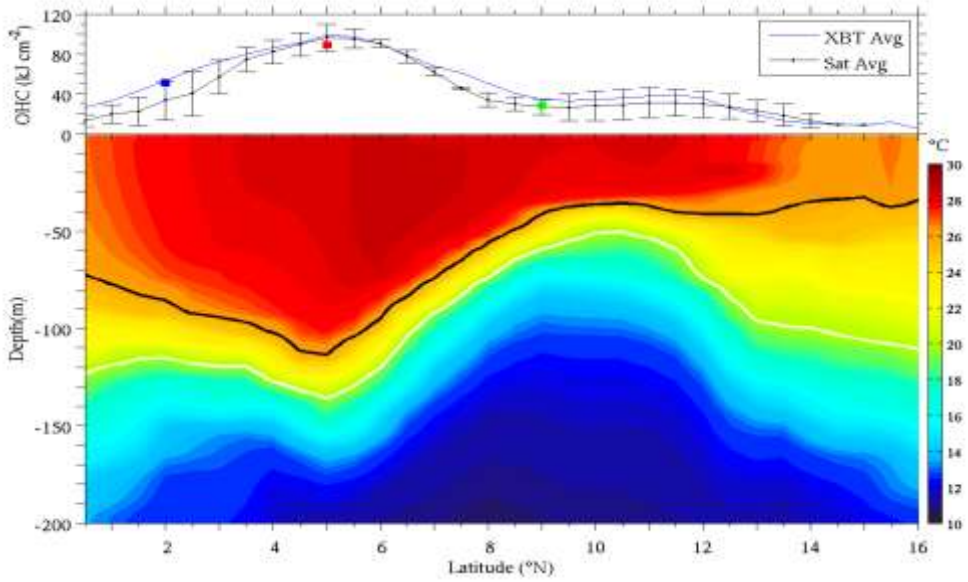

Figure 21: Averaged OHC (upper panel: kJ cm^{-2}) derived from repeat XBT transects in the eastern Pacific Ocean basin (blue line), TAO moorings at 2, 5 and 8^{o}N (140^{o}W: colored boxes) and the corresponding satellite-derived values (black line) with error bars. In the lower panel, the corresponding vertical temperature structure from XBTs where the 20^{o}C and 26^{o}C isotherm depths are depicted as white and black lines, respectively. Data were averaged from the months of July from 2000 to 2005 (From Shay and Brewster 2010).

the eastern Pacific Ocean (EPAC) basin TC season, OHC value statistics from 6,420 *in-situ* data points revealed RMS OHC differences were 13 to 20 kJ cm^{-2} or up to 15% of the maximum values with an RMS difference of 17 kJ cm^{-2} (not shown). Thus, estimating the 26^{o}C isotherm depth using satellite altimetry in a reduced gravity model (Goni *et al.* 1996) allows one to determine OHC for use with SHIPS (DeMaria *et. al.* 2005; Mainelli *et al.* 2008) that must be applied globally

An updated oceanographic climatology has been developed for empirically calculating OHC known as Systematically Merged Atlantic Regional Temperature and Salinity (SMARTS) Climatology (Meyers *et al*., 2014). SMARTS was developed by regionally blending the World Ocean Atlas 2001 (WOA) and Generalized Digital Environmental Model v.3.0 (GDEM) monthly climatologies at 1/4º resolution. This higher resolution climatology better resolved the spatial structure of the LC and eddy features in the GOM, improving upon Mainelli *et al.* (2008) approach and included the OML which improved the OHC estimations by as much as 7%. To determine the skill of SMARTS, satellite estimates were compared to over 60,000 in-situ profiles from shipborne and airborne

XBTs, long-term PIRATA moorings, and Argo drifters. As shown in Fig. 22, a direct relationship has emerged from the detailed analysis between satellite-derived and *in-situ* measurements of isotherm depths and OHC. The climatology was specifically examined in the GOM, LC, Gulf Stream, and equatorial wave guide to statistically calculate spatial blending weights from WOA and GDEM for the daily high resolution product. This same approach, known as Systematically merged Pacific Ocean Regional Temperature and Salinity or SPORTS, was developed for the North Pacific Ocean basin (McCaskill and Shay 2014) using more than 267,000 thermal profiles from the Argo floats, TOGA TAO moorings, drifters and XBT transects finding similar results with very high correlations. Both SMARTS and SPORTS are part of an operational product suite at NOAA NESDIS.

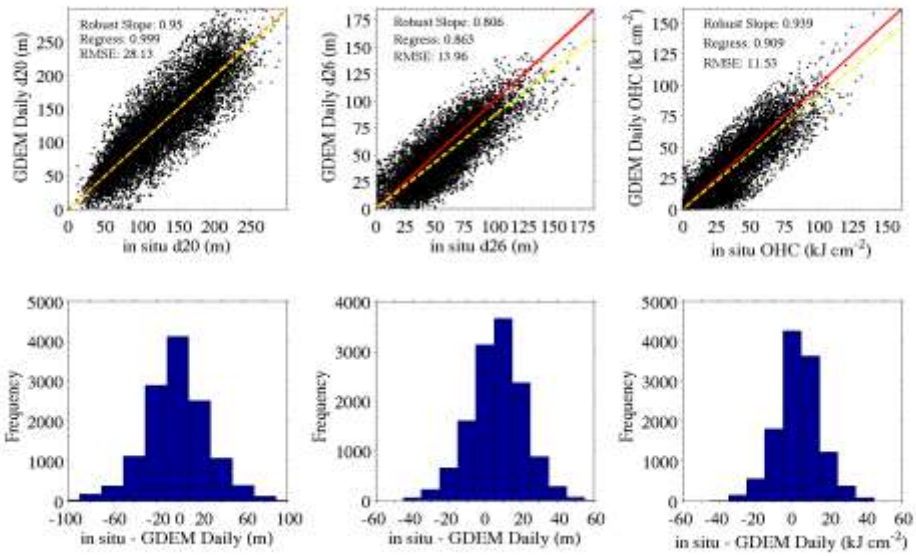

Figure 22: Scatter plots (upper panels) of *in-situ* versus satellite derived d_{20} (m), d_{26} (m) and OHC (kJ cm^{-2}) and frequency distribution of in-situ and satellite inferred differences (lower panels) from temperature profiles sensed by ARGO floats in the Atlantic Ocean basin using SMARTS and altimetry. In the scatter plot, the red line is the slope of the perfect fit, the yellow-dashed line is the slope of the actual regression fit. Key statistics are located in the upper left side of the scatter plots (From Meyers *et al.* 2014).

In 2014, Pun *et al.* (2014) uses large amount or Argo floats and satellite altimetry SSHA to obtain regression relationship to obtain subsurface thermal profiles over the western North Pacific ocean from about 38,000 thermal profiles. The approach differs in that rather than using a layered model (Shay *et al.* 2000; Shay and Brewster 2010; Meyers *et al.*, 2014), this new approach may now obtain 26 isothermal layers (D4 to D29) to improve the vertical resolution of the subsurface profile in capturing the subsurface profile shape. This improvement can leads to better initialization to coupled modeling and to obtain improved OHC estimate, since subsurface profiles can be characterized by 26 isothermal layers over the western North Pacific now (Fig. 23). This regression based approach is based on about 38,000 profiles over ten years over a spatial scale of 24.2 million km^2 since the differences are based on the depth of the 20°C isotherm from climatology and nearby ARGO profiles. McCaskill and Shay (2014) used over 267,000 thermal profiles in evaluating the SPORTS climatology which is based on daily WOA and GDEM climatologies. The inclusion of the

OML is now inferred in the 2.5 layer model and reduces the uncertainties by as much as 7% in estimating OHC from SMARTS and SPORTS (Meyers *et al*. 2014).

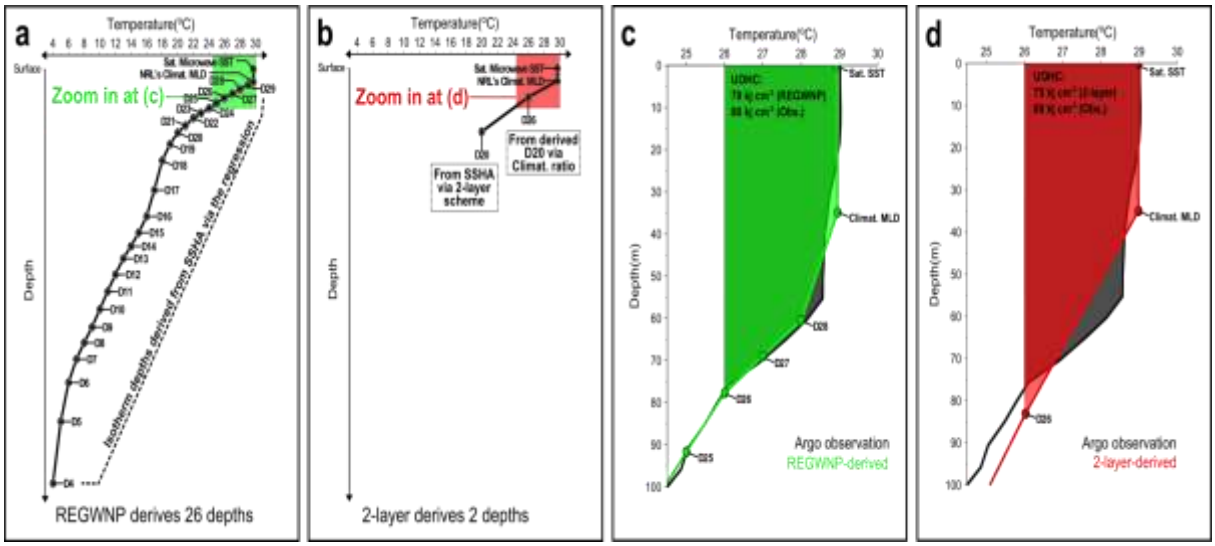

Figure 23: Schematic of (a) REGWNP-derived profile and (b) TLM-derived profile. (c) Zoom-in area of (a) compares the profiles from the REGWNP (green) and Argo (black). (d) Zoom-in area of (b) compares the profiles from the TLM (red) and Argo (black). Shaded areas in (c) and (d) indicate the upper ocean OHC, their values are also shown in the Western Pacific MDR domain-averaged D26 (in red, left axis) and OHC (in blue, right axis) has increased by 12% in the past 2 decades (After Pun *et al*. 2014).

4.4.4 Air-Sea Interface:

Given limited observations across the air-sea interface during TCs, the understanding has not progressed nearly enough to significantly improve the parameterization of momentum and energy transfers between the two fluids. The relationships of the transfer processes of small-scale roughness (Charnock 1955) and surface-layer stability (Monin-Obukhov similarity theory) are understood under low- to moderate-wind conditions (Large and Pond 1981), but additional phenomena not typically observed such as the sea state maturity (Donelan 1990; Moon *et al.* 2004a,b) and sea spray (Wang *et al.* 2001; Andreas 2010) have been shown to modulate the heat and momentum exchange. These effects under TC winds have been primarily studied in controlled laboratory experiments (Donelan *et al.* 2004). In a TC environment, both young and mature waves are present and impact air-sea fluxes and OML and atmospheric boundary layer processes.

Intensity is maintained in part by the balance between the heat gained by the atmospheric boundary layer and the energy lost due to friction. Emanuel (l986) proposed a theory requiring this relative balance to be a primary modulator of maximum potential intensity (MPI). Based on this view, it is assumed that under certain conditions there should be a level of mutual dependence of the air-sea transfer processes of heat and momentum as suggested in idealized model simulations (Emanuel 1995; Braun and Tao 2000). This has

led to the conclusion that intensity is sensitive to the ratio of enthalpy to drag coefficient ($c_k\ c_d^{-1}$), which lies within a limited range. However, most TCs do not reach their MPI (DeMaria *et al*. 2005). When the SST in the MPI calculation is replaced with a mean mixed layer ocean temperature, the revised MPI provides an improved maximum intensity estimation with the observed 1998-2011 western North Pacific TCs (Lin *et al.* 2013).

4.4.4.1 Surface Wave Field

It has been known that the NOAA's WAVEWATCH III (WW3) wave model tends to overestimate the significant wave height (Hs) under extreme hurricanes (Tolman *et al.* 2005; Chao *et al.* 2005). Moon *et al.* (2008) suggested that one of the reasons for the overestimation of Hs is due to overestimation of the drag coefficient in high wind conditions. Fan *et al.* (2009 a,b) have implemented the Moon *et al*. (2007) drag coefficient formulation into WW3 and introduced the effect of wave-current interaction. The wave model results were compared with field observations of the surface wave spectra from a scanning radar altimeter (SRA) (Wright *et al*. 2001), National Data Buoy Center (NDBC) data and satellite altimeter measurements during TC Ivan (2004) (Fig. 24). The results suggest that WW3 with the original drag coefficient parameterization tends to overestimate the significant wave height and the dominant wave length, and it produces a wave spectrum that is higher in wave energy and narrower in directional spreading. Using the Moon *et al.* (2007) drag parameterization with wave-current interaction in WW3, the simulations suggest an improved forecast of Hs, but it underestimates the dominant wave length (DWL).

Closer to the coast, Wang *et al.* (2005) documented the wave response to Ivan over the NRL SEED moorings (Fig. 25). Wave heights increased with peak values when the radial distance between the mooring and storm center was ~75 km (Fig. 20c). Hs reached maximum values of 16 m to 18 m on inshore moorings and were larger than those detected at the NDBC buoy (15.9 m). The maximum wave height was recorded to be 27.7 m at mooring 3, and wave height variations were consistent with the radial variations in the surface wind of Ivan. At Rmax, the model predicted a maximum wave height of ~21 m. Previous studies have suggested in a TC wave field that the maximum wave height approaches 1.9 x Hs, which would be consistent with these measurements. However, the moored measurements sampled only a small part of the domain influenced by Ivan's broad wind field with large changes in the bottom topography. A larger area of Hs was instead sampled south of the SEED moorings in the middle of the GOM by the airborne Scanning Radar Altimeter (SRA) along an "alpha flight pattern" by the NOAA's Hurricane Research Division (HRD) where the Hs observed by the SRA is between 6 – 12 m. A bimodal swell with wavelength of 250–300 m is seen propagating toward the northwest (Chen *et al.* 2014).

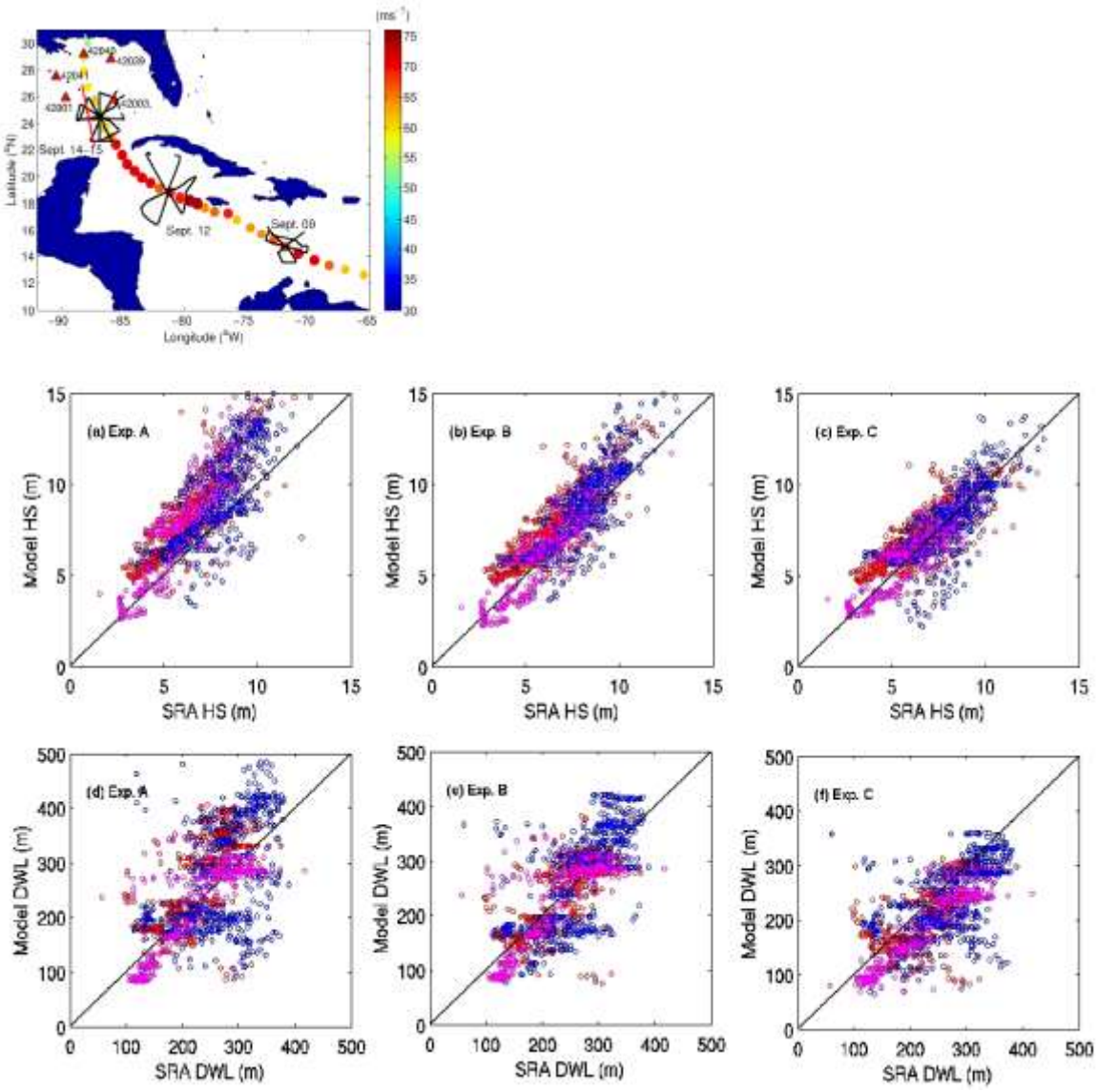

Figure 24: Tracks (black lines) of NOAA WP-3D (upper left panel) aircraft relative to TC Ivan's track and intensity (color bar) where directional wave measurements were acquired from the SRA on 9, 12 and 14-15 Sept. 2004. The red line to the left of the Ivan's track, overlaping with the 14-15 Sept measurements, represents satellite tracks of Envisat-1 and ERS-2. Red triangles in the Gulf of Mexico depict NDBC buoy locations along Hurricane Ivan track. In the bottom panels, comparisons between WW3 H_s dominant wave length (DWL) vs. SRA measurements for (a,d) Exp. A with original WW3 drag coefficient, (b,e) Exp. B with Moon *et al*. (2007) drag coefficient, and (c,f) Exp. C with the new drag coefficient and the oceanic current effect. Magenta, red, and blue circles correspond to differing SRA measurement periods (Adopted from Fan *et al.* 2009).

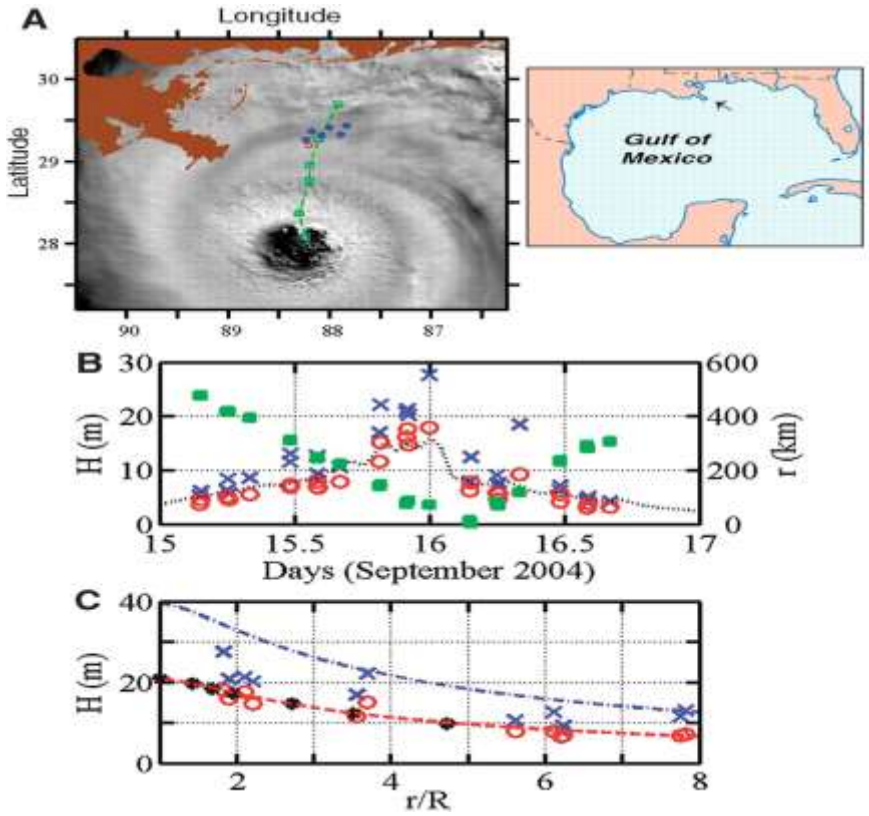

Figure 25: a) TC Ivan image at 1850 UTC 15 Sept 2004 with the green line representing the track of Ivan at 3-h intervals moving over the SEED moorings (blue). Panel b) represents the time evolution of Hs (circle) and Hmax (cross) at differing distances. Hs is from NDBC buoy 42040 (dotted curve) and its radial distance to Ivan's center is shown by the green squares. Panel c) represents Hs and Hmax as a function of normalized distance from the center compared to the exponential distance: digitized values of a segment 15^{o} clockwise (CW) from the forward direction of a numerically simulated wave field (black asterisks). Blue curve depicts the line of Hmax = 1.9Hs where circles and crosses are as in panel b) (from Wang *et al.* 2005).

4.4.4.2 Surface Winds

Surface winds in hurricanes have been estimated remotely using the Stepped-Frequency Microwave Radiometer (SFMR) from aircraft (Uhlhorn *et al.* 2007). With six frequencies, the SFMR measures radiative emissions, expressed in terms of brightness temperatures (T_b), from the ocean and the atmosphere. The percentage of foam coverage on the sea surface is known to increase monotonically with wind speed. At microwave frequencies, foam acts as a blackbody emitter. As foam increases, the ocean emits microwave energy more readily, and assuming a constant SST, the T_b increases. Given an accurate physical model that relates ocean surface wind speed and rain-rate to measurements of T_b at each frequency, a set of equations are inverted to estimate surface winds. Based on measurements during the 2005 Atlantic hurricane season, Uhlhorn *et al.* (2007) developed

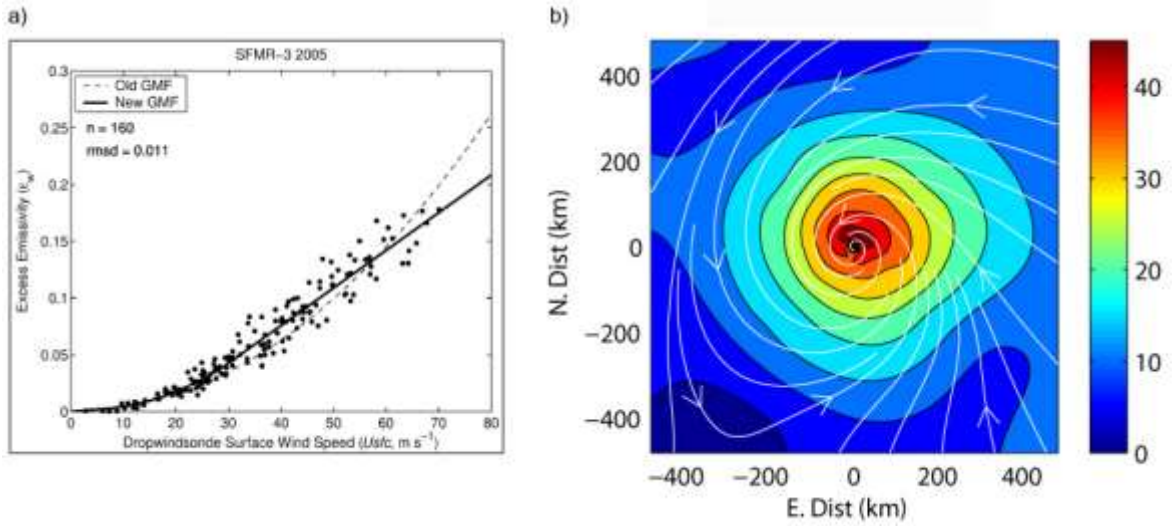

Figure 26: a) Excess emissivity from SFMR compared to 10-m surface winds measured from GPS dropsondes. The total number of samples is 160 and the RMS difference between the SFMR model function was 0.011 (left panel) and b) example of an HWIND wind field (Powell and Houston 1996) and streamlines relative to the TC center (0,0) when SFMR data are included into the analysis from TC Frances (2004) where the color bar is in m s^{-1} (from Uhlhorn *et al.* 2007).

a new emissivity and wind speed model function based on comparisons with direct measurements of surface winds in hurricanes by GPS dropwindsondes (Fig. 26). This function eliminates a previously-documented high bias in moderate SFMR-measured wind speeds (10 to 50 m s^{-1}), and additionally corrects an extreme wind speed (>60 m s^{-1}) systematic underestimate in the past cases. The model function behaves differently below and above the hurricane wind speed threshold (32 m s^{-1}), which may have implications for air-sea momentum and kinetic energy exchange.

4.4.4.3 Surface Drag Coefficient

Knowledge of the heat and moisture fluxes across the interface and into the atmospheric boundary layer are critical elements (Emanuel 1995). Momentum transfer between the two fluids is characterized by the variations of wind with height and a surface drag coefficient ($C_{d)}$ that is a function of wind speed and surface roughness. For more than a decade, GPS sondes (Hock and Franklin 1999) have been deployed from aircraft to measure Lagrangian wind profiles in the TC boundary layer. By analyzing these profiles, Powell *et al.* (2003) found a logarithmic variation of mean wind speed in the lowest 200 m, a maximum speed at 500 m, and a gradual weakening with height to 3 km. From these estimates, the surface stress, roughness length, and neutral stability drag coefficient determined by the profile method suggest a leveling of the surface momentum flux as winds increase above hurricane-force and a slight decrease of the drag coefficient with increasing winds.

Donelan *et al.* (2004) described a series of wind-wave tank experiments that included stress measurements from hot-film anemometry and digital particle image velocimetry, and laser/line scan cameras for measuring the water surface elevation. Measurements of the drag coefficient from this laboratory experiment referenced to the 10-m wind speed. Wind speed was measured at 30-cm height in the tank and extrapolated to the 10-m using the logarithmic dependence on height. Wind speeds were verified between crest height and 30 cm for all but the two highest wind speeds. The saturation level for c_d is ~0.0025, corresponding to a roughness length of 3.35 mm from the laboratory results. Powell *et al.* (2003) found a "saturation" of the drag coefficient at 0.0026 at about 35 m s^{-1} that decreased at higher wind speeds using wind profiles normalized by a mean boundary layer wind. Shay and Jacob (2006) found a "saturation" wind speed at 30 m s^{-1} of 0.0034 derived by equating internal wave ocean fluxes to the surface winds at 10-m level. Note it was assumed that all of the wind drives a current and no separation was attempted to partition the energy between current and wave fields. Beyond 30 m s^{-1}, the c_d began to level off at surface wind speeds up to 38 m s^{-1} observed in TC Gilbert. The implication here is that ocean current profilers deployed in TC can be used to trace the momentum flux, and the c_d behavior.

The momentum flux was also estimated using the current profiles recorded in water depths of less than 100 m during TC Ivan (Teague *et al.* 2007), and discussed in terms of the neutral drag coefficient (Jarosz *et al.* 2007). The eye of Ivan generated strongly forced and relaxation stage responses to the surface wind field (Wang *et al.* 2005; Teague *et al.* 2006, 2007). Over the shelf, the response consisted of a barotropic component, and a much weaker baroclinic response. Scale analysis of recorded current velocity showed that this forced response was described by the linearized, depth-integrated along-shelf horizontal momentum balance with bottom friction. The drag coefficient was estimated based on these observed depth-averaged currents at an ADCP mooring for wind speeds between 20 and 48 m s^{-1}. In this case, surface drag increased to a peak value of 0.0026 at 32 m s^{-1} before decreasing. This inflection point is coincident with above results. Differences may also be attributed to uncertainties in the wind measurements and the use of simplified ocean dynamics.

Sanford *et al.* (2007) estimated the volume transport per unit of width based on velocity profiles in hurricane Frances using a saturated surface drag coefficient of Powell *et al.* (2003) and Large and Pond (1981) formulations. Numerical simulations from the PWP mixing model embedded in the 3-D ocean model (Price *et al.* 1994) indicated consistent results for the volume transport and SST cooling values at two of the three floats to the right of the storm track. Along the track, however, differences differed by about 15 to 20%. More recently, Sanford *et al.* (2011) used EM-APEX velocity profiles from Hurricane Frances to estimate local terms of the upper-ocean momentum balance during the period of strongest forcing to back out an estimate of C_d. Over a range of wind speeds from about 27-47 m s^{-1}, the estimated value was 1.5×10^{-3}, substantially smaller than previous estimates of $\geq 2 \times 10^{-3}$ obtained from the atmospheric side of the air-sea interface. This discrepancy may result in part from the transfer of some of the surface momentum flux to the non-stationary wave field beneath the storm. Errors in surface momentum estimates provided to the ocean model produce substantial errors in SST cooling rate. This

analysis highlights the importance of upper-ocean velocity measurements and momentum balance analysis to understand this phenomenon and to evaluate ocean model performance.

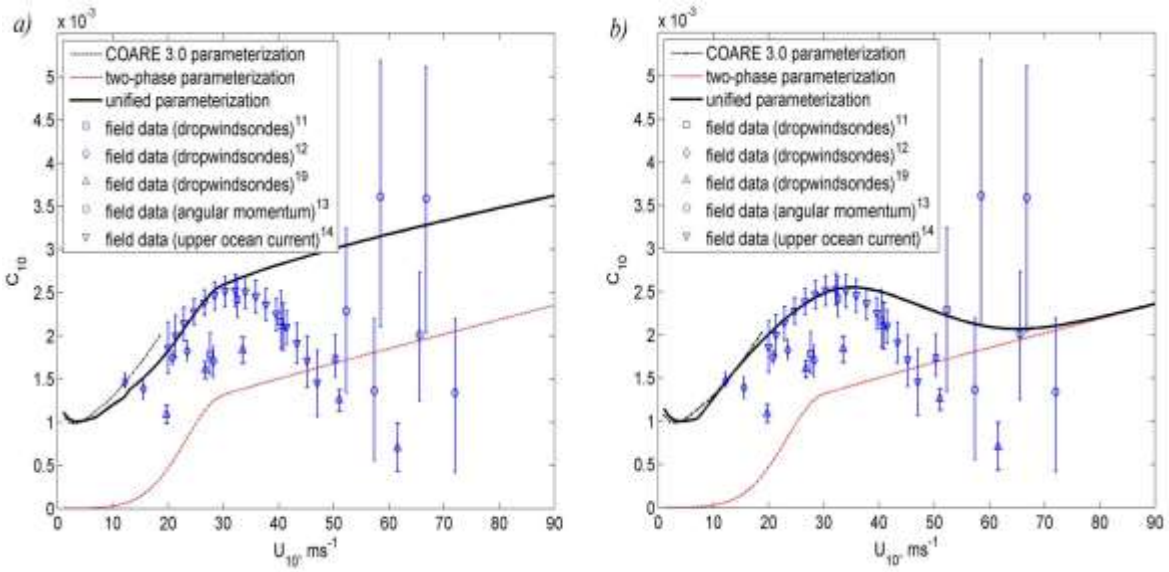

Figure 27: Comparison of the unified air-sea drag coefficient parameterization calculated with the surface stress method (a) and the surface roughness method (b). The COARE 3.0 parameterization, two-phase parameterization (lower bound on drag coefficient), and available data from field experiments are shown for comparison. We have included only the available field observations that report confidence intervals. The surface stress method and the surface roughness method are different approaches for unifying two-phase, wave-form, and viscous stresses (see Methods). The COARE 3.0 parameterization has been used for verification of the unified parameterizations in the range of wind speeds from 1 to 19 m s^{-1} (from Soloviev *et al*. 2014).

Soloviev *et al*. (2014) reported new parameterization of surface drag coefficient. Through a laboratory experiment and numerical LES, they were able to confirm the microstructural processes of the air-sea interface under the hurricane force environment similar to Kelvin-Helmholtz (KH) shear instability between two fluids. They were able to simulate that growing KH waves at high winds break the tension of the air-sea interface, eventually producing large droplets ("spume"), which is confirmed by the laboratory experiment. Based on the results, they derived a new parameterization by employing the wave-form and the two-phase parameterization model, whose value increases at weak winds and becomes variable at strong winds (Fig. 27). They reported that a local peak of C_k/C_d around 60 m s^{-1} of the new parameterization, where enthalpy exchange coefficient C_k is constant, accounts for rapid intensification that is observed often in winds between 40 and 60 m s^{-1} (Fig. 28).

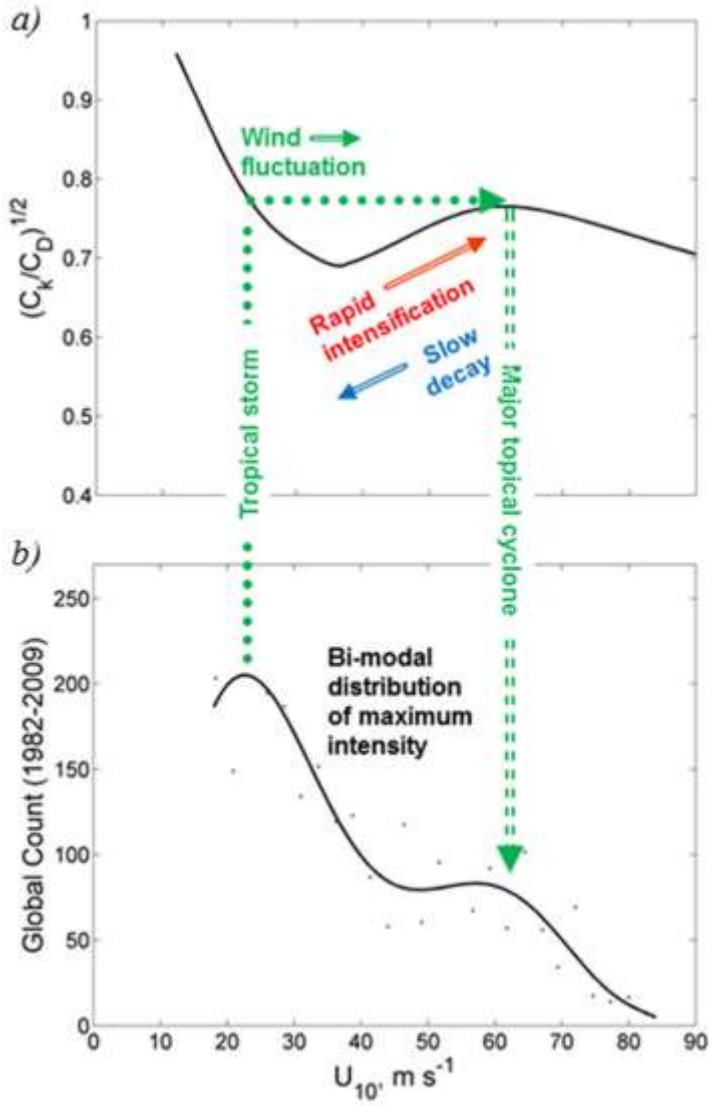

Figure 28: A mechanism of rapid storm intensification and the bimodal distribution of lifetime maximum tropical cyclone intensity. The shape of C_k/C_d dependence on wind speed containing a secondary maximum around 60 m s^{-1} (a) may be a factor in rapid intensification of some storms to major tropical cyclones and may explain the observed bimodal distribution of lifetime maximum intensity of tropical cyclones (b). Drag coefficient C_d is shown in Fig. 27b; while enthalpy coefficient C_k is interpolated from laboratory data for winds below 40 m s^{-1} and extended with a constant value C_k=1.2 x 10^{-3} for winds above 40 m s^{-1}, which is consistent with the available field data. Continuous line in (b) is a 7th order polynomial fit to the global best-track tropical cyclone data on maximum intensity for 1982–2009 (dots) (Figure from Soloviev *et al*. 2014).

4.4.4.4 Wind-Wave Coupling

The momentum flux is parameterized with a non-dimensional surface roughness (or Charnock's equation, $z_{ch} = z_0 g / u_*^2$, where z_0 is the roughness length, u_* is the surface friction velocity and g is the gravitational acceleration) and the stability correction (not shown) is based on the Monin-Obukhov similarity theory, regardless of the wind speed or the sea state in the GFDL model. Moon *et al.* (2004) investigated the Charnock coefficient under TC conditions using a coupled wind-wave (CWW) model (Fig. 29). In the CWW model, the surface wave directional frequency spectrum near the spectral peak is calculated using the WAVEWATCH III (Tolman 2002) model and the high frequency part of the spectrum was parameterized using the theoretical model of Hara and Belcher (2004). The wave spectrum is then introduced to the wave boundary layer model of Hara and Belcher

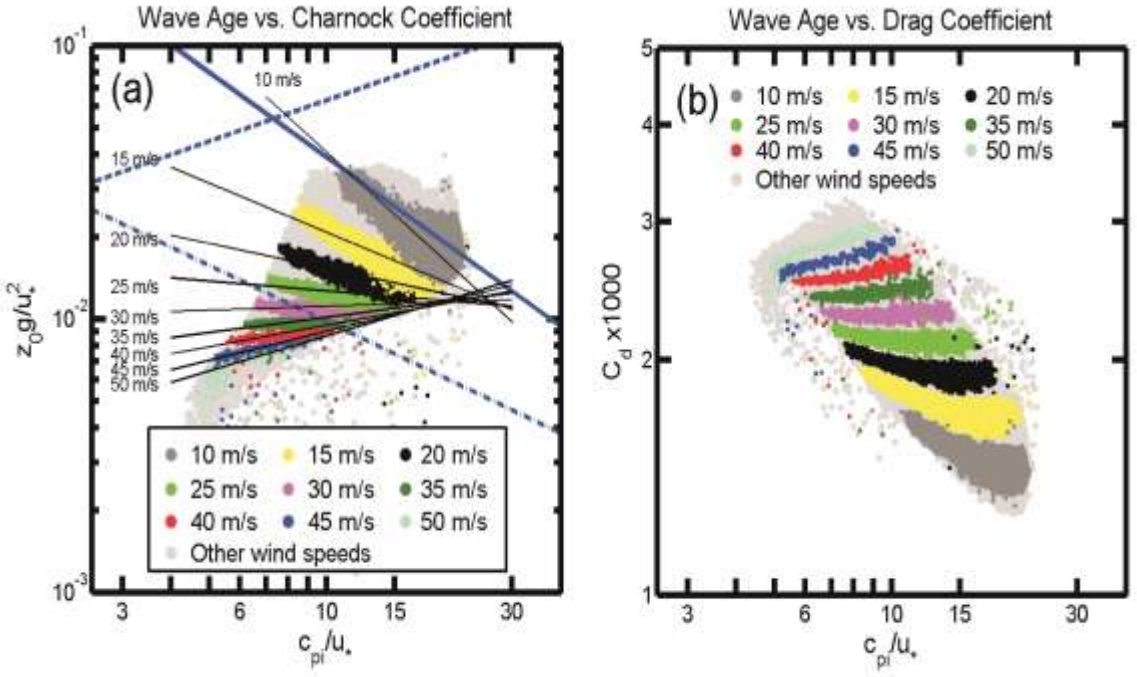

Figure 29: Scatterplots of the a) Charnock Coefficient (z_{ch}) and b) drag coefficients (c_d) as a function of the wave age (cp/ u_*) for several TCs in the Atlantic Ocean. Differing colors represent 5-m s^{-1} intervals for surface winds for z_{ch} and $c_{d.}$ are the best fits for each wind speed group. In panel a, blue solid line and dash-dot represent empirical estimates for ocean and laboratory experiments (Donelan 1990). Dotted line is the formula of Toba et al. (1990) (Figure from Moon *et al.* 2004a).

(2004) to estimate the Charnock coefficient at differing wave evolution stages. The regression lines between the wave age and the Charnock coefficient have a negative slope at low wind speeds but have a positive slope at higher wind speeds. For example, in Figure 29a, this change in slope occurs between 25 and 35 m s^{-1}. This behavior of the Charnock coefficient provides one explanation why c_d under a TC, where seas tend to be "young," is reduced in high wind speeds as the wave field is not fully developed. Consistent with this change in the Charnock coefficient, c_d levels off at high wind speeds and begins to decrease at ~35 m s^{-1}. The result also is in accord with these other studies in that the drag coefficient levels off between surface winds of 28 to 33 m s^{-1} and begins to decrease with wind speeds (Powell *et al*. 2003; Donelan *et al.* 2004). Notwithstanding, perhaps the most important finding of the Moon *et al.* (2004b) study is that a hurricane model must have a surface wave model to gain a more accurate prediction of surface enthalpy fluxes under the high-wind conditions (Wada *et al*. 2013b).

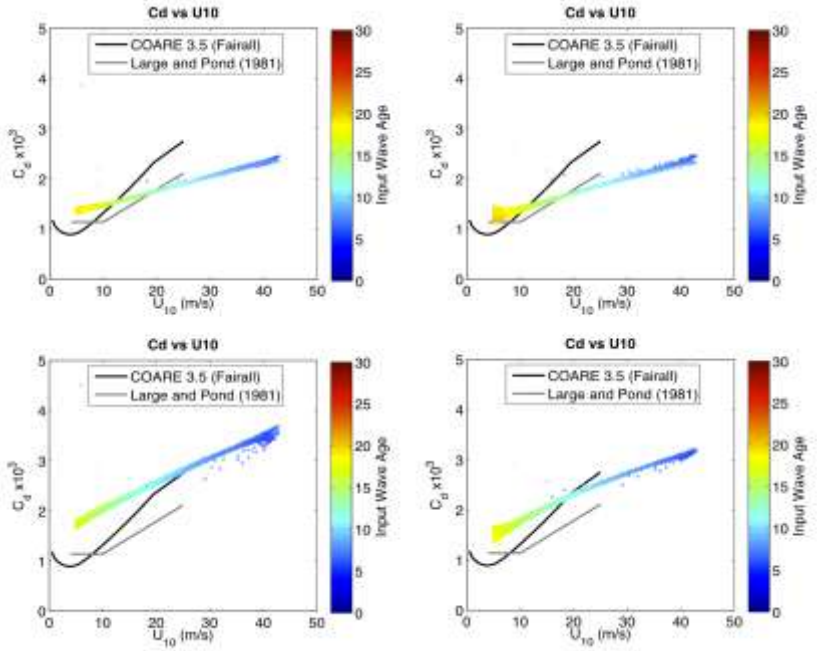

Figure 30: Drag coefficient ($\times 10^3$) vs wind speed for a 5 m s^{-1} translating tropical cyclone. The left column is calculated using the Reichl *et al.* (2014) method, while the right column is calculated using the Donelan *et al.* (2004) method. The saturation level is set to 0.006 (top), and 0.012 (bottom) (From Reichl *et al.* 2014).

Reichl *et al.* (2014) investigated the impact of the surface wave field (sea state) on the wind stress over the ocean with fetch-dependent seas under idealized tropical cyclone winds. Two different approaches were employed to calculate the wind stress and the mean wind profile. The results suggest (Fig. 30) that the drag coefficient magnitude is very sensitive to the spectral tail level but is not as sensitive to the drag coefficient calculation methods. The drag coefficients at 40 m s^{-1} may vary from 1×10^{-3} to 4×10^{-3} depending on the saturation level. The results also indicate enhanced sea state dependence of the drag coefficient for a fast moving tropical cyclone than for a slow moving storm. Another potentially important limiting factor in TC intensification is the kinetic energy loss due to surface friction. The viscous dissipation of the kinetic energy can be a significant heat source for TCs as this part of the kinetic energy is ultimately dissipated on molecular scales into heat (Bister and Emanuel 1998). Using the Navy's operational forecast model - COAMPS® to improve TC intensity and structure forecasts, Jin *et al.* (2007) showed that the inclusion of dissipative heating improves surface maximum wind forecasts of Hurricane Isabel by 10-20% at a 15-km horizontal resolution and even more so (up to 29%) at 5-km resolution. This study is distinct from previous investigations of dissipative heating (e.g. Zhang and Altshuler 1999) in that the kinetic energy dissipation both at the surface and in the internal atmosphere is considered using the dissipation equation of turbulent kinetic energy (TKE) to ensure energy conservation. The averaged profiles of the wind speed in the boundary layer indicate that the TKE-only run (only the dissipative heating in the internal atmosphere considered) results in a small impact on wind speed, but when the dissipative heating from the surface friction and internal dissipation work together the storm obtained significantly stronger winds than when either process at work alone (surface friction only or TKE only), suggesting highly nonlinear interaction between the two dissipative heating processes. The dissipative heating produced about 12 m s^{-1} stronger azimuthally averaged winds in the eyewall region than the run without and also warmed the air near the surface by nearly 1^{o}K near the eyewall, resulting in negative

COAMPS® is a registered trademark of the Naval Research Laboratory.

(albeit small) sensible heat flux in that region. The azimuthally averaged vertical motion in the run without the dissipative heating was only about 0.5 m s^{-1} over a section of 60 km along the radius.

Wada et al. (2013a) examined the surface roughness-length scheme that directly affects the simulated sea-level pressure, air temperature, and sea-air CO_2 flux at the location of a buoy during the passage of Choi-wan (2009) and has an effect on the variations in sea surface salinity (SSS) after the passage of the typhoon and oceanic surface uptake of carbon dioxide (pCO_2) during and after the passage of the typhoon. The change of surface roughness-length scheme also affects the surface wind asymmetry but has little effect on sea-surface cooling induced by Choi-wan. Strong surface friction plays a role in intensification of Choi-wan, while it enables weakening of the typhoon during the mature phase. The effect of a change in surface roughness may differ on oceanic surface pCO_2 depending on the phase of the typhoon.

4.4.4.5 Enthalpy Fluxes

Direct turbulent flux measurements were carried out in the hurricane boundary layers using a research aircraft instrumented with fast-response turbulence sensors (Black *et al*. 2007). As shown in Fig. 31, the wind speed range for momentum and enthalpy fluxes and exchange coefficients has been extended by over 50% compared to that in previous studies. The drag coefficient (C_d) increase linearly with 10 m wind speed up to 22 m s^{-1} then level off at higher wind speed (French *et al.* 2007). The Dalton number (C_E) is nearly constant with 10 m wind speed up to 30 m s^{-1} (Drennan *et al.* 2007). Combining the sensible and latent heat flux measurements, Zhang (2007) derived the enthalpy flux and the exchange coefficient for enthalpy transfer (c_k) showing that there is no evidence of an increase of c_k with wind speed, in good agreement with the Humidity Exchange over the Sea (HEXOS) result (DeCosmo *et al.* 1996) and recent wave tank experiments (Jeong *et al.* 2012, Haus *et al.* 2010). The ratio of C_k/C_d versus wind speed for the flux runs with both momentum and enthalpy flux measurements. The average is 0.63 well below the 0.75 threshold for TC development suggested by Emanuel (1995).

Estimates of enthalpy fluxes during TCs Isidore and Lili were sensitive to the storm translation speed. In Isidore, peak enthalpy flux ~1.7 kW m^{-2} was in the right-rear quadrant of the storm due to the high SSTs (~30^{o}C) as there was a negligible decrease from pre-storm SST conditions, especially over the warm LC where ocean cooling was minimal (Shay and Uhlhorn 2008). Although the maximum momentum flux (7 Pa) is in the right-front quadrant, TC Isidore's wind stress field was symmetric as it moved at only 4 m s^{-1}. Estimated maximum surface enthalpy fluxes in Lili were about 1.4 kW m^{-2} due in part to the marked asymmetry associated with the faster storm translation speed (7 m s^{-1}) and SSTs reduced by about 1^{o}C. This result highlights how modest SST differences alter the surface heat fluxes in extreme winds (Cione and Uhlhorn 2003; Cione *et al.* 2013). Enthalpy fluxes were integrated along the track to obtain the cross-track (radial) distributions of net sea surface heat loss (not shown). The estimated surface heat loss in Isidore (~9 kJ cm^{-2}) is almost a factor of two larger than in Lili (~4.5 kJ cm^{-2}) due to the enhanced enthalpy fluxes, slower storm speed, and larger horizontal SST gradients along

the western side of the Yucatan Strait. To potentially improve estimates of enthalpy fluxes, a wave glider with CTD sensor and weather station has been shown to provide near-surface temperatures (e.g. SST) compared to the other measurement techniques such as AXBTs where the closest temperatures are several meters beneath the surface.

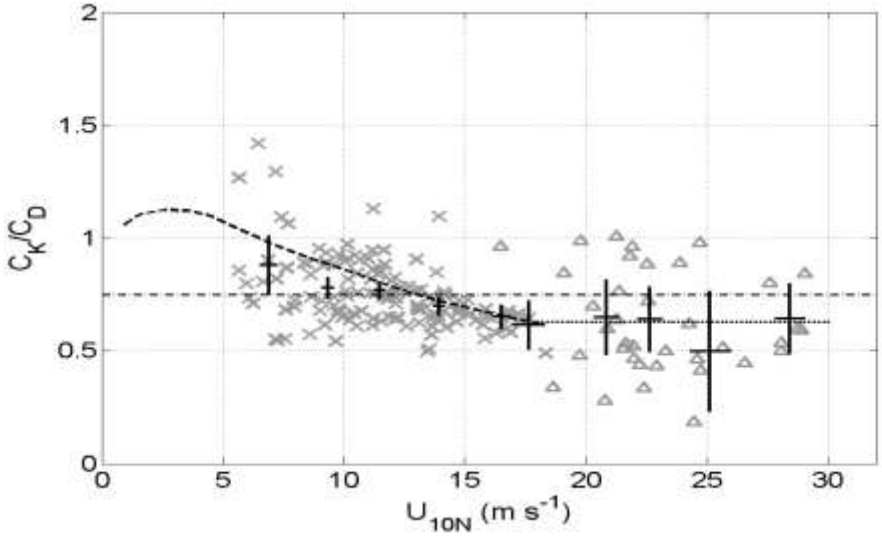

Figure 31: Ratio of $C_k C_d^{-1}$ as a function of 10-m neutral wind speed. Data from CBLAST (Δ), and HEXOS (x) are shown. Solid black lines show the mean and 95% confidence intervals of the combined HEXOS and CBLAST field data after binning average by wind speed. The dotted black line shows the mean of the CBLAST data. The ratio based on COARE 3.0 bulk flux algorithm is shown as the dashed line. The threshold value of 0.75 suggested by Emanuel is also shown as the dash-dotted line (from Zhang 2007).

4.4.4.6 Sea Spray

Recent research on sea spray effects in TCs has included fundamental theory, surface-source scaling, near-surface effects of spray on momentum and thermodynamic transfer, and sensitivity of numerical forecast models to parameterized sea spray. Soloveiv and Lukas (2010) postulated a lower limit on the drag coefficient under hurricane force winds caused by the break-up of the air–sea interface due to KH instability and formation of the two-phase transition layer consisting of sea spray and air bubbles (noted above). Rastigejev and Lin (2010) applied the Lighthill and Barenblatt approach to examine the lubricating effect of sea spray associated with it negative buoyancy effect.

Zheng *et al.* (2010, 2012) studied the effects of sea spray on tropical cyclone (TC) structure and intensity variation through numerical simulations using an advanced sea-spray parameterization from the National Oceanic and Atmospheric Administration/Earth System Research Laboratory (NOAA/ESRL), which is incorporated in the idealized Advanced Research version of the Weather Research and Forecast (WRF-ARW) model. The effect of sea spray on TC boundary-layer structure is also analyzed. The results show that there is a significant increase in TC intensity when its boundary-layer wind includes the radial and tangential winds, their structure change, and the total surface wind speed change. Diagnosis of the vorticity budget shows that an increase of convergence in TC

boundary layer enhances TC vorticity due to the dynamic effect of sea spay. The main kinematic effect of the friction velocity reduction by sea spray produces an increment of large-scale convergence in the TC boundary layer, while the radial and tangential winds significantly increase with an increment of the horizontal gradient maximum of the radial wind, resulting in a final increase in the simulated TC intensity. The surface enthalpy flux enlarges TC intensity and reduces storm structure change to some degree, which results in a secondary thermodynamic impact on TC intensification.

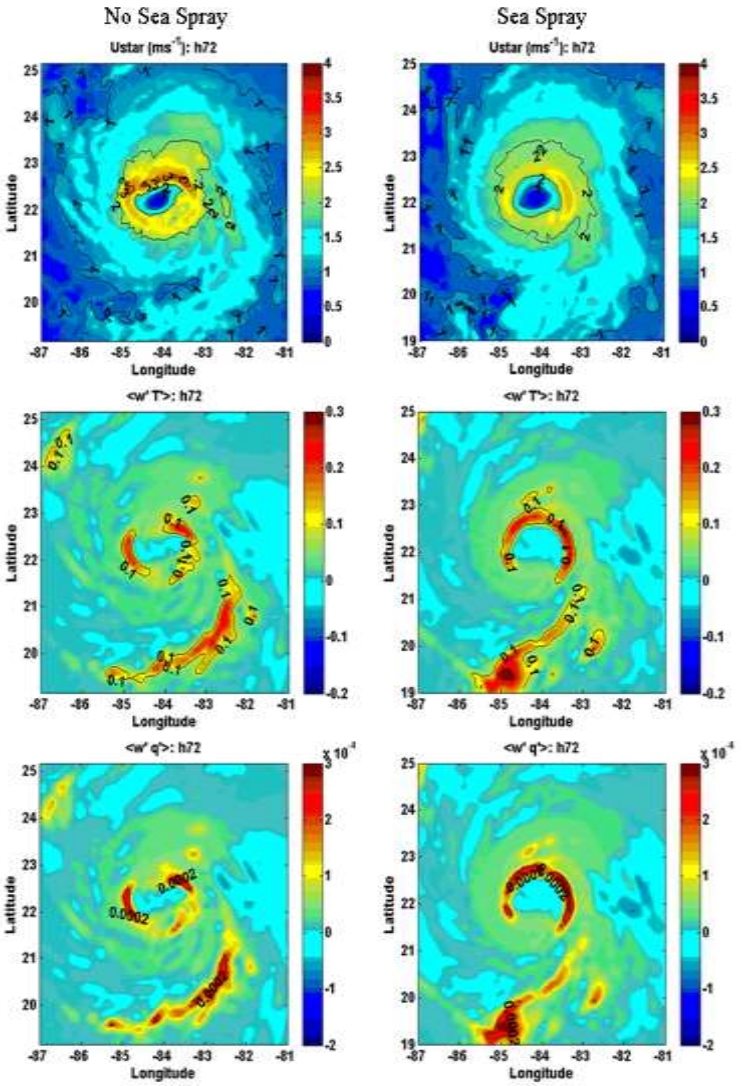

Figure 32: Maps of the friction velocity (u*, the top row, in unit of ms^{-1}), turbulent flux of temperature ($\langle w' T' \rangle$, the middle row, in unit of $Km^{-2}s^{-1}$) and turbulent flux of specific humidity ($\langle w' q' \rangle$, the bottom row, in unit of $kg/kg\ m^{-2}s^{-1}$) from two air-sea coupled GFDL model simulations initialized identically that are run with (right column) and without (left column) the sea spray scheme. These fields are defined at the lowest model level (~35 m above the surface) and valid at 72 h into the model integration. The contour intervals for u*, $\langle w' T' \rangle$ and $\langle w' q' \rangle$ are 2 m s^{-1}, 0.1 $Km^{-2}s^{-1}$ and 0.0002 $kg/kg\ m^{-2}s^{-1}$, respectively (from Bao *et al.* 2010).

Several new scaling models for the spray source strength (Kudrayetsev and Makin 2009; Mueller and Veron 2009; Fairall *et al.* 2009) were published where the source strength was linked to wave and breaking wave properties. Fairall *et al.* (2009) included laboratory verification of some of the model assumptions. Vickery *et al.* (2009) analyses of wind profiles from low-level dropsondes found that the drag coefficient, given similar wind speeds, is smaller for smaller-radii storms; enhanced sea spray by short or breaking waves was speculated as a cause Andreas (2010) published a scaling parameterization of the heat and salinity fluxes at high winds. Several papers (Kihara and Hirakuchi 2008; Innocentini

and Goncalves 2010) have appeared that essentially use very high-resolution 1-D models to study the effects of injection, acceleration, and evaporation of sea spray on near-surface profiles of winds, temperature, humidity, and their fluxes.

As shown in Fig. 32, Bao *et al.* (2010) have done a study of sensitivity of the hurricane WRF model to a new spray parameterization that incorporates both momentum and thermodynamic effects. This parameterization has now been implemented and tested in the GFDL coupled atmosphere-wave-ocean hurricane model. The scheme predicts that the overall impact of sea-spray droplets on the mean winds depends on the wind speed at the level of sea-spray generation. As the wind speed increases, the droplet size increases and the overall wind speed in the surface layer above the level of sea-spray generation increases, indicating that the increase of droplet size due to the increase of wind speed enhances the vertical mixing. This is consistent with observations and results from wind velocities that increase the overall enthalpy flux in the storm inner core shown in Fig. 31.

4.4.5: Atmospheric response to ocean forcing

It has previously been stated that understanding interactions between TCs and the ocean is crucial to decreasing the extent of the overestimations that are currently made of TC intensities and intensification rates. The atmospheric response to TC-induced sea surface cooling and the impact such a response has on an idealized TC-like vortex has been investigated using atmosphere-ocean coupled models, and an atmosphere-wave-ocean coupled model has recently been developed to numerically simulate TCs. It has been shown in numerical experiments that TC-induced sea surface cooling leads to the suppression of the intensity of an idealized TC-like vortex, resulting in decreased latent heat fluxes within the inner core of the vortex and increased inner-core asymmetries. Wada *et al.* (2013) showed that the impact of preexisting oceanic conditions on central pressure simulations and the axisymmetric structure of Typhoon Choi-wan (2009) depended on the phase of the simulated typhoon. The maximum range of the simulated central pressure was ~10 hPa during the mature phase of the simulated typhoon.

Wada *et al.* (2014) evaluated the impacts of four typhoons using an atmosphere-wave-ocean coupled model to determine the impacts of typhoon-induced sea surface cooling on typhoon predictions. The coupled model simulated sea surface cooling and the resultant increases in the central pressures caused by the passages of the typhoons reasonably well. When asymmetrically simulated, the mean sea surface cooling beneath a typhoon decreased the latent heat fluxes by 24% to 47%. A larger cooling effect gave a larger decrease in the latent heat flux only during the intensification phase. The decrease in the latent heat flux affected the inner core structure, particularly in the inflow boundary layer and around the eyewall. The cooling effect significantly affected the track simulation only for Typhoon Muifa, which had the weakest zonal steering flow of the four typhoons.

As shown in Fig. 33, Ito *et al.* (2014) performed a large number of high-resolution calculations by running the Japan Meteorological Agency (JMA) non-hydrostatic atmospheric model (AMSM) and AMSM coupled with a simple upper ocean model (CMSM). They compiled 281 3-day forecasts for 34 TCs from April 2009 to September

2012 for each model. The performance of these models is compared with the JMA global atmospheric model (GSM) that is used for the operational TC intensity guidance. The TC intensities are better predicted by CMSM than the other models. The improvement rates in CMSM relative to GSM and AMSM generally increase with increasing forecast time (FT). CMSM is better than GSM and AMSM by 27.4% and 21.3% at FT=48 h in terms of minimum sea level pressure, respectively. Regarding maximum wind speed, CMSM is better than GSM and AMSM by 12.8% and 19.5% at FT=48 h. This is due to smaller initial intensity error and sea surface cooling, which is consistent with in situ observations.

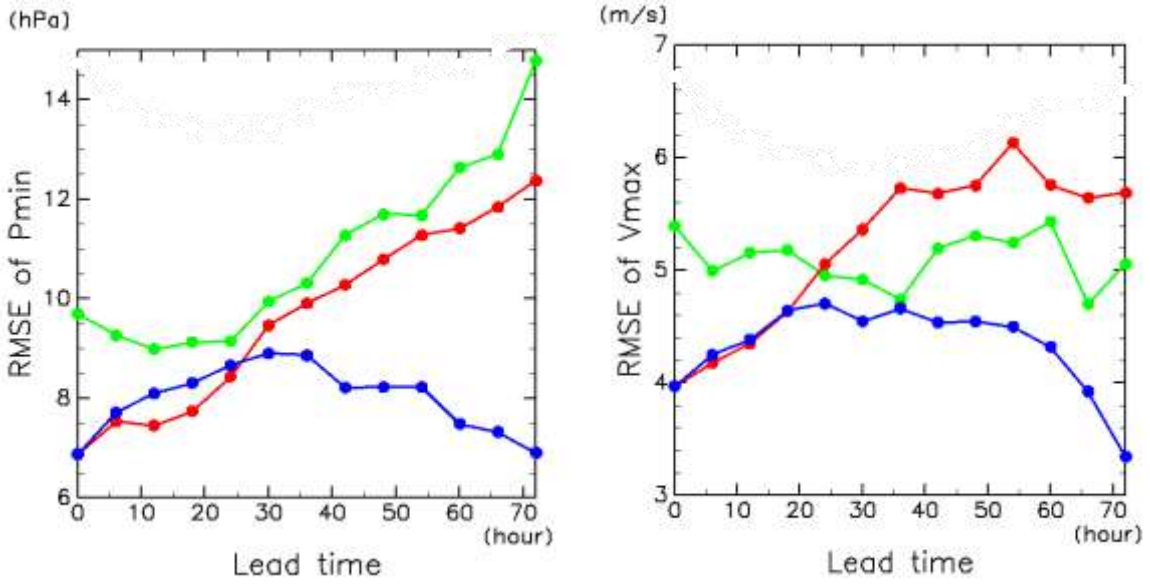

Figure 33: Root mean square error (RMSE) of (a) Pmin and (b) Vmax relative to the RSMC best track. The results are shown for GSM (green), AMSM (red) and CMSM (blue) (From Ito *et al.* 2014).

During TC-Earl (cat 4 hurricane), bulk air-sea fluxes of enthalpy and momentum were estimated relative to intensity change and underlying upper-ocean thermal structure from *in-situ* and satellite derived fields and seven clusters of GPS sondes (Hock and Franklin 1999). Earl moved over three ocean regimes: a weakly stratified, warm deep regime where the ocean heat content (OHC) variability relative to the 26^{o}C isotherm exceeded 90 kJ cm^{-2}; a transition regime where OHC gradually decreased in the direction of storm propagation, indicative of increasing temperature stratification; and a cool, highly stratified regime where OHC vanished (Fig. 34a). The OHC response to Earl was smaller over the warm regime, indicative of small SST cooling response (< 0.5^{o}C); it attained maximum values over the transition regime (because of tighter horizontal and vertical gradients in thermal structure); and it nearly vanished over the cool regime where the ocean temperatures were less than the air-temperature (e.g., downward enthalpy fluxes (Fig. 34b)). The sea surface heat loss through enthalpy fluxes over the warm ocean regime was comparable to the OHC response during the forced stage, where the storm experienced rapid intensification (RI). By contrast, the sea surface heat loss to the storm over the ocean transition regime was between 15 to 40% of the total in-storm OHC response (Fig. 34b).

This variability in upper-ocean cooling responses underscores the need of including realistic ocean structures in coupled numerical models for hurricane intensity forecasting.

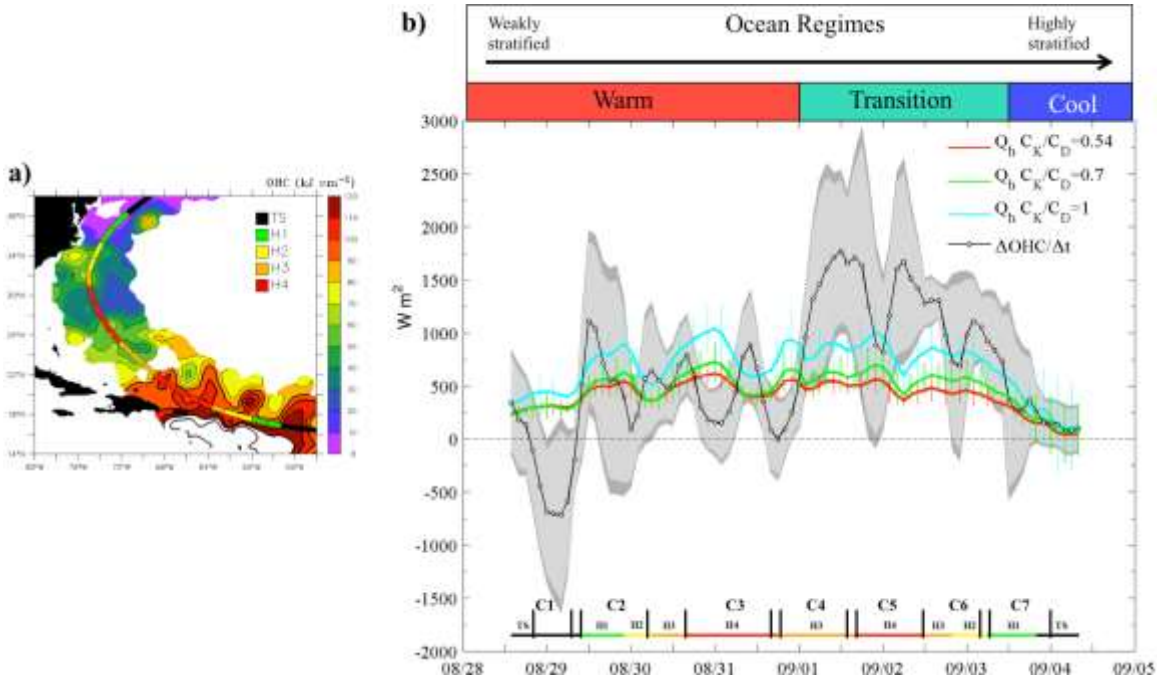

Figure 34. (a) OHC structure encountered by Earl; color in the storm's track is for intensity as per the legend. (b) OHC response ($\Delta OHC/\Delta t$, where Δt=24 h), and sea surface heat loss by enthalpy fluxes (Q_h), averaged in the cross-track direction from -9R_{max} to 9R_{max}, where R_{max} is the storm's radius of maximum winds; grey shade and vertical color bars are for standard deviation; C1 to C7 are labels for dropsonde clusters 1 to 7. A ratio C_k/C_D of the exchange coefficients of enthalpy (C_k) and momentum (C_D) between 0.54 and 0.7 produced reliable estimates for the fluxes relative to OHC changes, even during RI in C2; a ratio C_k/C_D=1 overestimated the fluxes (from Jaimes *et al.* 2014).

As summarized in Fig. 35, enthalpy fluxes impacted intensity fluctuations. This buoyancy forcing grew faster, peaked earlier, and decayed earlier than the maximum wind speed. This result suggests that, rather than controlling heat intake, the wind field adjusted to horizontal pressure gradients created by buoyancy forcing. Rather than being controlled by just SSTs, fluxes were influenced by underlying OHC structures where maximum fluxes were observed. In contrast, the enthalpy fluxes vanished as the OHC was reduced (SST < 26^{o}C). A steep increase in enthalpy fluxes was observed during RI in C2. The most important result is that bulk enthalpy fluxes were controlled by the thermodynamic disequilibrium between the sea surface and the near-surface air, independently of wind speed. This disequilibrium was strongly influenced by underlying warm oceanic features; localized maxima in enthalpy fluxes developed over tight horizontal gradients of moisture disequilibrium over these eddy features. These regions of local buoyant forcing preferentially developed during RI. The overall magnitude of the moisture disequilibrium ($\Delta q=q_s-q_a$) was determined by the saturation specific humidity at sea surface temperature (q_s) rather than by the specific humidity of the atmospheric environment (q_a). These results

support the hypothesis that intense local buoyant forcing by the ocean could be an important intensification mechanism in tropical cyclones over warm oceanic features.

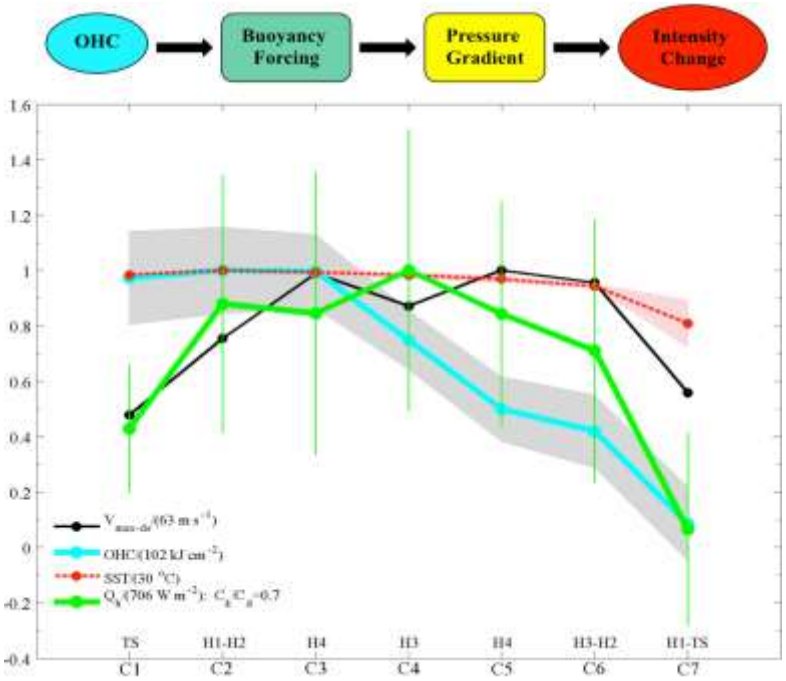

Figure 35: Processes observed in TC Earl, in terms of cluster-averaged storm and oceanic properties along Earl's track (See Fig. 1 for the definition of clusters), normalized by their corresponding overall maximum value (parenthesis). $V_{max\text{-}ds}$ is the maximum wind speed measured by a dropsonde in the cluster. Color shades and bars are for standard deviation (Jaimes *et al.* 2014).

During ITOP, pre-TC upper ocean thermal profiles were observed by the Argo floats during Megi, Fanapi, and Malakas (Fig. 36). These profiles were used as input to the 3D PWP (Price *et al.* 1994) ocean mixed layer model to estimate during-TC SST during their intensification (Fig. 36b). The drag coefficient used in the 3DPWP model was based on Powell *et al*. (2003). The colored triangles represent the WC-130 aircraft observed during-intensification SST. As multiple aircraft penetration flights to each of the 3 typhoons, each triangle represents the averaged from each flight, obtained within the 17 m s^{-1} (34 kts) radii of each TC. The simulations of SST (i.e. curves in Fig. 36b) match well with the *in-situ* observed during the intensification phases (triangles in Fig. 36b). The corresponding enthalpy fluxes (Fig 36c) were calculated using exchange coefficients from CBLAST (Black *et al.* 2007) based on near-surface atmospheric temperature and humidity data from aircraft measurements including GPS sondes (Hock and Franklin 1999). Enthalpy fluxes ranged from 0.4 to 1.4 kW m^{-2} where the largest was from ST Megi with its deep ocean structure and high OHC of ~120 kJ cm^{-2}. The enthalpy fluxes were roughly 0.8 kW m^{-2} encountering OHC values of 70 kJ cm^{-2} that reached cat-3 status (Lin *et al.* 2013; D'Asaro *et al.* 2013). During TC Malakas, the storm deepened to cat-2 status while moving over relatively shallow OML that supported an enthalpy flux of ~0.6 kW m^{-2}. Some of the AXBT profiles may be ~5 m shallow due to processing errors. These maximum enthalpy fluxes strongly point to the relative importance of the underlying OML and the corresponding values of OHC on the intensity changes of these three TCs in the western Pacific Ocean basin.

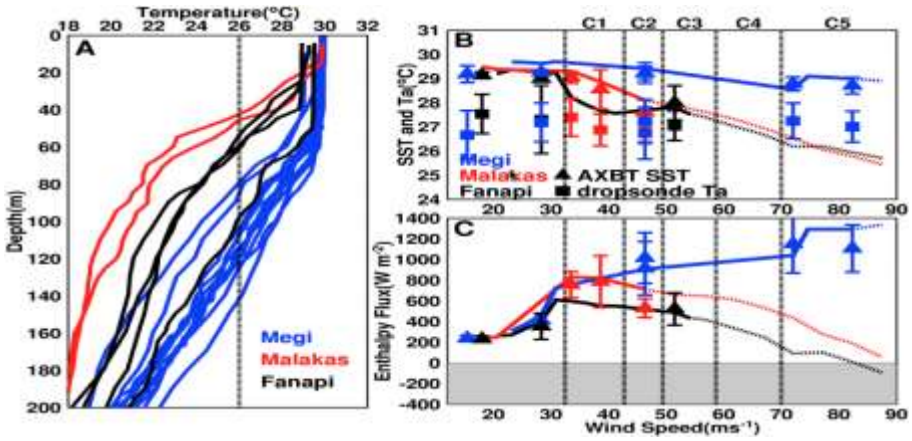

Figure. 36: (a) Pre-storm temperature profiles for each ITOP storm from ARGO floats. (b) Symbols: SSTs and air temperature (AT) at the core of each storm as measured by dropsonde/AXBT pairs deployed into the storms. Lines are results of an ocean model driven by the observed storms (solid) and same extrapolated to higher wind speeds (dashed). (c) Same as (b), but for estimated total enthalpy flux inside 34-kt radii (after Lin *et al.* 2013).

4.4.6: Summary

Considerable ocean-atmosphere variability occurs over the storm scales that include fundamental length scales such as the radius of maximum winds and another scale that includes the radius to gale-force winds. Here, the fundamental science questions are how the two fluids are coupled through OML and air-sea interface processes, and what are the fundamental time scales of this interaction? These questions are not easily answered as the interactions must be occurring over various time/space scales. For example, one school of thought is that the only important process with respect to the ocean is under the eyewall where ocean cooling has occurred. While it is at the eyewall where the maximum wind and enthalpy fluxes occur, the broad surface circulation over the warm OML also has non-zero fluxes that are contributing thermal energy to the TC. Thus, the deeper the OML (and 26^{o}C isotherm depth), more heat (OHC) is available to the storm through the enthalpy fluxes largely through moisture disequilibrium. In this context, process studies must begin to assess this atmospheric variability relative to warm and cold ocean features.

With regard to the oceanic response to the atmospheric forcing, an important missing ingredient in many studies is the role of the forced and background current fields. In addition to aircraft-based sampling by AXCPs and AXCTDs and new profiling floats such as the EMAPEX and the SOLO (during CBLAST and ITOP), efforts along the southeastern United States are underway to deploy long-range, HF-radars to map the surface currents to 200 km from the coast as part of an integrated ocean observing system. Such measurements would not only be invaluable to map the wind-driven surface currents during high winds, but also in the case of phased arrays, to map the directional wave spectra over the domain. These measurements could then be used to not only examine air-sea interactions, but also assess the relative importance of surface wave-current interactions under strong wind conditions in an Eulerian frame of reference.

Due to high noise with respect to signal, profiling devices provide less accurate measurements in the top few meters of the ocean. In order to gain better understanding of air-sea interaction, it is essential to have accurate information in the near-surface layer and the sea surface boundary layer.

The variability of the surface drag coefficient has received considerable attention over the last five years including the Coupled Boundary Layer and Air-Sea Transfer (CBLAST) program sponsored by the Office of Naval Research. Several treatments have come to the conclusion that there is a leveling off or a saturation value at ~ 30 m s^{-1} +/- 3 m s^{-1}. The ratio of the enthalpy coefficient and the drag coefficient is central to air sea fluxes impacting the TC boundary layer. In this context, the relationship between the coupled processes such as wave breaking and the generation of sea spray and how this is linked to localized air-sea fluxes remains a fertile research area. A key element of this topic is the atmospheric response to the oceanic forcing where there seems to be contrasting viewpoints. One argument is that the air-sea interactions are occurring over surface wave (wind-wave) time and space scales and cause significant intensity changes by more than a category due to very large surface drag coefficients. Yet empirical studies suggest the values to be between 1.5 to 4 x 10^{-3} compared to recent coupled model studies. While, these sub-mesoscale phenomena may affect the enthalpy fluxes, the first-order balances are primarily between the atmospheric and oceanic mixed layers.

4.4.7: Recommendations

The recommendations are:

i.) Given the range of uncertainty in the surface drag (e.g., wave effects), heat fluxes (e.g., sea spray), and initial conditions (e.g., wind field) beyond 30 m s^{-1}, assess how these combined uncertainties propagate through the coupled ocean-hurricane model;

ii.) Develop an archive of data sets and model outputs and make these archives publicly available for research and operational purposes. Investigate the potential use of these data sets in assimilation, evaluation, and verification of ocean models and parameterization schemes;

iii.) Create an *in-situ* tropical cyclone ocean-atmosphere observing program for pre-storm, storm, and post-storm environments. Develop optimal and co-located observing strategies and observational mixes of sensors for spatial evolution of upper ocean, interface, and atmospheric boundary layer structure; and;

iv.) Develop improved ocean model initialization schemes through data assimilation of satellite and in situ measurements, and test mixing parameterizations for a spectrum of ocean, wave and atmospheric conditions including the impact of waves on the surface heat, moisture, and momentum fluxes, and thus on the evolving OML.

A common theme is that international research and forecasting programs need to build on recent field programs (ONR-CBLAST, ONR-ITOP, NSF-sponsored measurements on

Hurricane Isidore and Lili; NOAA IFEX and MMS Loop Current Dynamics Study, NOAA HFIP) and acquire *in situ* data over a broad spectrum of atmospheric and oceanographic forcing regimes. These data are needed to test models and examine the parameter space in these air-sea interaction and vertical mixing schemes. Ultimately, future research initiatives must now have strong experimental, empirical, analytical, and numerical modeling components to further improve our understanding of the complex coupling processes between these two fluids.

4.4.8: Glossary of Terms

1-D: One-Dimensional
3-D: Three-Dimensional
ADCP: Acoustic Doppler Current Profiler
AMSR: Advanced Microwave Sounding Radiometer
AXBT : Airborne Expendable Bathythermograph
AXCP: Airborne Expendable Current Profiler
AXCTD: Airborne Expendable Conductivity Temperature Depth profiler
CBLAST: Coupled Boundary Layer Air-Sea Transfer Experiment
CCR: Cold Core Rings
CHIPS : Coupled Hurricane Intensity Prediction Scheme
COARE : Coupled Ocean and Atmospheric Response Experiment
CWW : Coupled Wind Wave model
EMAPEX: Electromagnetic Autonomous Profiling Explorer Floats
EPAC: Eastern Pacific Ocean Basin
EPIC : Eastern Pacific Investigation of Climate
FC: Florida Current
GCW: Gulf of Mexico Common water
GFDL : Geophysical Fluid Dynamics Laboratory
GISS: Goddard Institute for Space Studies Level-2 closure
GOM: Gulf of Mexico
GPS: Global Positioning System
HEXOS: Humidity Exchange Over the Sea
HYCOM: Hybrid Coordinate Ocean Model
IFEX: Intensity Fluctuation Experiment
IP: Inertial Period
ITOP: Interaction of Tropical Cyclone and Ocean
JMA: Japan Meteorological Agency
KPP: K-Profile Parameterization scheme
KT: Kraus, Turner turbulence balance model
MY: Mellor-Yamada 2.5 level Closure Scheme
LC: Loop Current
OML: Ocean Mixed Layer
ONR : Office of Naval Research
OHC: Oceanic Heat Content
OI: Optimal Interpolation
MODAS: Modular Ocean Data Assimilation Scheme
MODIS: Moderate Resolution Microwave Sounding Unit

MLD : Mixed Layer Depth
MLT : Mixed Layer Temperature
MPI: Maximum Potential Intensity
NASA : National Aeronautics and Space Administration (US)
NDBC : NOAA's National Data Buoy Center
NRL : US Navy Research Laboratories
NSF : National Science Foundation (US)
NOAA: National Oceanic and Atmospheric Administration (US)
PWP: Price, Weller and Pinkel dynamical instability model
PSU : Practical Salinity Unit (psu)
REGWNP: Regression Analysis of Western North Pacific
SHA: Sea-Surface Height Anomaly (SSHA)
SFMR : Stepped Frequency Microwave Radiometer
SRA : Scanning Radar Altimeter
SHIPS: Statistical Hurricane Intensity Prediction Scheme
SST: Sea Surface Temperature
TAO : Tropical Ocean Atmosphere Mooring Array as a result of TOGA
TC: Tropical Cyclone
TCHP: Tropical Cyclone Heat Potential
TOPEX: The Topographic Experiment (Radar Altimeter)
TMI: Tropical Rain Measuring Mission (TRMM) Microwave Imager
TOGA : Tropical Ocean Global Atmosphere Program
WATL : Western Atlantic Ocean
WPAC: Western Pacific Ocean Basin
WCR: warm core rings
XBT: Expendable Bathythermographs

4.4.9: References

Ali, M. M., P. S. V. Jagadeesh, and S. Jain, 2007: Effects of eddies on Bay of Bengal cyclone intensity, *EOS*, **88**, 93,95.

Ali, M. M., D. Swain, T. Kashyap, J. P. McCreary and P. V. Nagamani, 2013a: Relationship between Cyclone Intensities and Sea Surface Temperature in the Tropical Indian Ocean, *IEEE Geoscience and Rem. Sens. Letters*. **10**, pp 841 – 844.

Ali, M. M., T. Kashyap and P. V. Nagamani, 2013b: Use of Sea Surface Temperature for Cyclone Intensity Prediction Needs a Relook, *EOS*, **94**, pp 117.

Andreas, E.L, 2010: Spray-mediated enthalpy flux to the atmosphere and salt flux to the ocean in high winds. *J. Phys. Oceanogr*., **40**, 608-619.

Balaguru, K., P. Chang, R. Saravanan, L. R. Leung, Z. Xu, M. Li, and J. S. Hsieh, 2012: Ocean barrier layers' effect on tropical cyclone intensification. *Proceedings of the National Academy of Sciences*, **109(36),** 14343-14347.

Bao, J.-W., J. M. Wilczak, J. K. Choi, and L. H. Kantha, 2000: Numerical simulations of air-sea interaction under high wind conditions using a coupled model: A study of hurricane development. *Mon. Wea. Rev*., **128**, 2190-2210.

Bao, J.-W., C. W. Fairall, S. A. Michelson, and L. Bianco, 2010: Parameterizations of sea-spray impact on the air-sea momentum and heat fluxes. *Mon. Wea. Rev*., to appear.

Baranowski, D. B., P. J. Flatau, S. Chen, and P. G. Black, 2014: Upper ocean response to the passage of two sequential typhoons. *Ocean Science*, **10(3),** 559-570.

Bender, M. and I. Ginis, 2000: Real-time simulation of hurricane-ocean interaction. *Mon. Wea. Rev.*, **128,** 917-946.

Bister, M., and K. A. Emanuel, 1998: Dissipative heating and hurricane intensity. *Meteor. Atmos. Phys.*, **65**, 233–240.

Black, P.G., R.L.Elsberry and L.K. Shay, 1988: Airborne surveys of ocean current and temperature perturbations induced by hurricanes. *Adv. Underwater Tech.*, **16**, 51 - 59.

Black, P. G., E. A. D'Asaro, W. Drennan, J. R. French, P. P. Niiler, T. B. Sanford, E. J. Terrill, E. J. Walsh, and J. Zhang, 2007: Air-sea exchange in hurricanes: synthesis of observations from the Coupled Boundary Layer Air-Sea Transfer experiment. *BAMS*, **88**, 357-384.

Brassington, G. B., T. Pugh, C. Spillman, E. Schulz, H. Beggs, A. Schiller and P. R. Oke, 2007: BLUElink: Development of operational oceanography and servicing in Australia. *Journal of Research and Practice in Information Technology* **39,** 151-164.

Braun, S. A. and W.-K. Tao, 2000: Sensitivity of high resolution simulations of hurricane Bob (1991) to planetary boundary layer paramterizations. *Mon. Wea. Rev*., **128**, 3941-3961.

Canuto, V. M., A. Howard, Y. Cheng, and M. S. Dubovikov, 2001: Ocean turbulence. Part I: One-point closure model-momentum and heat vertical diffusivities. *J. Phys. Oceanogr*., **31**, 1413-1426.

Canuto, V. M., A. Howard, Y. Cheng, and M. S. Dubovikov, 2002: Ocean turbulence. Part II: Vertical diffusivities of momentum, heat, salt, mass, and passive scalars, *J. Phys. Oceanogr*., **32**, 240-264.

Chan, J.C.L., Y. Duan and L.K. Shay. 2001: Tropical cyclone intensity change from a simple ocean-atmospheric coupled model. *J. Atmos. Sci.*, **58**, 154-172.

Chan, J. C., and J. D. Kepert, 2010: Global perspectives on Tropical cyclones: From science to mitigation, **4**, World Scientific, Eds. 2.

Chao, Y. Y., J. H. G. M. Alves and H. L. Tolman, 2005: An operational system for predicting hurricane-generated wind waves in the North Atlantic Ocean, *Wea. Forecasting*, **20**, 652-671.

Charnock, H., 1955: Wind stress on a water surface. *Quart. J. Royal Meteor. Soc*., 639-640.

Chassignet, E. P., L. Smith, G. R. Halliwell, and R. Bleck, 2003: North Atlantic simulations with the hybrid coordinate ocean model (HYCOM): Impact of the vertical coordinate choice and resolution, reference density, and thermobaricity. *J. Phys. Oceanogr.*, **33**, 2504-2526.

Chen, S. S., J. F. Price, W. Zhao, M. Donelan, and E. J. Walsh, 2007: The CBLAST Hurricane program and the next generation fully coupled atmosphere-wave-ocean models for hurricane research and prediction., *BAMS*, **88**, 311-317.

Chen, S., T. J. Campbell, H. Jin, S. Gaberšek, R. M. Hodur and P. Martin, 2010: Effect of two-way air-sea coupling in high and low wind speed regimes. *Mon. Wea. Rev.*, **138**, 3579–3602.

Chen, S., S. Gaberšek, J. D. Doyle, J. Cook, P. Chu, P. R. A. Allard, E. Rogers, Wittmann, W. Nuss, 2014: Validation Test Report for the Coupled Ocean/Atmosphere Mesoscale Prediction System (COAMPS) Version 5.0: Air/Wave Component Validation. Naval Research Laboratory Memorandum Report, NRL/MR/ 7533-9526, 68 pp.

Cheney, R., L. Miller, R. Agreen, N. Doyle, and J. Lillibridge, 1994:, TOPEX/Poseidon: The 2-cm solution. *J. Geophys. Res*., **99,** 24,555-24,563.

Church, J.A., T.M. Joyce, and J.F. Price, 1989: Current and density observation across the wake of Hurricane Gay, *J. Phys. Oceanogr.*, **19**, 259-265.

Cione, J.J., and E.W. Uhlhorn, 2003: Sea surface temperature variability in hurricanes: Implications with respect to intensity change. *Mon. Wea. Rev*., **131**, 1783-1796.

Cione, J. J., E. A. Kalina, J. A. Zhang, and E. W. Uhlhorn, 2013: Observations of air–sea interaction and intensity change in hurricanes. *Mon. Wea. Rev.*, **141**, 2368–2382.

Cummings, J. A, 2003: Ocean data assimilation, *In* COAMPS: Version 3 Model Description, NRL Publication *NRL/PU/7500-03-448*. Naval Research Laboratory, Washington, DC, 20375, 21-28.

Daniel, T., J. Manley, and N. Trenaman, 2011: The Wave Glider: enabling a new approach to persistent ocean observation and research. *Ocean Dynamics*, **61**, 1509-1520.

Dare, R. A. and N. E. Davidson, 2004: Characteristics of Tropical Cyclones in the Australian Region. *Mon. Wea. Rev.*, **132**, 3049-3065.

D'Asaro, E. A., 2003: The ocean boundary layer under hurricane Dennis. *J. Phys. Oceanogr*., **33**, 561-579.

D'Asaro, E. A., T. B. Sanford, E. Terrill, and P. Niiler, 2007: Cold wake of hurricane Francis, *Geophys Res. Lett.*, 34, L15609, doi:10.1029/2007GL030160, 6 pp.

D'Asaro, E., P. Black, L. Centurioni, P. Harr, S. Jayne, I.-I. Lin, C. Lee, J. Morzel, R. Mrvaljevic, P. P. Niiler, L. Rainville, T. Sanford, and T. Y. Tang, 2011: Typhoon-ocean interaction in the western North Pacific: Part 1. *Oceanography*, **24**(4), 24–31.

D'Asaro, E., P. Black, L. Centurioni, P. Harr, S. Jayne, I.-I. Lin, C. Lee, J. Morzel, R. Mrvaljevic, P. P. Niiler, L. Rainville, T. Sanford, and T. Y. Tang, 2013: Impact of typhoons on the ocean in the Pacific: ITOP. *Bull. Am. Meteorol. Soc.*, doi:10.1175/BAMS-D-12-00104.1.

DeCosmo, J. B., K. B. Katsaros, S. D. Smith, R. J. Anderson, W. A. Oost, K. Bumke, and H. Chadwick, 1996: Air-sea exchange of water vapor and sensible heat: The Humidity Exchange over the Sea (HEXOS) results. *J. Geophys. Res.*, **101**, 12,001-12,016.

DeMaria, M., M. Mainelli, L. K. Shay, J. Knaff, and J. Kaplan, 2005: Further improvements to the statistical hurricane intensity prediction scheme. *Wea and Forecasting,* **20**, 531-543.

Donelan, M A., 1990: Air-sea interaction. The Sea, B. LeMehaute abnd D. Hanes, Eds, *Ocean Engineering Science*, **9**, John Wiley and Sons, 239-292.

Donelan, M. A., B. K. Haus, N. Reul, W. J. Plant, M. Stiassine, H. Graber, O. Brown, and E. Saltzman, 2004: On the limiting aerodynamic roughness of the ocean in very strong winds. *Geophys. Res. Letters*., 31L18306,doi:1029/2004GRL019460.

Donelan, M. A., M. Curcic, S. S. Chen, and A. K. Magnusson, 2012: Modeling waves and wind stress, *J. Geophys. Res. Oceans,* **117**, 1–26. doi: 10.1029/2011JC007787

Drennan, W. M. and L. K. Shay. 2006: On the variability of the fluxes of momentum and sensible heat. *Bound. Layer Meteor.,* **119(1)**, 81-107.

Drennan, W. M., J. A. Zhang, J. R. French, C. McCormick, and P. G. Black, 2007: Turbulent fluxes in the hurricane boundary layer, Part II: Latent heat flux. *J. Atmos. Sci.,* **64,** 1103- 1115.

Elliot, B. A., 1982: Anticyclonic rings in the Gulf of Mexico, *J. Phys. Oceanogr.,* **12**, 1292-1309.

Emanuel, K A., 1986: An air-sea interaction theory for tropical cyclones Part 1: Steady-State maintenance**.** *J. Atmos. Sci***.,** **43,** 585-605.

Emanuel, K. A., 1988: The maximum intensity of hurricanes. *J. Atmos. Sci.* **45**, 1143–1155.

Emanuel, K A., 1995: Sensitivity of tropical cyclones to surface exchange and a revised steady-state model incorporating eye dynamics**.** *J. Atmos. Sci.* **, 52,** 3969-3976.

Fairall, C.W., M. Banner, W. Peirson, R. P. Morison, and W. Asher, 2009: Investigation of the physical scaling of sea spray spume droplet production. *J. Geophys., Res*., **114**, C10001, doi:10.1029/2008JC004918.

Falkovich, A., I. Ginis, and S. Lord, 2005: Implementation of data assimilation and ocean initialization for the coupled GFDL/URI hurricane prediction system. *J. Atmos. and Ocean. Tech.*, **22**, 1918–1932.

Fan, Y., I. Ginis, T. Hara, C. W. Wright, and E. Walsh, 2009a: Numerical simulations and observations of surface wave fields under an extreme tropical cyclone. *J. Phys. Oceanogr.*, **39**, 2097-2116.

Fan, Y., I. Ginis, and T. Hara, 2009b: The effect of wind-wave-current interaction on air-sea momentum fluxes and ocean response in tropical cyclones. *J. Phys. Oceanogr*., **39**, 1019-1034.

Fan, Y., I. Ginis, and T. Hara, 2010: Momentum flux budget across air-sea interface under uniform and tropical cyclones winds. *J. Phys. Oceanogr*., **40**, 2221-2241.

Findlater, J., 1969: A major low-level air current near the Indian Ocean during the northern summer. *Quart. J. R. Met. Soc*., **95,** 362-380.

French, J. R., W. M. Drennan, J. A. Zhang, and P. G. Black, 2007: Turbulent fluxes in the hurricane boundary layer. Part 1: Momentum flux. *J. Atmos. Sci.*, **64,** 1089-1102.

Gaspar, Ph., 1988: Modeling the seasonal cycle of the upper ocean. *J. Phys. Oceanogr*., **18**, 161-180.

Gill, A. E., 1984: On the behavior of internal waves in the wakes of storms. *J. Phys. Oceanogr*., **14**, 1129-1151.

Ginis, I., 1995: Interaction of tropical cyclones with the ocean. *In Global Perspective of Tropical Cyclones,* Chapter 5, Ed. R. L. Elsberry, **Tech. Document WMO/TD 693**, World Meteorological Organization, Geneva, Switzerland, 198-260.

Goni, G. J., S. Kamholz, S. L. Garzoli, and D. B. Olson, 1996: Dynamics of the Brazil/Malvinas confluence based on inverted echo sounders and altimetry. *J. Geophys. Res.*, **95,** 22103-22120.

Greatbatch, R.J., 1983: On the response of the ocean to a moving storm: nonlinear dynamics. *J. Phys. Oceanogr.*, **13**, 357-367.

Halliwell, Jr., G. R., 2004: Evaluation of vertical coordinate and vertical mixing algorithms in the hybrid-coordinate ocean model (HYCOM). *Ocean Modelling*, **7**, 285-322.

Halliwell, G., L. K. Shay, S. D. Jacob, O. Smedstad, and E. Uhlhorn, 2008: Improving ocean model initialization for coupled tropical cyclone forecast models using GODAE nowcasts. *Mon Wea Rev,* **136 (7)**, 2576–2591.

Halliwell, G., L. K. Shay, J. Brewster, and W. Teague, 2011: Evaluation and sensitivity analysis of an ocean model to hurricane Ivan in the northern Gulf of Mexico. *Mon. Wea. Rev*. , **139(3)**, 921-945.

Halliwell, Jr., G. R., A. Srinivasan, V. Kourafalou, H Yang, D. Willey, M. Le Henaff, and R. Atlas, 2014a. Rigorous evaluation of a fraternal twin ocean OSSE system in the open Gulf of Mexico. *J. Atmos. Ocean. Technol.*, 31, 105-130.

Halliwell, Jr., G. R., V. Kourafalou, M. Le Henaff, R. Atlas, and L. K. Shay, 2014b: OSSE impact analysis of airborne ocean surveys for improving upper-ocean dynamical and thermodynamical forecasts in the Gulf of Mexico. *Prog. in Oceanogr.*, submitted.

Hanshaw, M. N., M. S. Lozier, and J. B. Palter, 2008: Integrated impact of tropical cyclones on sea surface cholophyll in the North Atlantic. *Geophys. Res. Lett.*, **35**, L01601 doi:10.1029/3007 GL031862.

Hara, T., and S. E. Belcher, 2004: Wind profile and drag coefficient over mature ocean surface wave spectra. *J. Phys. Oceanogr*., **34,** 2345-2358.

Haus, B. K., Jeong, D., Donelan, M. A., Zhang, J. A., and Savelyev, I., 2010: Relative rates of sea-air heat transfer and frictional drag in very high winds. *Geophys. Res. Lett.*, ***37***. doi: 10.1029/2009GL042206

Hock, T. J., and J. L. Franklin, 1999: The NCAR GPS dropwindsonde. *BAMS*, **80**, 407-420.

Hong, X., S. W. Chang, S. Raman, L. K. Shay, and R. Hodur, 2000: The interaction of hurricane Opal (1995) and a warm core ring in the Gulf of Mexico. *Mon. Wea. Rev*., **128,** 1347-1365.

Innocentini, V., and I.A. Goncalves, 2010: The impact of spume droplets and wave stress parameterizations on simulated near-surface maritime wind and temperature. *J. Phys. Oceanogr*., **40**, 1373-1389.

Ito, K., T. Kuroda, K. Saito and A. Wada, 2014: Forecasting a large number of tropical cyclone intensities around Japan using a high-resolution atmosphere-ocean coupled model. *Wea. Forecasting*, accepted.

Jacob, D. S., L. K. Shay, A. J. Mariano, and P. G. Black, 2000: The three-dimensional mixed layer heat balance during hurricane Gilbert. *J. Phys. Oceanogr*., **30**, 1407-1429.

Jacob, S. D., and L. K. Shay, 2003: The role of oceanic mesoscale features on the tropical cyclone-induced mixed layer response. *J. Phys. Oceanogr*., **33**, 649-676.

Jacob, S. D., and C. Koblinsky, 2007: Effects of precipitation on the upper ocean response to a hurricane. *Mon Wea. Rev*.**,135**, 2207-2225.

Jaimes, B. and L. K. Shay. 2009: Mixed layer cooling in mesoscale eddies during Katrina and Rita. *Mon. Wea. Rev*.**, 137(12)**, 4188-4207.

Jaimes, B. and L. K. Shay. 2010: Near-inertial wave wake of hurricanes Katrina and Rita in mesoscale eddies. *J. Phys. Oceanogr*.. **40(6),** 1320-1337.

Jaimes, B., L. K. Shay, and G. R. Halliwell, 2011: The response of quasigeostrophic oceanic vorticies to tropical cyclone forcing. *J. Phys. Oceanogr*., **41**, 1965-1985.

Jaimes, B., L. K. Shay, and E. W. Uhlhorn, 2014: Enthalpy and momentum fluxes during Hurricane Earl (2010) relative to underlying ocean features. *Mon. Wea. Rev. (In Press)*

Jaimes, B.,and L. K. Shay, 2014: Enhanced wind-driven downwelling in warm ocean eddy features during the intensification of tropical cyclone Isaac (2012). *J. Phys. Oceanogr*. *(In Submission)*

Jarosz, E., D.A. Mitchell, D.W. Wang, and W.J. Teague, 2007: Bottom-up determination of air-sea momentum exchange under a major tropical cyclone. *Science*, **315**, 1707.

Jeong D., B. K. Haus, and M. A. Donelan, 2012: Enthalpy transfer across the air–water interface in high winds including spray. *J. Atmos. Sci.*, **69**, 2733-2748.

Jin, Y., W. T. Thompson, S. Wang, and C.-S. Liou, 2007: A numerical study of the effect of dissipative heating on tropical cyclone intensity. *Wea. Forecasting,* **22,** 950-966.

Jourdain, N. C., Lengaigne, M., Vialard, J., Madec, G., and others, 2013: Observation-based estimates of surface cooling inhibition by heavy rainfall under tropical cyclones. *J. Phys. Oceanogr.* , **43(1),** 205-221.

Jullien, S., Menkes, C.E., Marchesiello, P., Jourdain, N., Lengaigne, M., Koch-Larrouy, A., Lefèvre, J., et al., 2012: Impact of tropical cyclones on the heat budget of the South Pacific ocean. *J. Phys. Oceanogr*. **42**, 1882–1906.

Kantha, L.H., and C. A. Clayson, 2004: On the effect of surface gravity waves on mixing in the oceanic mixed layer. Ocean Model, **6**, 101-124.

Kihara, N. and H. Hirakuchi, 2008: A model for air–sea interaction bulk coefficient over a warm mature sea under strong wind. *J. Phys. Oceanogr*., **38**, 1313-1326.

Kraus, E.B. and J.S. Turner, 1967: A one-dimensional model of the seasonal thermocline. II: The general theory and its consequences. *Tellus*, **1**, 98-105.

Kudryavtsev, V. N., and V. K. Makin, 2009: Model of the spume sea spray generation. *Geophys. Res. Lett.*, **36**, L06801, doi:10.1029/2008GL036871

Kunze, E., and T. B. Sanford, 1984: Observations of near-inertial waves in a front. *J. Phys. Oceanogr.*, **14**, 566–581.

Large, W.G., and S. Pond, 1981: Open ocean momentum flux measurements in moderate to strong winds. J. *Phys. Oceanogr*., **11,** 324-336, 1981.

Large, W., S., J. C. McWilliams, and S. C. Doney, 1994: Oceanic vertical mixing: A review and a model with non-local boundary layer parameterization. *Rev. Geophys.*, **32,** 363-403.

Leben, R. R., 2005: Altimeter derived Loop Current metrics. In *Circulation in the Gulf of Mexico: observations and models, Geophys. Monogr.*, **161**, Amer. Geophys. Union, 181-201.

Leipper, D., and D. Volgenau, 1972: Hurricane heat potential of the Gulf of Mexico. *J. Phys. Oceanogr.*, **2,** 218-224.

Lin, I. I., W. Timothy Liu, Chuin-Chieh Wu, George T.F. Wong, Chuanmin Hu, Zhiqiang Chen, Wen-Der Liang, Yih Yang, and Kon-Kee Liu, 2003: New evidence for enhanced ocean primary production triggered by tropical cyclone, vol. 30, No. 13, 1718.

Lin, I-I., I.-F. Pun and C.-C. Wu, 2008: Upper ocean thermal structure and the western north Pacific Category 5 typhoons. Part I: Ocean features and category 5 typhoons' intensification. *Mon. Wea Rev*., **136**, 3288-3306.

Lin, I-I., I.-F. Pun and C.-C. Wu, 2009a: Upper ocean thermal structure and the western north Pacific Category 5 typhoons. Part II: Dependence on translation speed. *Mon. Wea Rev*., **137**, 3744-3757.

Lin, I-I, Chi-Hong Chen, I-F. Pun, W. Timothy Liu, and C.-C. Wu, 2009b: Warm ocean anomaly, air sea fluxes, and the rapid intensification of tropical cyclone Nargis (2008), *Geophys. Res. Lett,*

36, L03817, doi:10.1029/2008GL035815.

Lin, I. I., P. Black, J. F. Price, C. Y. Yang, S. S. Chen, C. C. Lien, C. C., and E. A. D'Asaro, 2013: An ocean coupling potential intensity index for tropical cyclones. *Geophysical Research Letters*, **40(9),** 1878-1882.

Mainelli, M., M. DeMaria, L. K. Shay and G. Goni, 2008: Application of oceanic heat content estimation to operational forecasting of recent category 5 hurricanes. *Wea. and Forecast*, **23**, 3-16.

Marks, F., and L.K. Shay, 1998: Landfalling tropical cyclones: Forecast problems and associated research opportunities: Report of the 5th Prospectus Development Team to the U.S. Weather Research Program, *BAMS*, **79**, 305-323.

McCaskill, E. C., and L. K. Shay 2014: The systematically merged Pacific Ocean regional temperature and salinity (SPORTS) climatology for typhoon intensity forecasts. *31th AMS Hurricane and Tropical Meteorology Conference*, 31 Mar-4 April, San Diego, CA, https://ams.confex.com/ams/31Hurr/webprogram/Paper244756.html (6pp. Extended Abstract).

Mellor, G. L., and T. Yamada, 1982: Development of a turbulence closure model for geophysical fluid problems. *Rev. Geophys. and Space Phys.*, **20,** 851-875.

Meyers, P. C., L. K. Shay and J. K. Brewster, 2014: Systematically merged Atlantic regional temperature and salinity (SMARTS) climatology for hurricane intensity forecasting. *J. Atmos. Oceanogr. Tech.* **31**, 131-149.

Moon, I., I. Ginis, and T. Hara, 2004a: Effect of surface waves on Charnock coefficient under tropical cyclones. *Geophys. Res. Lett.*, **31**, L20302.

Moon I.-J., I. Ginis, and T. Hara, 2004b: Effect of surface waves on air–sea momentum exchange. II: Behavior of drag coefficient under tropical cyclones. *J. Atmos. Sci.*, ***61,*** 2334–2348.

Moon, I., I. Ginis, and T. Hara, 2004c: Effect of surface waves on Charnock coefficient under tropical cyclones. *Geophys. Res. Lett.*, **31**, L20302.

Moon, I.-J., I. Ginis, and T. Hara, 2008: Impact of the reduced drag coefficient on ocean wave modeling under hurricane conditions. *Mon. Wea. Rev.*, **136**, 1217-1223.

Mrvaljevic, R. K., P. G. Black, L. R. Centurioni, Y.-T. Chang, E. A. D'Asaro, S. R. Jayne, and C. M. Lee, 2013:. Observations of the cold wake of Typhoon Fanapi (2010). *Geophys. Res. Lett.*, **40**, 316-321.

Mueller, J.A., and F. Veron, 2009: A sea-state dependent spume generation function. *J.Phys. Oceanogr*., **39,** 2363-2372.

Noh, Y. and H. J. Kim, 1999: Simulations of temperature and turbulence structure of the oceanic boundary layer with the improved near-surface process. *J. Geophys. Res.*, **104**, 15621-15634.

Oke, P. R., A. Schiller, D. A. Griffin and G. B. Brassington, 2005: Ensemble data assimilation for an eddy-resolving ocean model of the Australian region. *Quarterly Journal of the Royal Meteorological Society* **1,** 1-11.

Park, J., K.-A. Park, K. Kim, and Y.-H. Youn, 2005: Statistical analysis of upper ocean temperature response to typhoons from ARGO floats and satellite data. *IEEE*, 2564-2567.

Powell, M. D., and S. Houston, 1996: Hurricane Andrew's landfall in South Florida. Part II: surface wind fields. *Wea and Forecasting*., **11**, 329-349.
Powell, M.D., P.J. Vickery, and T.A. Reinhold, 2003: Reduced drag coefficient for high wind speeds in tropical cyclones. *Natur*e, **422,** 279-283.

Price, J. F., 1981: Upper ocean response to a hurricane. *J. Phys. Oceanogr.*, **11**, 153–175.

Price, J. F., R. A. Weller, and R. Pinkel, 1986: Diurnal cycling: Observations and models of the upper ocean response to diurnal heating, cooling and wind-mixing. *J. Geophys. Res.*,**7,** 8411-8427.

Price, J. F., T. B. Sanford, and G.Z. Forristall, 1994: Observations and simulations of the forced response to moving hurricanes. *J. Phys. Oceanogr*., **24**, 233-260.

Pudov, V., and S. Petrichenko, 2000: Trail of a typhoon in the salinity field of the ocean upper layer. *Atmospheric and Ocean Physics (Izvestiya Acad. Sci.*), **36**, 700-706.

Pun, I-F, I-I Lin, C. -R. Wu, D. -S. Ko, W. T. Liu, 2007: Validation and Application of Altimetry-derived Upper Ocean Thermal Structure in the Western North Pacific Ocean for Typhoon Intensity Forecast. *IEEE Trans. Geosci. Rem. Sens*., **45**, 1616-1630.

Pun, I-F, I-I Lin, and Min-Hui Lo, 2013: Recent Increase in High Tropical Cyclone Heat Potential Area in the Western North Pacific Ocean, *Geophysical Research Letters*. doi:10.1002/grl.50548, 3 Sep., 2013

Pun, I-F, I-I Lin, and Dong S. Ko, 2014: New Generation of Satellite-Derived Ocean Thermal Structure for the Western North Pacific Typhoon Intensity Forecasting, 2014: *Progress in Oceanography*, **121**, p 109-124 ,doi: 10.1016/j.pocean.2013.10.004

Rabe, T., Kukulka, T., I. Ginis, T. Hara, B. Reichl, E. D'Asaro, R. Harcourt, and P. P. Sullivan, 2014:. Langmuir turbulence under Hurricane Gustav. *J. Phys. Oceanogr*., (In Press).

Rao, R. R., 1984: A case study on the influence of the summer monsoonal vortex on the thermal structure of upper central Arabian Sea during the phase of the MONEX-79. *Deep-Sea Res.*, **31**, 1511-1521.

Rastigejev, Y. and Yuh-Lang Lin, 2010: A theoretical study of fine ocean spray on tropical cyclones. *J. Geophys. Res.*, submitted.

Reichl, B. G., T. Hara, and I. Ginis, 2014: Sea state dependence of the wind stress over the ocean under hurricane winds. *J. Geophys. Res*., **119**, 30-51.

Rogers, R., S. Aberson, M. Black, P. Black, J. Cione, P. Dodge, J. Dunion, J. Gamache, J. Kaplan, M. Powell, L. K. Shay, N. Surgi, and E. Uhlhorn, 2006: The intensity forecasting experiment (IFEX), a NOAA multiple year field program for improving intensity forecasts. *BAMS*, **87(11),** 1523-1537

Sanabia, E. R., B. S. Barrett, P. G. Black, S. Chen, and J. A. Cummings, 2013: Real-Time Upper-Ocean Temperature Observations from Aircraft during Operational Hurricane Reconnaissance Missions: AXBT Demonstration Project Year One Results. *Wea. Forecast.,* **28(6),** 1404-1422.

Sandery P. A., G. B Brassington, A. Craig and T. Pugh., 2010: Impacts of ocean-atmosphere coupling on tropical cyclone intensity change and ocean prediction in the Australian region, *Mon. Wea. Rev.*, **138**, 2074-2091.

Sanford, T.B., P.G. Black, J. Haustein, J.W. Feeney, G. Z. Forristall, and J.F. Price, 1987: Ocean response to a hurricane. Part I: Observations. *J. Phys. Oceanogr*., **17**, 2065-2083.

Sanford, T.B., J.H. Dunlap, J.A. Carlson, D.C. Webb and J. B. Girton, 2005: Autonomous velocity and density profiler: EM-APEX. Proceedings of the IEEE/OES 8th Working Conference on Current Measurement Technology, IEEE Cat No. 05CH37650, ISBN: 0-7803-8989-1, 152-156.

Sanford, T B., J. F. Price, J. Girton, and D. C. Webb, 2007: Highly resolved observations and simulations of the oceanic response to a hurricane. *Geophys. Res. Lett.*, **34,** L13604, 5 pp.

Sanford, T. B., J. F. Price, and J. B. Girton, 2011: Upper-ocean response to Hurricane Frances (2004) observed by profiling EM-APEX floats. *J. Phys. Oceanogr.*, 41, 1041-1056.

Schade, L., and K. Emanuel, 1999: The ocean's effect on the intensity of tropical cyclones: Results from a simple ocean-atmosphere model. *J. Atmos. Sci.*, **56**, 642-651.

Scharroo, R., W.H. Smith, and J.L. Lillibridge, 2005: Satellite altimetry and the intensification of Hurricane Katrina. *EOS,* **86,** 366-367.

Schiller, A., P. R. Oke, G. B. Brassington, M. Entel, R. Fiedler, D. A. Griffin and J. Mansbridge, 2008: Eddy-resolving ocean circulation in the Asian-Australian region inferred from an ocean reanalysis effort. *Prog. Oceanogr.* **76,** 335-365.

Shay, L.K., 2009: Upper Ocean Structure: a Revisit of the Response to Strong Forcing Events. In*: Encyclopedia of Ocean Sciences*, ed. John Steele, S.A. Thorpe, Karl Turekian and R. A. Weller, Elsevier Press International, Oxford, UK, 4619-4637, doi: 10.1016/B978-012374473-9.00628-7.

Shay, L. K., 2010: Air-sea interactions in tropical cyclones (Chapter 3). *In Global Perspectives of Tropical Cyclones:* 2nd Edition, World Scientific Publishing Company: Earth System Science Publication Series, London, UK, Edited by J. C. Chan and J. D. Kepert, pp 93-132.

Shay, L.K. and R.L. Elsberry, 1987: Near-inertial ocean current response to hurricane Frederic. *J. Phys. Oceanogr.*, **17**, 1249 – 1269.

Shay, L.K., and S.W. Chang, 1997: Free surface effects on the near-inertial ocean current response to a hurricane: A revisit. *J. Phys. Oceanogr*., **27**, 23 - 39.

Shay, L. K., G. J. Goni, and P. G. Black, 2000: Effects of a warm oceanic feature on hurricane Opal. *Mon. Wea. Rev.*, **128**, 1366-1383.

Shay, L. K, and S. D. Jacob, 2006: Relationship between oceanic energy fluxes and surface winds during tropical cyclone passage (Chapter 5). Atmosphere-Ocean Interactions II, *Advances in Fluid Mechanics*. Ed. W. Perrie, WIT Press, Southampton, UK, 115-142.

Shay, L. K., and E. W. Uhlhorn, 2008: Loop Current response to Hurricanes Isidore and Lili. *Mon Wea. Rev.*, **136**, 3248-3274 doi: 10.1175/2008MWR2169.

Shay, L. K., and J. Brewster. 2010: Eastern Pacific oceanic heat content estimation for hurricane forecasting. *Mon. Wea. Rev*, **138**, 2110-2131**.**

Smith, T.A., S. Chen, T. Campbell, E. Rogers, S. Gabersek, D. Wang, S. Carroll, and R. Allard, 2013: Ocean-wave coupled modeling in COAMPS-TC: A study of Hurricane Ivan (2004). Ocean Dynamics, **69**, 181-194.

Soloviev, A., and R. Lukas, 2010: Effects of bubbles and sea spray on air–sea exchange in hurricane conditions. *Bound.-Layer Meteorol.,* **136**, 365–376, DOI 10.1007/s10546-010-9505-0.

Soloviev, A., R. Lukas, M. A. Donelan, B. K. Haus and I. Ginis, 2014: The air-sea interface and surface stress under tropical cyclones. *Sci. Rep.*, 4, 5306; DOI:10.1038/srep05306.

Stern, M. E., 1965: Interaction of a uniform wind stress with a geostrophic vortex. *Deep-Sea Res.*, **12**, 355-367.

Sullivan, P. P., L. Romero, J. C. McWilliams, and W. K. Melville, 2012: Transient evolution of Langmuir turbulence in ocean boundary layers driven by hurricane winds and waves. J. Phys. Oceanogr., **42**(11), 1959-1980.

Sun, D..R. Gautam, G. Cervone, Z. Boyeyi, and M. Kaptos, 2006: Comment on Satellite altimetry and the intensification of Hurricane Katrina. *EOS*, **87(8),** 89

Sturges, W., and R. Leben, 2000: Frequency of ring separations from the Loop Current in the Gulf of Mexico: A revised estimate. *J. Phys. Oceanogr*., **30,** 1814-1819.

Teague, W. J., M. J. Carron, and P. J. Hogan, 1990: A comparison between the generalized digital environmental model and Levitus climatologies. *J. Geophys. Res*., **95**, 99-116.

Teague, W.J., E. Jarosz, D.W. Wang, and D.A. Mitchell, 2007: Observed oceanic response over the upper continental slope and outer shelf during Hurricane Ivan. *J. Phys. Oceanogr.*, **37**, 2181-2206.

Toba, Y., N. Iida, H. Kawamura *et al.,* 1990: The wave dependence of sea surface wind stress. *J. Phys. Oceanogr.* **20**, 705-721.

Tolman, H. L., 2002: User manual and system documentation of WAVEWATCH-III version 2.22. NOAA/NWS/NCEP/OMB Tech. Note 222, 133 pp.

Tolman H.L., J. H. G. M. Alves, Y. Y. and Chao, 2005: Operational forecasting of wind-generated waves by hurricane Isabel at NCEP, *Wea. Forecasting*, **20**, 544-557.

Uhlhorn, E. W., P. G. Black, J. L. Franklin, M. Goodberlet, J. Carswell and A. S. Goldstein, 2007:Hurricane surface wind measurements from an operational stepped frequency microwave radiometer. *Mon. Wea. Rev*., **135,** 3070-3085.

Uhlhorn, E., and L. K. Shay, 2012: Loop Current mixed layer response to hurricane Lili (2002). Part I: Observations. *J. Phys. Oceanogr.*, **42**, 400-419.

Uhlhorn, E., and L. K. Shay, 2013: Loop Current mixed layer response to hurricane Lili (2002). Part II: Modeling results. *J. Phys. Oceanogr.*, **43**, 1173-1192.

Vickery, P. J., D. Wadhera, M. D. Powell and Y. Chen, 2009: A hurricane boundary layer and wind field model for use in engineering applications. *J. Appl. Meteor. Climatol*, **48,** 381-405.

Vincent, E. M., Lengaigne, M., Madec, G., Vialard, J., and others (2012a). Processes setting the characteristics of sea surface cooling induced by tropical cyclones. *J. Geophys. Res. Oceans,* **117 (C2)** , 1978–2012.

Vincent, E. M., Lengaigne, M., Vialard, J., Madec, G., and others (2012b). Assessing the oceanic control on the amplitude of sea surface cooling induced by tropical cyclones. *J. Geophys. Res. Oceans,* **117 (C5)** , 1978–2012.

Wada, A., and N. Usui, 2007: Importance of tropical cyclone heat potential for tropical cyclone intensity and intensification in the western north Pacific. *J. of Oceanography*, **63**, 427-447.

Wada, A. and J. C. L. Chan , 2008: Relationship between typhoon activity and upper ocean heat content. *Geophys. Res. Lett.*, **35**, L17603.

Wada, A., H. Niino and H. Nakano, 2009: Roles of vertical turbulent mixing in the ocean response to Typhoon Rex (1998). *J. Oceanogr.*, **65**, 373-396.

Wada, A, N. Kohno and Y. Kawai, 2010a: Impact of wave-ocean interaction on Typhoon Hai-Tang in 2005. *SOLA*, **6A**, 13-16.

Wada, A. and N. Usui, 2010b: Impacts of Oceanic Preexisting Conditions on Predictions of Typhoon Hai-Tang in 2005. *Advances in Meteorology*, 756071.

Wada, A., T. Midorikawa, M. Ishii, and T. Motoi, 2011: Carbon system changes in the East China Sea induced by Typhoons Tina and Winnie in 1997, *Journal of Geophysical Research – Oceans*. **116**, C07014.

Wada, A., N. Usui, and K. Sato, 2012: Relationship of maximum tropical cyclone intensity to sea surface temperature and tropical cyclone heat potential in the North Pacific Ocean. *Journal of Geophysical Research - Atmosphere*, **117**, D11118.

Wada, A., N. Usui and M. Kunii, 2013a: Interactions between Typhoon Choi-wan (2009) and the Kuroshio Extension System. *Advances in Meteorology*, 859810.

Wada, A., M. F. Cronin, A. J. Sutton, Y. Kawai and M. Ishii, 2013b: Numerical simulations of oceanic pCO_2 variations and interactions between Typhoon Choi-wan (0914) and the ocean. *Journal of Geophysical Research - Oceans*, **118**, 2667-2684.

Wada, A., T. Uehara and S. Ishizaki, 2014: Typhoon-induced sea surface cooling during the 2011 and 2012 typhoon seasons: observational evidence and numerical investigations of the sea surface cooling effect using typhoon simulations. *Progress in Earth and Planetary Science*, **1**, 11.

Walker, N., R. R. Leben, and S. Balasubramanian 2005: Hurricane forced upwelling and chlorophyll a enhancement within cold core cyclones in the Gulf of Mexico. *Geophys. Res. Letter*, **32**, L18610, doi: 10.1029/2005GL023716, 1-5.

Wang, B., and X. Zhou , 2008: Climate variation and prediction of rapid intensification in tropical cyclones in the western North Pacific, *Meteorol. Atmos. Phys.*, **99**, 1– 16.

Wang, D.W., D.A. Mitchell, W.J. Teague, E. Jarosz, and M.S. Hulbert, 2005: Extreme waves under Hurricane Ivan. *Science*, **309**, 896.

Wang, Y., J. D. Kepert, and G. J. Holland, 2001: The effect of sea spray evaporation on tropical cyclone boundary layer structure and intensity. *Mon. Wea. Rev*., **129**, 2481-2500.

Wright, C. W., E. J. Walsh, D. Vandemark, W. B. Krabill, A. W. Garcia, S. Houston, M. Powell, P. Black, and F. D. Marks, 2001: Hurricane directional wave spectrum spatial variations in the open ocean. *J. Phys. Oceanogr.*, **31**, 2472-2488.

Wu, C.-C., C.-Y. Lee, and I-I Lin, 2007: The effect of the ocean eddy on tropical cyclone intensity. *J. Atmos. Sci.*, **64(10)**, 3562-3578.

Yablonsky, R. M., and I. Ginis, 2008: Improving the ocean initialization of coupled hurricane-ocean models using feature-based data assimilation. *Mon. Wea. Rev*., **136,** 2592-2607.

Yablonsky, R. M, and I. Ginis, 2009: Limitation of one-dimensional ocean models for coupled hurricane-ocean forecasts. *Mon. Wea. Rev*., DOI 10.1175/2009MWR2863

Yablonsky, R. M., and I. Ginis, 2013: Impact of a warm ocean eddy's circulation on hurricane-induced sea surface cooling with implications for hurricane intensity. *Mon. Wea. Rev.*, **141**, 997-1021.

Yablonsky, R. M., I. Ginis, B. Thomas, V. Tallapragada, D. Sheinin, and L. Bernardet, 2014: Description and analysis of the ocean component of NOAA's operational Hurricane Weather Research and Forecasting (HWRF) Model. *J. Atmos. Oceanic Technol.*, (In Press).

Yin, X., Z. Wang, Y. Liu, and Y. Xu., 2007: Ocean response to typhoon Ketsana traveling over the northwest Pacific and a numerical model approach. *Geophys. Res. Lett.*, **34**, doi:10.1029/3007GL031477.

Yoshikawa, Y., A. Masuda, K. Marbayashi, M. Ishibashi, and A. Okuno, 2006: On the accuracy of HF radar measurement in the Tsushima Strait, *J. Geophys. Res.*, **111**, C04009, doi:10.1029/2005JC003232.

Zedler, S., T. Dickey, S. Doney, J. Price, X. Yu, and G. Mellor, 2001: Analyses and simulations of the upper ocean's response to hurricane Felix at the Bermuda Testbed Mooring site: 13-23 August 1995. *J. Geophys. Res*, **107**, 3232.

Zhang, J. A., 2007: An airborne investigation of the atmospheric boundary layer structure in the hurricane force wind regime. *Ph.D.Dissertation*, RSMAS, University of Miami, Miami, FL 33149, 60pp.

Zhang, D.-L., and E. Altshuler, 1999: The effects of dissipative heating on hurricane intensity. *Mon. Wea. Rev.*, **127**, 3032–3038.

Zeng, Z. , Y. Wang , D. Yihong, L. Chen and G. Zhiqiu, 2010: On Sea Surface Roughness Parameterization and Its Effect on Tropical Cyclone Structure and Intensity, *Adv. in Atmos. Sci*., **27(02),** 337-355.

Zeng, Z., Y. Wang , D. Yihong, L. Chen and G. Zhiqiu,2012：Numerical simulation on re-intensification of tropical remnant re-entering the sea: A case study. *J. Trop. Meteor*., **18(2)**, 146-161.

Zheng, Z.-W., C.-R. Ho, and N.-J. Kuo , 2008: Importance of pre-existing oceanic conditions to upper ocean response induced by super typhoon Hai-Tang. *Geophys. Res. Lett.*, **35**, L20603.